Mechanisms and Implementation of Thermo-Optical Annealing in Silica Fiber Sensors for Radiation-Induced Attenuation Mitigation

by

Aurelien Y. M. Legoupil

Diplôme d'Ingénieur (MSc), Engineering, Ecole Polytechnique, 2022

Submitted to the Department of Nuclear Science and Engineering
in partial fulfillment of the requirements for the degree of

MASTER OF SCIENCE IN
NUCLEAR SCIENCE AND ENGINEERING

at the

MASSACHUSETTS INSTITUTE OF TECHNOLOGY

September 2024

Authored by: Aurelien Y. M. Legoupil
Department of Nuclear Science and Engineering
August 16, 2024

Certified by: Michael P. Short
Department of Nuclear Science and Engineering
Associate Professor of Nuclear Science and Engineering
Thesis Supervisor

Accepted by: Ju Li
Department of Nuclear Science and Engineering
Chair, Department Committee on Graduate Students

Mechanisms and Implementation of Thermo-Optical Annealing in Silica Fiber Sensors for Radiation-Induced Attenuation Mitigation

by

Aurelien Y. M. Legoupil

Submitted to the Department of Nuclear Science and Engineering
on August 16, 2024 in partial fulfillment of the requirements for the degree of

MASTER OF SCIENCE IN
NUCLEAR SCIENCE AND ENGINEERING

ABSTRACT

In the context of quench detection systems for fusion superconducting magnets, temperature sensors based on optical fibers provide an effective solution for rapid, distributed measurement, with low sensitivity to electromagnetic interference. At the cryogenic temperatures and high radiation doses associated with this application, however, optical fibers undergo radiation-induced attenuation (RIA): light-absorbing point defects form within the silica glass structure, reducing the longevity and effectiveness of these sensors. In this work, we investigate the underlying microscopic defects and mechanisms of RIA and assess strategies for mitigation, namely, annealing via heat treatment (thermal annealing) and annealing via light propagation through the fiber (optical annealing, or "photobleaching"). We design a white light absorption spectroscopy setup with in-situ irradiation and optical annealing, working at liquid nitrogen temperature and different post-irradiation warm-up rates. For the pure silica core and F-doped cladding fibers studied, the RIA spectrum obtained is decomposed into known radiation-induced defect absorption bands, highlighting the key role of self-trapped holes in RIA at telecommunication wavelengths. Furthermore, absorption spectroscopy experiments are performed to show that thermal annealing at liquid nitrogen temperature is negligible, validating the transferability of the experimental results obtained at 77 K to 20 K applications. The decomposition of RIA into different defect contributions is supported by cold post-irradiation electron paramagnetic resonance (EPR) spectroscopy of fiber preform fragments, which reveals the presence of two types of paramagnetic centers: self-trapped holes and E'_γ centers. The post-irradiation transient grating spectroscopy (TGS) technique is adapted to glass samples with continuous cooling at liquid nitrogen temperature and in-situ optical annealing. With this technique, we could observe the changes in thermal and acoustic properties resulting from the evolution of defect populations, with the potential to complement other experimental techniques to better understand RIA build-up and annealing kinetics. To improve the modeling of thermo-optical annealing, we propose future experiments including isothermal annealing tests and a larger exploration of optical annealing parameters. Our RIA build up and annealing tests can help companies aiming to operate optical fibers under irradiation at cryogenic temperatures optimize their heat treatments to restore fiber transmission and the prevention of RIA during operation.

Thesis supervisor: Michael P. Short
Title: Associate Professor of Nuclear Science and Engineering

Acknowledgments - Remerciements

English

I want to express my deepest gratitude to my advisor, Mike, for supporting me during these two years. Thank you for believing in me, sharing my enthusiasm over new results and ideas, and doing everything you can to help me grow into the person I want to be. You are a kind and passionate scientist, a great teacher, and I am glad to have worked with you. Ericmoore, I would also like to thank you for your continuous interest in my progress and in working with me, your availability, and your guidance.

I want to acknowledge all the persons that have helped me on this project: if I have been able to carry out all these experiments, it's also thanks to you. This includes my collaborators at CFS, especially Owen, Rebecca, Erica, but also my colleagues at MIT who have participated in my RIA journey: Alexis, Angus, Bob, Ed, Jose, Max, Rui, Weiyue, Yifan, and Yifu. I extend my gratitude to all my friends at the Short lab, who make it an exciting place to work at: working alone on glass didn't mean being alone.

Rachel, thanks for helping me navigate the administrative maze that MIT can sometimes be. I also want to thank all the NSE and PSFC administrative staff for their support.

Mike, thanks to you, I had the chance to join EDF for an exciting internship last summer, and I would like to take this opportunity to thank the amazing people I worked with and who guided me there. In particular, I want to thank Nicolas and Hugues for being great mentors and engineers, and for believing in me.

I also want to thank all the professors who made my academic journey so enriching and enthralling. More specifically, I would like to thank Professor François Willaime for helping me join the fascinating world of nuclear materials and arrive where I am now.

I am so extremely grateful to have been supported all these years by such an amazing family. To my parents, I would not be here without you. You put so much effort into raising me into a kind, passionate, and hard-working man. I always felt that you would be happy if I did something that fulfilled me, and you taught me how to put my energy into achieving these dreams. Alexandre, I am very proud of being your brother, even if you are annoying sometimes: you are talented, clever, relentless (most of the time!), but above all kind. Some of you may say that I speak like Mémé Coq, but I can let you laugh. I love you all, and I am proud of you.

I want to thank all my friends. For my friends here, thank you for making this a new home for me for the last two years. To my friends on the other side of the Atlantic, it has been tough to be away from you, but thank you for your patience and support (I will come back!), and know that I have cherished every message and call, and the moments we got to spend together in the rare weeks I spent in France. Alex, I hope you enjoy reading this

thesis, and know that I feel so lucky to have you as a friend.

Avery, you are the best (but not everything is a competition!). Thank you for choosing to be by my side every day, for giving me your love and support, and pushing me to be better.

Français

Je tiens à exprimer ma plus profonde gratitude à mon directeur de recherche, Mike, pour m'avoir soutenu pendant ces deux années. Merci de croire en moi, de partager mon enthousiasme pour de nouveaux résultats et idées, et de faire tout ce que tu peux pour m'aider à devenir la personne que je veux être. Tu es un scientifique gentil et passionné, un excellent professeur, et je suis heureux d'avoir travaillé avec toi. Ericmoore, je voudrais également vous remercier pour l'intérêt constant que vous portez à mes progrès et à travailler avec moi, et pour votre disponibilité et vos conseils.

Je tiens à remercier toutes les personnes qui m'ont aidé dans ce projet : si j'ai pu réaliser toutes ces expériences, c'est aussi grâce à vous. Cela inclut mes collaborateurs à CFS, en particulier Owen, Rebecca, Erica, mais aussi mes collègues du MIT qui ont participé à mon aventure sur l'atténuation induite par l'irradiation : Alexis, Angus, Bob, Ed, Jose, Max, Rui, Weiyue, Yifan et Yifu. J'exprime ma gratitude à tous mes amis du laboratoire Short, qui en font un lieu de travail passionnant : travailler seul sur du verre ne signifie pas être seul.

Rachel, merci de m'avoir aidé à naviguer dans le dédale administratif qu'est parfois le MIT. Je tiens également à remercier l'ensemble du personnel administratif du département NSE et du PSFC pour leur soutien.

Mike, grâce à toi, j'ai eu la chance de travailler chez EDF pour un stage passionnant l'été dernier, et je voudrais profiter de cette occasion pour remercier les personnes extraordinaires avec lesquelles j'ai travaillé et qui m'y ont guidé. En particulier, je tiens à remercier Nicolas et Hugues pour les mentors et ingénieurs formidables qu'ils sont et pour avoir cru en moi.

Je tiens aussi à remercier tous les professeurs qui ont rendu mon parcours académique si enrichissant et passionnant. Plus particulièrement, je voudrais remercier le Professeur François Willaime pour m'avoir aidé à rejoindre le monde fascinant des matériaux pour le nucléaire et à arriver là où je suis aujourd'hui.

Je suis si extrêmement reconnaissant d'avoir été soutenu pendant toutes ces années par une famille aussi extraordinaire. À mes parents, je ne serais pas là sans vous. Vous avez déployé tant d'efforts pour faire de moi un homme gentil, passionné et travailleur. J'ai toujours senti que vous seriez heureux si je faisais quelque chose dans lequel je m'épanouissais, et vous m'avez appris à consacrer mon énergie à accomplir ces rêves. Alexandre, je suis très fier d'être ton frère, même si tu es parfois agaçant : tu es talentueux, intelligent, infatigable (la plupart du temps !) mais surtout gentil. Certains d'entre vous diront que je parle comme Mémé Coq, mais je vous laisse rire. Je vous aime tous et je suis fier de vous.

Je tiens à remercier tous mes amis. À mes amis d'ici, merci d'avoir fait de ce lieu une nouvelle maison pour moi au cours des deux dernières années. À mes amis de l'autre côté de l'Atlantique, il a été difficile d'être loin de vous, mais je vous remercie pour votre patience et votre soutien (je vais rentrer !), et sachez que j'ai chéri chaque message et chaque appel, et les moments que nous avons pu passer ensemble pendant les rares semaines que j'ai passées en France. Alex, j'espère que tu apprécieras la lecture de cette thèse, et sache que j'ai beaucoup de chance de t'avoir comme ami.

Avery, tu es le·a meilleur·e (mais tout n'est pas compétition !). Merci de choisir d'être

à mes côtés chaque jour, de me donner ton amour et ton soutien, et de me pousser à m'améliorer.

Contents

List of Figures

15

List of Tables

Nomenclature

Roman letters

a_{uv}, a_{ir}	Fitted coefficients for the "Urbach edge" and the "multiphonon edge" (exponential model)
BNC	Bayonet Neill–Concelman (coaxial cable connector)
C_{uv}, C_{ir}	Fitted proportionality coefficients for the "Urbach edge" and the "multiphonon edge" (exponential model)
CAD	Computer-Aided Design
CFS	Commonwealth Fusion Systems
DFT	Density Functional Theory
EHS	MIT Environment, Health and Safety Office
EPR	Electron Paramagnetic Resonance
FBG	Fiber Bragg Gratings
FC/APC	Ferrule connector/Angled Physical Contact (type of optical fiber connector)
FC/PC	Ferrule connector/Physical Contact (type of optical fiber connector)
FWHM	Full-Width at Half Maximum
g	Lande factor
Gy_{act}	Unit for the actual dose received by the fiber samples in the absorption spectroscopy setup, as defined in 2.5.5
H	EPR external magnetic field
h	Planck's constant
HTS	High-Temperature Superconducting (magnets)
IPA	Isopropyl alcohol
IR	Infrared
K-G	Kubo-Greenwood (LTIRA model)
LTIRA	Low-Temperature Infrared Absorption
m_s	Spin quantum number
MD	Molecular Dynamics
MEMS	Micro-ElectroMechanical Systems
MIT	Massachusetts Institute of Technology
NBOHC	Non-Bridging Oxygen Hole Center
n	Refractive index of the fiber core
n_e	Modal effective refractive index of the fiber core
ODC	Oxygen-Deficient Center
OSA	Optical Spectrum Analyzer
p_{11}, p_{12}	Components of the strain optic tensor

POL	Peroxy linkages
POR	Peroxy radical
RIA	Radiation-Induced Attenuation
RIE	Radiation-Induced Emission
RIRIC	Radiation-Induced Refractive Index Change (RIRIC)
S	Spin
SEM	Scanning Electron Microscope
SPARC	Soonest/Smallest Private-Funded Affordable Robust Compact, Commonwealth Fusion Systems fusion reactor
SAW	Surface Acoustic Wave
STE	Self-Trapped Electrons
STEX	Self-Trapped EXcitons
STH	Self-Trapped Hole
SuperK	NKT Photonics SuperK Compact light source
TGS	Transient Grating Spectroscopy
TTL	Transistor-Transistor Logic
UV	Ultraviolet

Greek letters

α_Λ	Thermal expansion coefficient of the optical fiber
α_n	Thermo-optic coefficient
Λ	FBG period
λ	Wavelength variable
λ_B	Wavelength reflected by the FBG
$\delta\lambda_{B,\epsilon}$	Strain-induced variation in FBG reflected wavelength
$\delta\lambda_{B,T}$	Temperature-induced variation in FBG reflected wavelength
μ_B	Bohr's magneton
ν	Frequency
ν_P	Poisson's ratio

Chapter 1

Background and motivation

1.1 Quench detection and the radiation-induced attenuation problem

Magnet superconductivity is achieved at very low temperatures. For high-temperature superconducting (HTS) magnets, such as those used for the Commonwealth Fusion Systems (CFS) SPARC project, the temperature is that of liquid helium, 20 K [1], [2]. However, there may be a sudden rise in temperature in the magnet, leading to a loss of the superconducting character in a process termed quenching [3]. As the HTS material becomes resistive, the current flowing through it causes considerable Joule heating. Moreover, as temperature increases, the liquid helium coolant may evaporate, thus accelerating the material temperature rise. In addition, the local temperature peak will lead to a warm-up of the surrounding areas of the magnet, propagating the loss of superconductivity. This leads to the loss of magnetic confinement and may result in severe and permanent damage to the magnet material.

Quench can happen accidentally in the SPARC magnets when the critical current or the critical temperature is exceeded due to loss of cooling, the degradation of the superconducting material, or excessive Joule heating. Thus, monitoring the magnet temperature is necessary to detect a quench event as quickly as possible and trigger a fast discharge to avoid excessive damage to reactor components. To detect the temperature increase associated with a quench, using electronic thermometers would require a very high number of devices to cover all of the magnets and their conductive wires would have to be isolated. Another way to detect quench is to monitor the magnet voltage level, but this would require measuring a very small voltage peak (≈ 1 mV to 1 V) in a very high background (≈ 10 kV) [3]. In this context, CFS has adopted optical fiber sensors to measure temperature peaking in the SPARC magnets. Fiber Bragg grating (FBG) technology enables the use of optical fibers as strain or temperature sensors [4]–[7]. On a certain portion of the optical fiber, a grating — a regularly spaced collection of bands in the fiber core having a different refractive index — is inscribed to reflect a certain wavelength. As the maximally reflected wavelength λ_B depends on the periodicity of the grating and on the effective index of refraction, it is sensitive to strain and temperature (see 1.2.2).

Optical fibers, however, are subject to radiation-induced attenuation (RIA) due to the creation of light-absorbing point defects (or "color centers") in the glass structure. This

radiation-induced darkening threatens the lifetime of optical fibers chosen for the SPARC reactor as temperature sensors. To maintain the fiber transmission at acceptable levels for the integrity of the quench detection system, the operator may even need to plan reactor outages to reheat the fibers (see 1.4.1). By analogy with light-water nuclear reactors, these outages could cost on the order of $1 - 3M/(GWe \cdot day)$ [8][1]. Therefore, to ensure reliable quench detection and to optimize these potential outages, a better understanding of the underlying microscopic mechanisms and defects, and strategies to mitigate or anticipate RIA are needed. The work presented here aims at improving this understanding and supporting RIA mitigation strategies.

1.2 Silica optical fibers for quench detection

1.2.1 Optical fiber material and radiation-hardened fibers

Optical fibers are usually made of three cylindrical layers. The inner cylinder, with optical index n_2 in figure 1.1, is called the "core", while the second layer (n_1) is called the "cladding". The light is guided by total internal reflection in the core, enabled by $n_2 > n_1$[2]. When there is indeed a step transition between the core and the cladding, fibers are called "step index" fibers. When the fiber core is very small (smaller than 10 μm), only one mode is guided axially through the fiber: these are called "single mode" fibers. As the optical path can be significantly different between multiple modes in step-index multimode fibers, a third type of fiber uses cores whose optical index increases gradually towards the center of the fiber. In these "graded index" fibers, modal dispersion is minimized as the speed of light is higher on the external layers of the fiber core. Figure 1.1 below represents these different types of optical fibers.

Optical fibers are commonly made with silica glass. Silica glass is an amorphous phase of SiO_2, meaning that there is no long-range order in the arrangement of Si and O atoms. On the short-range order, silicon atoms are each bonded to 4 oxygen atoms for the most part, forming a tetrahedron, and oxygen atoms are each bonded to 2 silicon atoms (figure 1.2.2). The amorphous solid is formed by melting and quickly cooling down, also called "quenching"[3], silica. The sudden decrease in temperature does not enable crystallization, and the material stays in a metastable disorganized solid phase. The glass structure is usually described using continuous random network theory (CRN) [13], [14]: the tetrahedral unit is the short range, the medium range is the interaction with close neighboring units, and the long range is the

---

[1]We can also calculate an estimate based on the electricity rate. From publicly available electricity rates for Massachusetts in early August 2024[9], if we take an approximate rate of $0.13/kWh, the obtained price of electricity is $3.12M/(GWe \cdot day)$.

[2]This inequality indeed enables Snell-Descartes's law of refraction ($n_1 \sin \theta_1 = n_2 \sin \theta_2$, where θ_2 denotes the angle of incidence with respect to the normal in the core, and θ_1 denotes the angle of refraction in the cladding) to not have a solution in θ_1 when $\sin \theta_2 > \frac{n_1}{n_2}$. For these high incidence angles (beam close to the axis of the fiber), there is then no refraction and total internal reflection. The acceptance angle of the fiber is also commonly defined by the numerical aperture: $NA = \sqrt{n_2^2 - n_1^2}$. Furthermore, this explains why bending optical fibers may induce losses, as the incidence angle is locally increased.

[3]It is important to emphasize that this "quench" phenomenon is different from the superconductivity quench phenomenon previously discussed. These two phenomena share a notion of immediacy, of the loss of superconductivity in one case and of the cooling in the other.
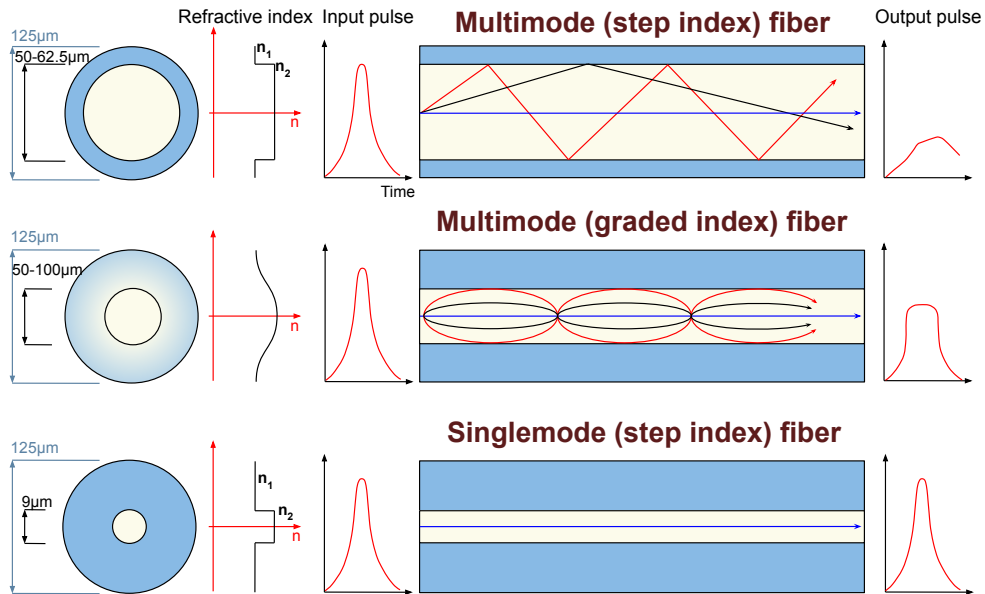
Figure 1.1: Three types of optical fibers: step-index multimode fiber, graded index multimode fiber, and single mode fiber (based on the information given in [10])
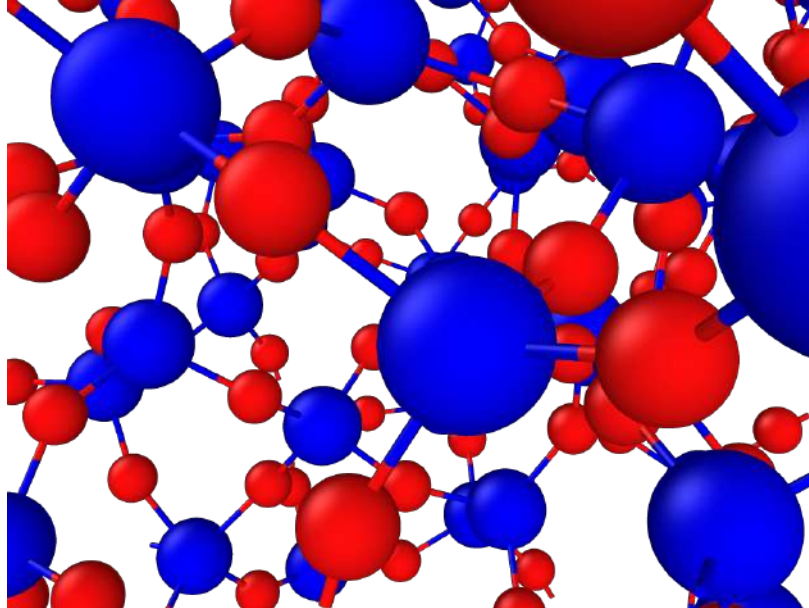
Figure 1.2: Pure silica glass network representation: silicon atoms (in blue) are each bonded to 4 oxygen atoms (in red) for the most part, forming a tetrahedron, in a metastable disorganized solid phase. This glass structure was obtained with a molecular dynamics quench simulation using the LAMMPS simulation tool [11]. The results are visualized with the OVITO software [12].

topology of the tetrahedron network and ring statistics. The network geometry of the glass itself, along with the elements involved, determines the types of defects possible to create in its structure and therefore determines how RIA will proceed in each fiber chemistry.

To tune the properties of the glass, and very commonly to change its optical index in optical fibers, doping elements are added to the glass matrix. There is a limited number of commonly used doping elements in passive optical fibers: germanium (Ge), fluorine (F), boron (B), phosphorus (P), aluminum (Al), and nitrogen (N) [15]. Girard et al. performed an extensive review of the performances of the different kinds of fiber technologies under irradiation and showed that doping had a significant effect on radiation-induced attenuation, which will be discussed in section 1.3.1. For example, they showed that phosphorus and aluminum, commonly used to limit rare-earth ion clustering (Er^{3+}, Yb^{3+}...), can lead to an increase in RIA of up to 10^4 dB/km, compared to attenuation levels generally lower than 1 dB/km for pristine fibers [15]. In particular, F-doped cladding and pure silica core fibers demonstrate the lowest levels of RIA. These fibers are often described as "radiation-hardened fibers" and are the ones chosen by Commonwealth Fusion Systems for the SPARC project and this study. According to Girard et al., photonic band gap fibers built with an air core and pure silica cladding are also very promising because of their very low RIA under gamma irradiation and their low residual RIA level after irradiation, but they emphasize the need for more investigations, as the literature on these fibers is very limited and they seem to show an unusual dose dependence, with a saturation of RIA at high doses [16].

1.2.2   Fiber Bragg grating (FBG) sensors

Using fiber Bragg gratings enables the use of optical fibers as strain or temperature sensors. On a certain portion of the optical fiber, a grating reflects a certain wavelength calculated as :

$$\lambda_B = 2n_e\Lambda$$

where n_e is the modal effective refractive index of the fiber core and Λ is the grating period. The sensitivity of this wavelength to axial strain change and temperature changes can be expressed by differentiating the previous equation with respect to strain and temperature. Othonos et al. [4] express it as :

$$\delta\lambda_{B,\epsilon} = \lambda_B \left[1 - \frac{n^2}{2}[p_{12} - \nu_P(p_{11} + p_{12})]\right]\epsilon_z$$

$$\delta\lambda_{B,T} = \lambda_B(\alpha_\Lambda + \alpha_n)\Delta T$$

where p_{11} and p_{12} are components of the strain optic tensor, ν_P is the Poisson's ratio and $\epsilon_z = \frac{\delta l}{l}$, and where α_Λ is the thermal expansion coefficient of the fiber ($0.55 \cdot 10^{-6}$ K^{-1} for silica [4]), the sensitivity of the grating period to a change in temperature, and $\alpha_n = (1/n)(\partial n/\partial T)$ is the thermo-optic coefficient ($8.6 \cdot 10^{-6}$ K^{-1} for silica [4]). At 1550 nm, the expected sensitivity is approximately 14 pm/K. Hence, if the two effects are correctly controlled and deconvolved, the fiber Bragg grating can be used as a strain or temperature sensor. In SPARC, FBG are the system chosen to measure temperature spikes in the magnets and detect quench events.

The grating inscription in the glass matrix can be performed in a variety of ways [17]. The photosensitivity of germanosilicate fibers enables them to change their refractive index under UV irradiation. The grating pattern is realized with UV light interference, sequential writing, photomasks, or point-by-point writing. For other types of fibers, high energy and intensity laser sources are required for the inscription, but it has been demonstrated to be possible with UV femtosecond laser sources [18], [19]. The technique used for the SPARC fiber is point-by-point inscription using an 800 nm femtosecond laser, using multi-photon absorption.

Figure 1.3 below represents a fiber Bragg grating, and the typical transmitted and reflected signals, with the peak wavelength λ_B used for sensing applications.
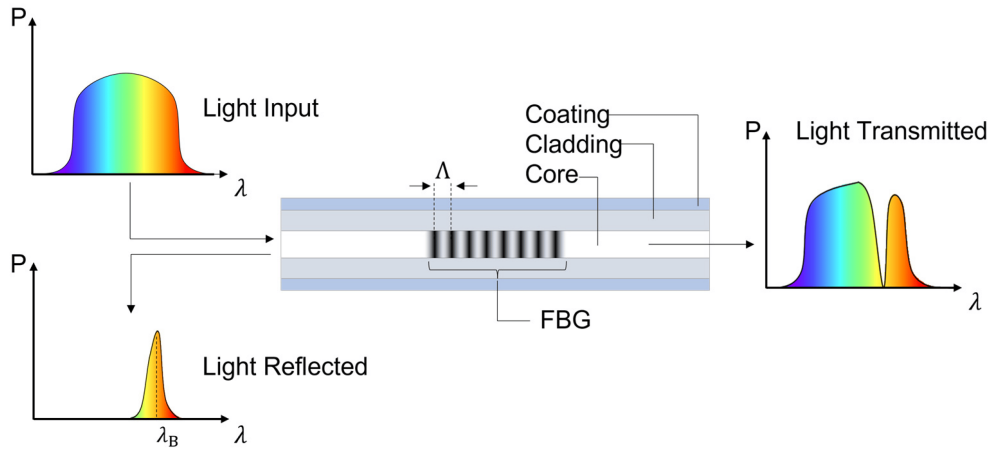
Figure 1.3: Typical structure of a positive-only index change fiber Bragg grating [20]

1.2.3 Attenuation in optical fibers

Optical fibers are often used to transmit signals over great distances due to their low attenuation levels, generally lower than 1 dB/km [15]. However, multiple factors can hinder light propagation through the fiber. Losses can occur due to intrinsic or extrinsic causes [21].

Intrinsic losses are commonly due to ultraviolet resonant absorption (electronic origin), mid-infrared absorption (glass network vibrational mode resonances) and Rayleigh scattering. Ultraviolet (UV) absorption is centered around $\lambda = 100$ nm and is sufficiently important for the "tail" of its curve, the "Urbach edge," to extend up to the visible, and tends to shift towards the infrared when dopants are added [21]. This tail can be described as proportional to $C_{uv}e^{-\frac{a_{uv}}{\lambda}}$, where a_{uv} is a fitted coefficient and λ is the wavelength. For infrared absorption (IR), the absorptive resonances are centered between 7 and 9 μm and are broadened by anharmonic coupling, leading to an absorption tail of the form $C_{ir}e^{\frac{a_{ir}}{\lambda}}$ ("Multiphonon edge") extending into the communication wavelengths and down to the near infrared. Finally, Rayleigh scattering corresponds to the elastic scattering of photons by dipoles present in the structure and with dimensions much smaller than the photon wavelengths. As some photons are reflected towards the source, this elastic scattering leads to an attenuation proportional to λ^{-4}.

Extrinsic loss sources are not related to the fundamental properties of the fiber material, but to additional species present in the glass or to the fiber structure. They can usually be diminished by a better control of the fiber fabrication process. These include metallic and rare earth impurities, hydroxyl impurities entered through water vapor, and imperfect fiber connections. Furthermore, fiber bending can also lead to radiative losses.

Moreover, defects can be created in the silica structure and lead to additional absorption bands, which happens during irradiation. This aspect will be further discussed in section 1.3.2. These additional defects can be both intrinsic when they are related to the intrinsic structure of silica glass, and extrinsic when related to impurities or fabrication defects.

Figure 1.4, from [22], summarizes these loss sources on the absorption spectrum of pure fused silica optical fibers.
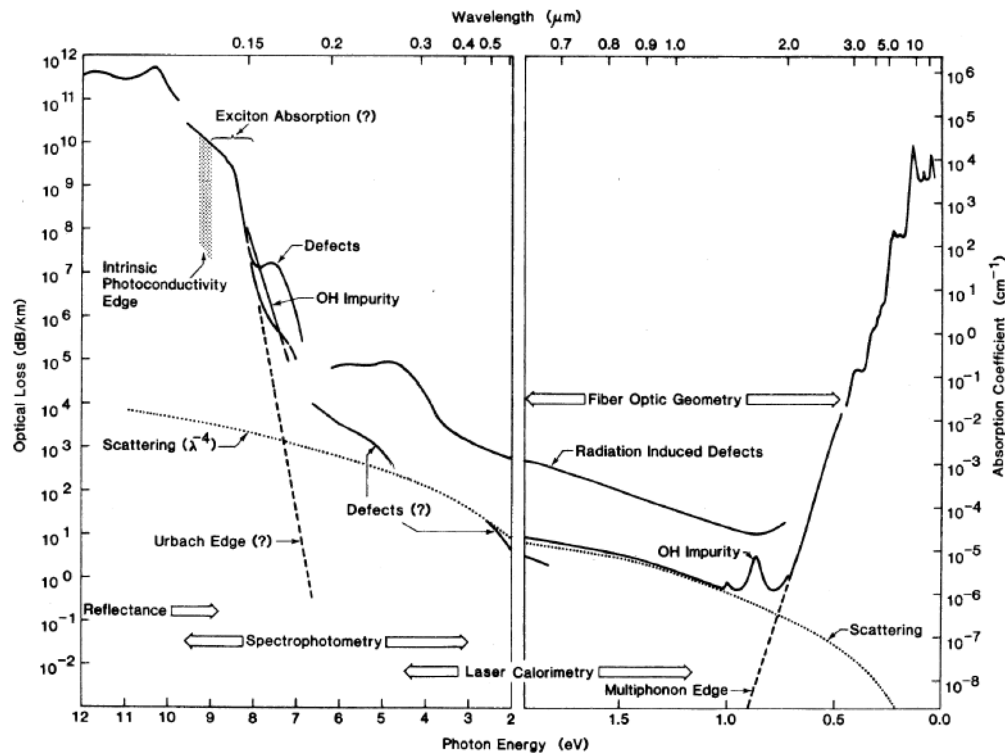
Figure 1.4: Optical attenuation spectra of pure fused silica. Radiation-induced spectrum given for Suprasil W1 fibers. [22]

1.3 Radiation damage and effects in optical fibers

1.3.1 Macroscopic phenomenology

Under irradiation, the silica glass structure is altered and point defects are created. Thus, three main radiation-induced effects can affect fiber transmission [13], [15]:

- Radiation-induced attenuation (RIA) is the result of radiation-induced point defects that can trap free electrons or holes. Each defect is associated with a certain number of

absorption bands, as discussed in section 1.3.2, and is thus very wavelength-dependent.

- Radiation-induced emission (RIE) corresponds to the emission of light by the fiber material under irradiation. This emission can be the result of pre-existing or radiation-induced defects luminescing when excited by incoming particles, or Cherenkov emission. According to Girard et al., RIE can be mitigated in most applications and environments. Furthermore, this phenomenon has a very low impact at infrared and telecommunication wavelengths (including 1550 nm, the wavelength chosen by CFS for FBG sensing) and matters mostly in the UV/visible range, as past experiments seem to indicate [23], [24].

- Radiation-induced refractive index change (RIRIC) is the result of both radiation-induced attenuation (via the Kramers-Krönig relations) and density change (Lorentz-Lorenz relation). For amorphous silica, Primak et al. observed a density and refractive index increase of 3% when irradiating at fluences larger than 10^{19} n/cm^2 with fast neutrons. At high doses, both amorphous silica and quartz transition to a new common phase called "metamict phase". Other works demonstrated that RIRIC also affects silica optical fibers under gamma irradiation [25], [26]. RIRIC may also affect the quality of FBG sensors by changing or blurring the refractive index Bragg gratings, but this effect on FBG sensors is not within the scope of this work, and a study on the radiation sensitivity of FBG has been performed in [27].

These different effects present both challenges and opportunities: they make telecommunication more difficult through irradiated optical fibers and their interconnection makes them harder to study independently, but they also present an interesting opportunity for potential new radiation sensors [28].

1.3.2 Radiation-induced defects in silica glass

In this section, we review the common defects that can be found in a pure silica core (PSC) optical fiber and their associated absorption bands, based on the existing literature. [15], [22], [29]–[31]

- The E' center is the best-known defect in crystalline SiO$_2$ and corresponds to an unpaired electron in a Si dangling bond ($\equiv$Si$^\bullet$). A study by Lo Piccolo et al. highlighted the different formation pathways for the formation of this defect, labeled E'_α, E'_β, E'_γ and E'_s [29]. These different pathways have a negligible influence on the resulting defect absorption bands.

- The non-bridging oxygen hole center (NBOHC) is the simplest oxygen-related defect in pure silica: it corresponds to an unpaired electron on an oxygen atom linked to one Si atom ($\equiv$Si$-$O$^\bullet$). This defect is also photoluminescent at 1.91 eV due to the decay of the excited state $n_{p_y}(O_{NB})$ (highest occupied molecular orbital) [29].

- Oxygen-deficient centers (ODC) are oxygen monovacancies and exist naturally in unirradiated silica, but their concentration is highly increased by irradiation. Two types of ODCs have been identified and associated with different absorption bands. ODC(I)

is a relaxed oxygen monovacancy ($\equiv$Si$-$Si$\equiv$). ODC(II) was first identified as an un-relaxed $\equiv$Si$-$Si$\equiv$, but some electron paramagnetic resonance (EPR) features led Tsai and Griscom to confirm a twofold-coordinated silicon model proposed by Skuja et al. in 1984 (>Si:) [32], [33]. These oxygen-deficient centers are also photoluminescent, at $4.3 - 4.4$ eV and $2.7 - 2.75$ eV, and might also be photoluminescent at 3.1 eV according to Lo Piccolo et al.

- Self-trapped holes (STH) are purely electronic defects, as they correspond to a hole trapped on a single bridging oxygen (STH$_1$) or delocalized over two equivalent bridging oxygen atoms (STH$_2$). Their discovery heavily relied on EPR [22], as explained in a paper written by Griscom in 2006 on the "history of their discovery and characterization" [34], and they are of great importance for telecommunication as their absorption bands belong to the highest wavelengths among silica defect absorption bands.

- Furthermore, at low temperatures, in the stability domain of STH, a non-Gaussian band attributed to these defects has been identified in the infrared. This low-temperature infra-red absorption band (LTIRA) can be well-fitted by a Kubo-Greenwood (K-G) expression ($RIA(E) = B_0 \cdot E \cdot \exp\left(-\frac{E}{S}\right) \cdot \left[\exp\left(\frac{E}{Q}\right) - \exp\left(-\frac{E_p}{Q}\right)\right]$, where B_0, S and Q are fitted and $E_p = 0.65$ eV is the self-trapping energy) or by a simpler exponential expression when only modeling the high-energy front ($RIA(E) = C \cdot \exp(-E/R)$, where C and R are fitted), as described by Dianov et al. in 1989 [35].

- Peroxy radicals (POR, Si$-$O$-$O$^\bullet$) have also been identified by EPR. However, though computations have predicted their absorption band centers (see for example [36]), no data was found for the full width at half maximum (FWHM), representing a potential difficulty for absorption spectrum deconvolution, given their absorption band centered around 2 eV.

- Peroxy linkages (POL, Si$-$O$-$O$-$Si) absorption bands are also the results of first principle calculations. [37] By deduction from the formation pathway of POR from POL, Nishikawa et al. [38] also associated the experimental 3.8 eV absorption band with POL.

- Self-trapped excitons (STEX) are created when an excited electron and hole create a localized distortion in the lattice which lowers their total energy and thus traps them. These defects are also photoluminescent.

- The existence of self-trapped electrons (STE) and their absorption bands have also been derived from numerical simulations. DFT calculations performed by El-Sayed et al. show that these electrons tend to be trapped at wide O$-$Si$-$O angle sites (angles exceeding 132°) [39].

No extensive literature presenting natural concentrations of these defects in optical fibers and the evolution of these populations was found, as the majority of the studies only calculate the absorption spectrum by subtracting the current irradiated transmission spectrum from the initial pristine fiber spectrum. We can however mention the EPR study by Girard et al.

in 2008 [40] which found no paramagnetic centers in F-doped fibers above the detection limit and does not state the concentration of the Ge-related paramagnetic centers in the Ge-doped fiber material probed. Their computational study presents some formation energy data for ODCs in pure and Ge-doped silica [41]. Work performed by Nishikawa et al. gives some concentration data as a function of dose (photons at 6.4eV, 7.9eV and Co-60 γ rays) for E' centers, NBOHC and POR for samples with different oxygen contents, and contributes to the understanding of point defect formation pathways [42].

Outside of defects directly related to the glass network, O_3, O_2 and chloride impurities resulting from the manufacturing process contribute to optical absorption and photolumi- nescence. Hydrogen centers H(I) ($>Si^\bullet\!-H$) do not seem to contribute to optical absorption or luminescence. In addition, it has been shown that hydrogen loading of pure silica core fibers can play an important role in increasing the fiber resistance to irradiation by enabling reactions that neutralize ODCs, E' centers and NBOHCs [29] :

$$\equiv\!Si\!-\!Si\!\equiv\, +\, H_2 \longrightarrow\, \equiv\!Si\!-\!H + H\!-\!Si\!\equiv$$

$$\equiv\!Si^\bullet + H_2 \longrightarrow\, \equiv\!Si\!-\!H + H^0$$

$$\equiv\!Si\!-\!O^\bullet + H_2 \longrightarrow\, \equiv\!Si\!-\!OH + H^0$$
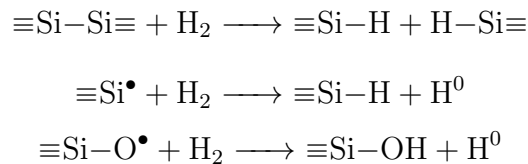
Heating unirradiated SiO_2 glasses in oxygen gas flow can also help neutralize pre-existing ODCs:

$$\equiv\!Si\!-\!Si\!\equiv\, +\, \frac{1}{2}\,O_2 \longrightarrow\, \equiv\!Si\!-\!O\!-\!Si\!\equiv$$
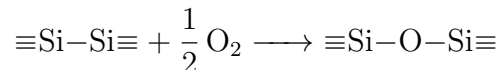
The table in figure 1.5 summarizes the properties of the different defects and figures 1.6 and 1.7 display their associated optical absorption bands. It is worth noting that the absorp- tion bands are broadened. This broadening is due to the coupling of electronic transitions with phonons ("homogeneous broadening") and to the different environments surrounding the defects because of the disorder of the amorphous material ("heterogeneous broadening") [43].

1.4 Damage annealing to mitigate radiation-induced attenuation

1.4.1 Thermal annealing

When defects in the silica glass structure are thermally excited, the energy imparted to them can enable them to leave their bound state: this is known as "thermal annealing". An electron hole in the valence band, for example, can recombine with an electron in the conduction band. The possibility of removing the defect from the glass structure may be enhanced by the presence of impurities with which the defect can react. For example, we can cite the annealing mechanisms of E' centers: at low-OH content, at temperatures higher than 150°C, they can react with a molecule of dioxygen to form a peroxy radical, while at high-OH content, at temperatures exceeding 300°C, they can react with water molecules according to the following reaction : $\equiv\!Si^\bullet + H_2O \longrightarrow\, \equiv\!Si\!-\!OH + H^0$ [44]. Thus, the thermal

Name	Structure	Param	OA peak eV (FWHM eV)	Oscillator strength	Note	PL peak eV (FWHM eV, lifetime RT)	Refs
Oxygen deficient center	> Si:	No	5.05 (0.32)	0.15	S_0-S_1 transition	4.4 (0.4 eV; 4.0 ns)	[16,29,156–159]
					ISC assisted (T_1-S_0 transition)	2.75 (0.34; 10 ms)	
			3.15 (0.30)[1]	$1.60 \ 10^{-7}$	S_0-T_1 transition	2.75(0.34; 10 ms)	
ODC(II)			6.9 (0.4)	0.1–0.2	PL features similar bands	4.4 and 2.7	
ODC(I)	≡Si-Si≡	No	7.6 (0.5–06)	0.1–0.2		4.4 (0.4 eV, 1.4 ns)	[16,139,157,159–162]
Non-Bridging Oxygen Hole Centers	≡Si-O•	Yes	1.97 (0.17)	$1.90 \ 10^{-4}$	Asymmetric Pekarian-shaped	1.91 (0.17, 10–20 µs)	[16,121,163–169]
			4,8 (1.0)	0.05	5 Gaussian are needed to describe		
			6.4 (1.7)[1]	0.05	the absorption in UV VUV		
NBOHC					see ref [167] for the relative intensity		
E'	≡Si•	Yes	5.8 (0.7)	0.1–0.2		Not observed	[16,156,170–172]
Self-trapped hole		Yes	2.61 (1.2)	0.283[2]	Inherent	None reported	[173–180]
STH$_1$			1,88 (0.2–0.5)		Strain-assisted (observed in OF)	None reported	[173,177,178]
STH$_2$		Yes	2.16 (0.3–0.6)	0.283[2]	Inherent	None reported	[173–180]
			1.63 (0.3–0.7)		Strain-assisted (observed in OF)	None reported	[173,177,178]
Peroxy Linkage **POL**	Si-O-O-Si	No	3.8(0.2), 4.2(0.6, 7.3(0.2), 7.5(0.1)	~0.0005–0.003	Computational	None reported	[30]
Peroxy Radical **POR**	Si-O-O•	Yes	2.02, 4.08, 5.02	0.00056, 0.052,0.035	Computational (one SiO$_4$ H-passivated tetrahedron cluster)	–	[126,132,181]
			2.0, 4.8	0.0004, 0.2	experiment		
Self-trapped Electron			3.7	–	Computational	–	[173,182]
STE			4.6	–	Computational	–	[173,182]
			6.4	–	Computational	–	[173,182]
Self-trapped Exciton **STEX**		No	4.2 (1.16)	–	Computational	2.85 eV (theory)	Theory [183]
			5.3 (0.78)		Experimental	2.6 −2.8 eV (exp)	Exp [184–189]
Ozone	O$_3$		4.8 (0.8–0.86)	Cross section $1.2 \ 10^{-17}$ cm^2	VUV UV bleaching can induce the O$_2$ emission [21]		[190,191]
O2	molecular oxygen	Yes	0.97 (0.013)	$1.1 \ 10{-8}$	T1-S0 transition	0.97 (0.01 eV, 0.4–0.8 s)[3]	[192–198]
			1.62 (0.013)	$4.2 \ 10{-9}$	T1-S1 transition		
Cl0	Cl0	Yes	3.26	–	–	–	
			3.65	–	–	–	[88,177,199,200]
Cl2	Cl2	No	3.78 (0.6)	3.8 cross section $2.58 \ 10^{-19}$ cm^2	Vibronic progression T<110 K	1.2 (0.42, 5 ms at 13 K)	[122]
			2.3				
H(I)	>Si•-H	Yes	Not observed	–	–	Not observed	[14,17,23]
LTRIA	STH	Yes	0.6 − 0.7 eV (non-Gaussian)	–	LTRIA is attributed to inherent STHs	Not observed	[153]

[1] Peak and FWHM derived from PLE spectra.
[2] Linear combination Gaussian bands peaking at 2.16 and 2.60 eV.
[3] Strong radioluminescence signal under X-rays [103].

Figure 1.5: Review of the main optical properties of pure-silica related point defects and those related to chlorine and hydrogen impurities. (From Girard et al. [15])
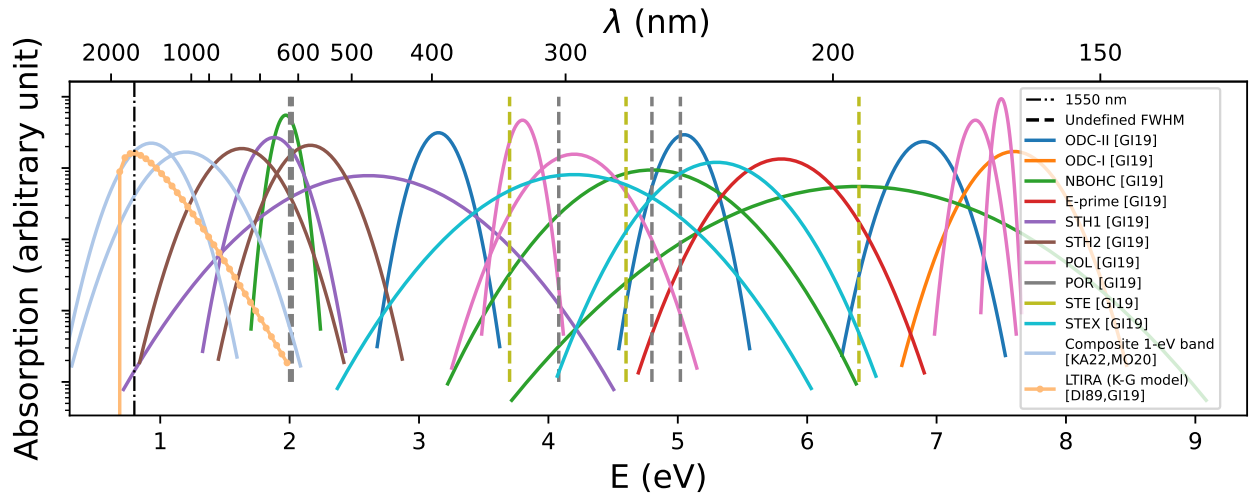
Figure 1.6: Optical absorption bands of defects in pure silica core optical fibers. The 1550 nm telecommunication wavelength is shown by a black vertical line. Peaks for which the full width at half maximum (FWHM) is unknown are represented by vertical colored dashed lines at the peak energy. The composite 1-eV band was tentatively associated with self-trapped holes [30]. From decompositions found in other studies [15], [30], [31] and the distribution of absorption bands shown here, we expect this composite 1-eV band, STH of type 1 and type 2, NBOHC and the LTIRA band to matter the most in the high visible and infrared spectrum. (References: GI19 [15], MO20 [30], KA22 [31], DI89 [35]. Complements: [22], [29].)
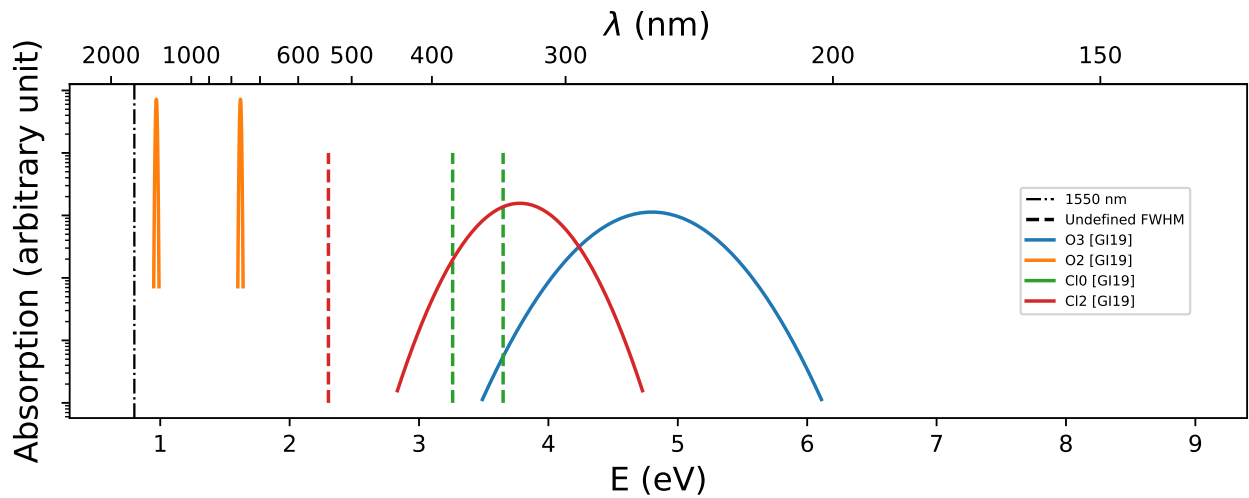
Figure 1.7: Optical absorption bands of the main impurities in pure silica core optical fibers. The 1550 nm telecommunication wavelength is shown by a black vertical line. Peaks for which the full width at half maximum (FWHM) is unknown are represented by vertical colored dashed lines at the peak energy. (Reference: GI19 [15].)

excitation of defects at the source of RIA may enable to anneal them and reduce the level of attenuation in optical fibers.

This possibility is widely presented in the literature, and numerous studies show that RIA levels decrease when optical fibers are heated (see for example [45]). In addition, for certain low-temperature stable defects such as STHs, a simple relaxation at room temperature is often sufficient to anneal them. This makes them more difficult to study experimentally, as the entire work must then be carried out at cryogenic temperatures, from irradiation to spectroscopic characterization [30].

The impact of thermal annealing on the RIA level has been confirmed by initial experiments under irradiation carried out by CFS [46].

However, it is worth noting that temperature increase does not always have a positive impact on RIA. Girard et al. carried out experiments in which UV-RIA first increases when the irradiation temperature is raised to 200°C, and then decreases, highlighting the complexity of combined radiation and temperature effects and the diversity of bleaching mechanisms. [47]

1.4.2 Optical annealing

When optical fibers need to be maintained at cryogenic temperatures, as is the case for the application to temperature measurement of superconducting magnets in the SPARC reactor (20 K), annealing defects at the source of RIA requires imparting energy to them by other means. It is possible to transmit energy to these defects by circulating a laser beam along the optical fiber, since the absorption of photons by the defects can enable them to make energy transitions (by $E = h\nu$) sufficient to anneal. This technique, known as optical annealing or more commonly "photobleaching", has also been used in several experimental tests aimed at reducing the level of RIA [48]–[51].

Optical annealing depends on three main parameters: the power of the laser injected into the optical fiber to perform the annealing (number of photons delivered per unit time to anneal defects), its wavelength (directly related to the energy difference of the allowed transitions, but also allowing the laser to be more or less absorbed by the medium in which it propagates) and the fiber length (as the laser is attenuated along its path in the optical fiber, fewer photons will be available to photobleach defects at the end of the fiber).

In this work, we focus on studying optical annealing at 785 nm, while other tests are carried out by CFS to determine the optimal annealing wavelength.

1.5 Survey of RIA study techniques

The main experimental techniques used to characterize the defects in the optical fiber glass structure in the literature are:

- Absorption spectroscopy, which is presented in chapters 2 and 4.

- Electron paramagnetic (or spin) resonance (EPR/ESR), which is presented in section 5.1

- Raman spectroscopy which can provide information on the chemical structure of a material [27], [52]–[54]. Preliminary work led on this project has shown no significant response of our fiber material to Raman spectroscopy, so this technique will not be further explored in this work.

- Radiation-induced photoluminescence spectroscopy [23], [27], [44], where the spectrum of the photons emitted by the silica luminescent centers is measured to probe the population of these centers.

The main computational techniques used to simulate RIA and the response of silica glass to the previously mentioned experimental techniques are:

- Density functional theory (DFT) for the calculation of the g-tensor for EPR [55], the understanding of the nature and structure of the different electronic defects [39] or the calculation of absorption bands [37].

- Molecular dynamics (MD) for the study of the dynamics of the silica atomic structure under irradiation and the evolution of the long-range order statistics, such as ring statistics evolution [14], [56]. As MD doesn't represent electronic densities, however, its application to the study of the point defects in amorphous silica remains limited.

1.6 Thesis's main methodology and contributions

This work meets two main objectives: characterizing the defects contributing to radiation-induced attenuation in pure silica core optical fibers[4] at cryogenic temperatures, and implementing, probing and modeling thermal and optical annealing. These new data are essential to the development of models predicting the evolution of RIA under these conditions, models which should be used to optimize the safe operation of systems such as SPARC's quench detection system, as well as the design of its outages.

In order to characterize the radiation-induced defects, three main experimental techniques have been explored. An *in-situ* white light absorption spectroscopy setup has been designed in order to probe and identify the different point defect contributions to the RIA spectrum. The design of this experimental setup is presented in chapter 2, and the results of RIA spectrum decomposition are presented in 4. Chapter 5 presents how electron paramagnetic resonance and transient grating spectroscopy can serve as complementary techniques to characterize the different defects contributing to RIA, with EPR confirming the results of absorption spectrum decomposition.

Experiments presented in this thesis are performed at liquid nitrogen temperature (77 K), while the quench detection system will operate at liquid helium temperature (20 K). Proving that the results we obtain apply to the latter temperature therefore necessitates a better understanding of thermal annealing processes at cryogenic temperatures. In chapter 3, we

---

[4]Exail IXF-RAD-SM-1550-014-PI: pure silica core and 0.5 w% F-doped silica cladding. The fluorine diffuses slightly to the core, giving rise to 0.1 w% concentration in the core. Fluorine is used to lower the refractive index of the core [57], has been shown to reduce transmission loss in optical fibers manufactured by vapor axial deposition [58], and is associated with low radiation-induced attenuation levels and no particular defect structure apart from Si-F linkage [15].

perform two experiments in order to prove that these processes are essentially frozen at liquid nitrogen temperatures, and thus at temperatures lower than 77 K. While the first experiment achieves this goal, the second is limited by the non-negligible impact of optical annealing by the probe light source. This second experiment enables us to record optical annealing kinetics, which impacts any of the optical absorption measurements we perform. In chapter 4, we further explore the mechanisms and kinetics of post-irradiation thermal annealing, with the intention of improving the modeling of these treatments. These improvements are necessary to optimize heat treatment downtimes which may be necessary for long term operation of the quench detection system. To perform these experiments, we use the *in-situ* absorption spectroscopy setup to record annealing kinetics.

Chapter 2

A white light absorption spectroscopy setup for RIA and annealing measurement at cryogenic temperature under irradiation

By passing a broadband light source through the fiber material as it undergoes changes (irradiation, temperature variations or optical annealing) and analyzing the transmitted spectrum with a spectrometer, we can obtain a continuous absorption spectrum characterizing the material. Indeed, as we will further see in chapter 4, this simple curve can be deconvolved into different contributions, each associated with a specific phenomenon or defect and often known from the literature (see figures 1.6 and 1.7). The deconvolved signal thus gives us an idea of the relative importance of the contribution of the different defects.

This section covers the design of an absorption spectroscopy setup to measure RIA in optical fibers at cryogenic temperatures during irradiation in the MIT Gammacell gamma irradiator with the possibility to probe the effects of optical annealing (see 1.4.2). First, section 2.1 presents an overview of the absorption spectroscopy setup built for this project and section 2.2 details the method for preparing optical fiber samples for these experiments. Then, section 2.3 focuses on the choices made for the temperature control of the fiber samples, which is necessary to understand the impacts of thermal annealing. Section 2.4 describes the Gammacell irradiator used for these experiments in more detail. Finally, section 2.5 builds upon this understanding of the gamma source to calculate the actual dose rate in optical fiber samples in the spectroscopy system.

2.1 System design overview
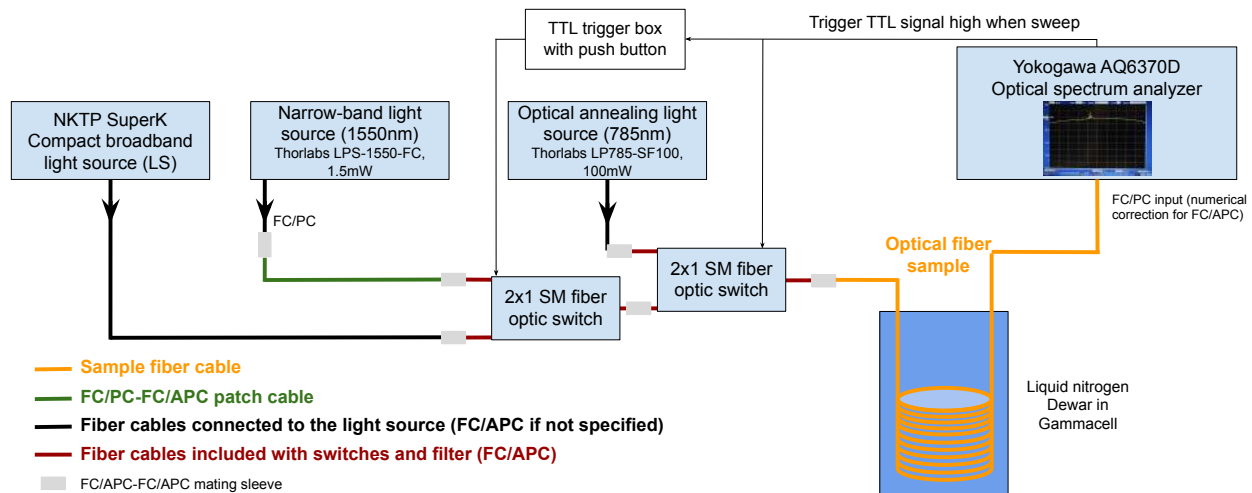
Figure 2.1: White light absorption spectroscopy experimental setup with optical annealing and a secondary narrowband 1550 nm light source.

Figure 2.1 shows a diagram of the broadband absorption spectroscopy setup. The spooled fiber sample is placed inside a dewar containing liquid nitrogen to maintain a temperature of 77 K. This fiber is prepared according to the method described in 2.2, and most of the length of the sample is contained in the immersed spool. The dewar is placed inside the Gammacell chamber during irradiation (see 2.4). The ends of the fiber coming out of the irradiator are connected to a light source on one end, and to an optical spectrum analyzer (OSA) on the other end.

The OSA used in the study to probe the absorption spectrum is the Yokogawa AQ6370D. This analyzer spanning the 600 nm -1700 nm range is chosen to cover the communication wavelength (1550 nm) which is the wavelength at which the temperature sensor works, making it the most important wavelength at which RIA must be known, and also a large-enough part of the spectrum at lower wavelengths to enable better decomposition of the spectrum, as we have seen that most defect absorption peaks were much lower than 1550 nm. Furthermore, this OSA presents good sensitivity and connectivity while still being widely used and thus available for rental, which is not the case of the more advanced models. It is connected to the fiber via an FC/PC connector (ferrule connector/physical contact), but has a built-in numerical correction for the FC/APC (ferrule connector/angled physical contact) cables used in this project. In addition, it is possible to program it for specific goals, and appendix A details the main settings used in these experiments and the program to enable periodic sweeping over the spectrum and saving. More information on how the OSA data is processed and used in the different experiments is given in the following chapters.

On the other end of the fiber, three light sources can be connected to the sample via 2×1 optical switches[1]. While the spectrum is being scanned, the OSA sends a TTL signal

---

[1] The switches used in this setup are Agiltron/Photonwares MEMS fiber to fiber 1x2 latching fast switch modules, made of SMF-28 fiber and including a BNC interface for TTL control

to select the probe light source: a broadband light source or a 1 mW 1550 nm fiber-pigtailed laser. The main probe light source is the broadband NKT Photonics SuperK Compact. This light source is chosen for its broad spectral range ($450 - 2400$ nm), high output power (> 100 mW) to get a high signal-to-noise ratio, and its single-mode FC/APC output termination. However, using a high-power broadband source runs the risk of optically annealing the fiber whose spectrum is being measured. This problem is discussed further in chapter 3. The 1550 nm laser is inserted to enable probing only the region of the spectrum close to the communication wavelength when necessary, to limit potential optical annealing from the broadband light source. When the spectrum is not being scanned, another light source (narrowband 100 mW single-mode fiber-pigtailed laser) is connected to the sample to be able to test optical annealing at 785 nm.

This setup tests RIA evolution while controlling irradiation, optical annealing power and, to a certain extent, temperature (see 2.3). The optical annealing light source can be changed if other wavelengths are tested, but this work focuses on the one selected by CFS. The amount of RIA that can be measured is limited by the noise level: figure 2.2 compares the typical noise floor and SuperK spectrum at full power measured with this setup. In addition, the light source switching architecture was chosen because coupling two different light sources into a single-mode fiber is challenging in terms of both power and spectrum width conservation. This also means that the fraction of time available for optical annealing at 785 nm decreases when sweep duration and frequency increase.

2.2   Sample preparation

To prepare a sample of the fiber of interest (Exail IXF-RAD-SM-1550-014-PI), we spool the desired length (certain number of windings) with a manual winding machine, secure the spool with adhesive tape on a plastic spool, and add protective jackets to the fiber ends. In order to connect the sample to extensions and FC/APC fiber pigtails on both ends, each fiber end is manually stripped of its jacket, and the sample fiber ends are uncoated by burning and wiping the ends with isopropyl alcohol (IPA). Both ends of each splice are cleaved with a Fujikura CT50 optical fiber cleaver and spliced using a Fujikura 90S+ fusion splicer. The total length of the final sample is measured with an optical reflectometer (Yokogawa AQ1000 OTDR) by connecting it to a reference 150 m long fiber. For the experiment, the fiber is placed in the metallic spool described in section 2.3, which is sealed with cryogenic tape, and the ends are measured using a tape measure to obtain the spooled length of fiber that is being irradiated.

2.3   Temperature control for slow thermal annealing testing

Initially, the experiments were performed by spooling the fiber around the type of plastic spool represented in figure 2.4 and immersing it into liquid nitrogen. However, this spool did not allow accurate measurement of the sample temperature nor did it enable slowing down the warm-up to observe with precision the different effects of thermal annealing as the sample

Resolution: 2 nm. Sensitivity: 'MID'. Sampling: 2751(MANU). 2x speed. Angled PC correction.
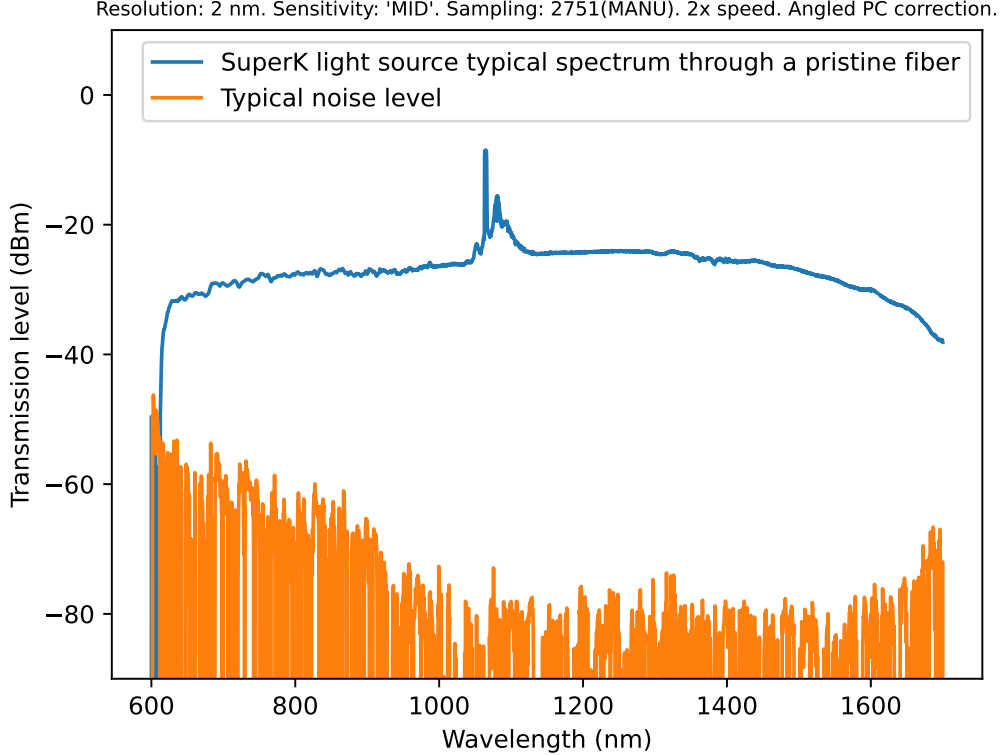
Figure 2.2: Typical noise level and broadband light source spectrum at full power measured with the Yokogawa AQ6370D (OSA settings detailed above the figure)

goes from 77 K to higher temperatures. To achieve this, a metallic spool enclosing the fiber with a significant thermal mass and with an embedded temperature sensor was designed. This new spool, conceived to fit in the initial experimental setup and made with stainless steel 316L, is represented in figure 2.5. A Lake Shore Cryotronics Cernox AA[2] temperature sensor is inserted next to the fiber in the hole shown in figure 2.6, with Apiezon N grease for thermal contact. This calibrated sensor combines a high sensitivity at low temperatures and a good sensitivity over a broad range. It also has good resistance to ionizing radiation (relative calibration offset $\frac{\Delta T}{T} < 0.5\%$ for temperatures higher than 77 K and doses under 1 MGy [59]). The sensor is connected to a Lake Shore 211S monitor interrogated via a program given in appendix B.

An initial cool-down and warm-up test was carried out to check the thermal response of the spool. The spool was plunged into liquid nitrogen until stabilization at 77 K and taken out to ambient air for warm-up. Figure 2.7 shows a picture from the warm-up part of this test, and figure 2.8 shows the evolution of the temperature measured by the sensor in the spool over time. As expected, boiling enables rapid cool-down (≈ 10 min) of the spool and the warm-up to room temperature is slow enough (3.5 h) to gradually observe the effects of thermal annealing as the spool warms up. It is important to note that the sensor, embedded inside the

---

[2]CX-1080-AA-20L-QT32-2

1) Winding the sample fiber
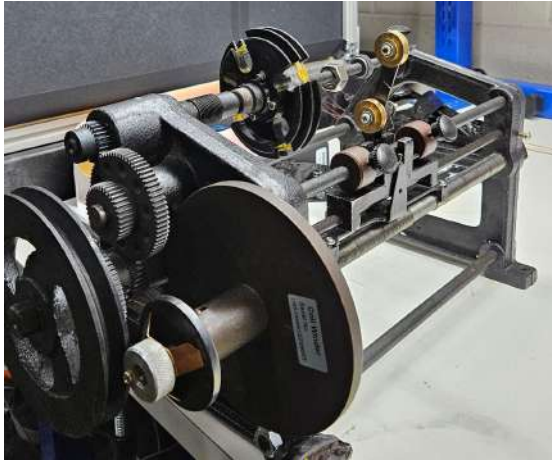
2) Cleaving and splicing the sample, extension, and pigtail fibers

3) Measuring the total length of the final sample with a reflectometer
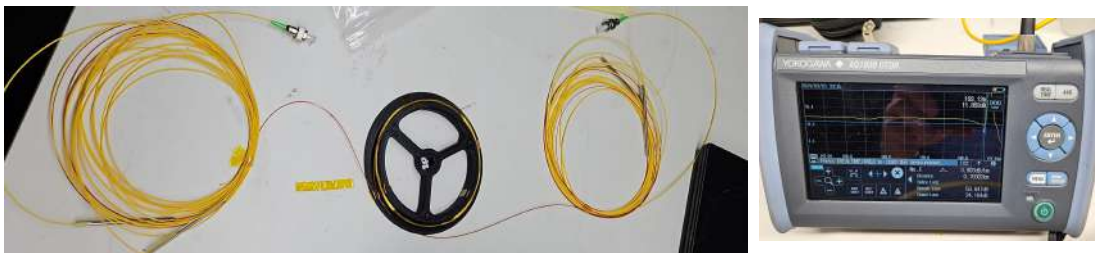
Figure 2.3: Optical fiber sample preparation steps for white light spectroscopy

Figure 2.4: Original optical fiber plastic spool (Spooling diameter: 9 cm)

spool, is placed near the inner side of the spooled fiber. The temperature measurement may therefore be slightly delayed compared to the sample temperature evolution. This possible discrepancy is studied in appendix C.

With this spool, the temperature changes are not completely controlled, even if it could have been achieved by adding resistive heaters and changing the cooling system, because it was not necessary to get a first understanding of thermal annealing processes. This is a possible improvement for future work.
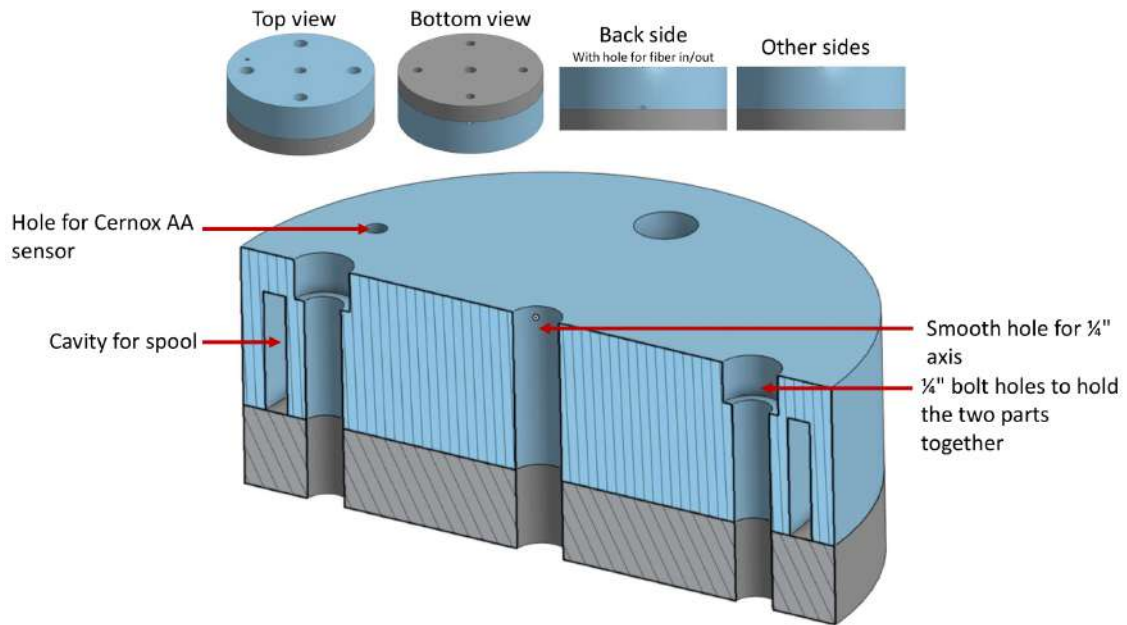
Figure 2.5:   CAD design of the new stainless steel spool
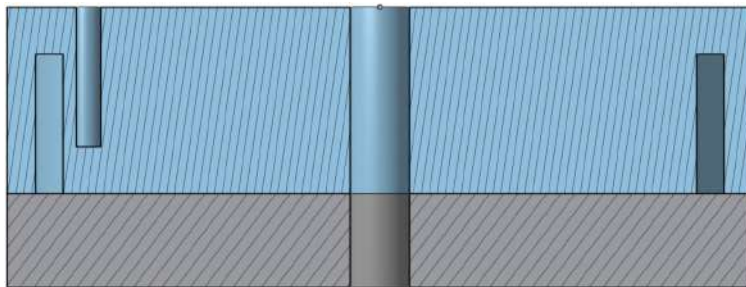
Figure 2.6:   CAD section view of the spool in the sensor plane

Figure 2.7:   Picture of the spool during ambient temperature warm-up test after liquid nitrogen cool-down
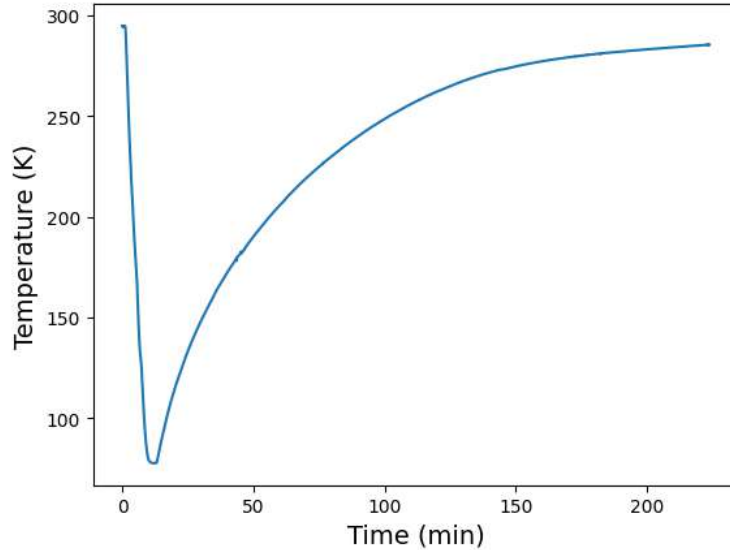
Figure 2.8: Evolution of the temperature measured by the sensor over time during cooldown in liquid nitrogen and warm-up in ambient air

2.4 The Gammacell 220F irradiator

The Gammacell 220F is a cobalt-60 γ-irradiation unit used at MIT to irradiate samples at about 15 kGy/h [3] [60]. Figure 2.9 shows the external aspect of this device. The samples are inserted in a chamber (6.10 inches diameter, 8.06 inches high) by opening the leaded collar. The chamber works as an elevator, taking the sample down to the middle of the source during irradiation. The source cage, represented in figure 2.10, contains 48 double-sealed source pencils, each 8.31 inches long, on an 8.23 inches pitch circle diameter. Each pencil is composed of 7 cobalt 60 slugs.

The typical dose distribution in air given by the manufacturer for a similar Gammacell model (220E) is shown in figure 2.11.

2.5 Actual sample dose rate calculation

2.5.1 Aim and motivation

In the Gammacell irradiator facility, the reference data given is the dose rate for air at the center of the chamber when it is empty. However, in our absorption spectroscopy setup, a liquid nitrogen dewar containing the metallic spool which holds the fiber is inserted in the dewar, and all of these different layers may absorb some gamma radiation and lower the dose rate at the center of the chamber. Furthermore, the sample is not placed at the center: the fiber is on a circle of approximately 9 cm in diameter (in the cavity of the metallic spool),

---

[3]The activity decaying over time, this dose rate is an order of magnitude at the time the experiments were conducted and, in the experimental data presented in the following chapters, the dose rate at the time of each experiment is the one recorded and used.
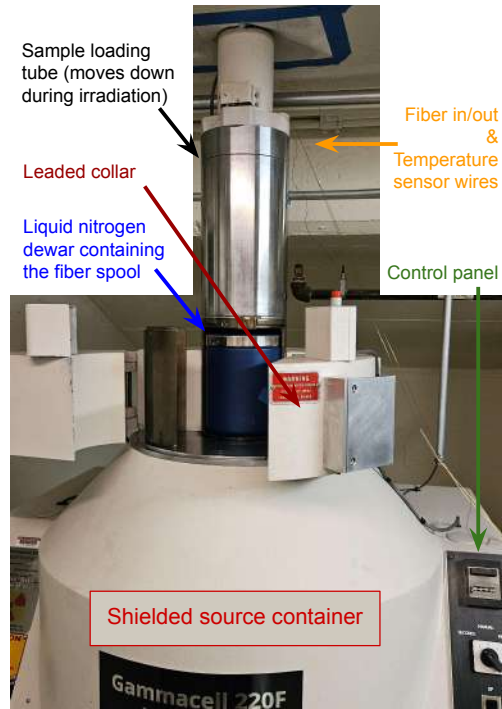
Figure 2.9: External elements of the Gammacell irradiator in the sample loading (upper) position with its drawer open, after setting up the liquid nitrogen dewar and feeding the fiber ends and the temperature sensor wires through the instrumentation hole.
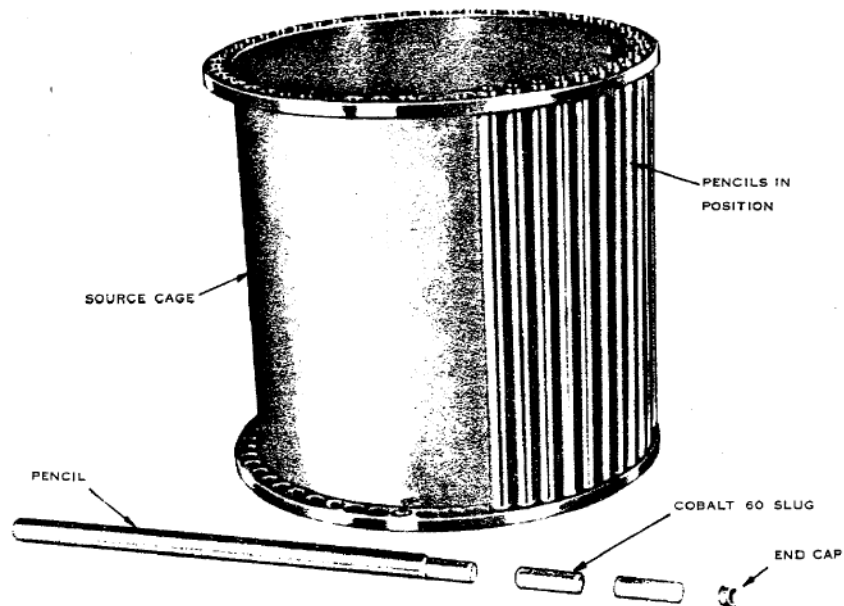
Figure 2.10: Gammacell source cage and pencils [60]
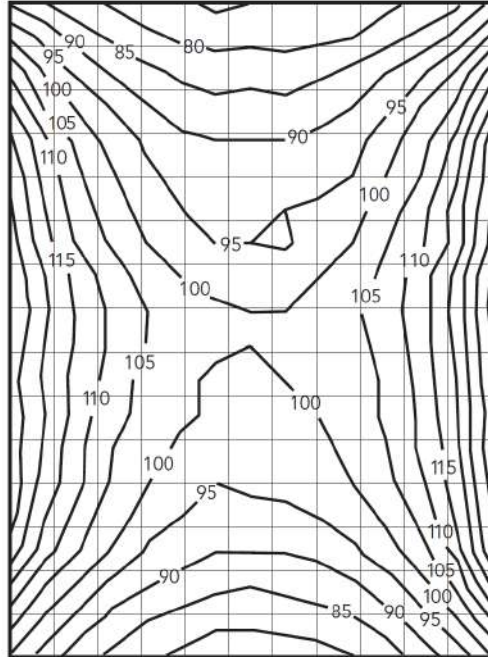
Normalized to 100% at the centre of the canister

Figure 2.11: Typical isodose distribution in air in a Gammacell 220E chamber (source: MDS Nordion)

which would expose it to higher dose rates if it was simply held in air, according to figure 2.11. Figure 2.12 shows the two configurations that need to be compared : the configuration where the chamber only contains air on the left, which is the configuration for which the dose rate is known, and the configuration with the chamber containing the dewar and the spool for absorption spectroscopy.

To accurately estimate the ratio between the given calibrated data (dose rate in air at the center) and the actual dose rate that the fiber samples will receive, we performed a simple Monte-Carlo simulation of photon transport in the chamber using the OpenMC Python simulation package. We will first present the geometrical assumptions that were made to simplify the system to model (2.5.2), then describe the materials that were modeled, and the method used to calculate dose rate (2.5.3). Finally, in section 2.5.4, we present how the simulation and tallies were parametrized, and the results obtained are discussed in 2.5.5. The complete simulation code for this section is attached in appendix D.

2.5.2   Geometrical assumptions

For the Monte-Carlo photon transport simulation, we chose to model only the space inside the Gammacell chamber with, outside this space, a fixed gamma source made of 48 cylindrical pencils in vacuum. As the diameter of the pencils is unknown, we assume that the source cylinders touch their neighbors on the 20.91 cm diameter pitch circle.

Figure 2.13 represents the geometry adopted for the simulation within inside the Gammacell chamber. We do not represent the screws and nuts, the polystyrene foam and plastic
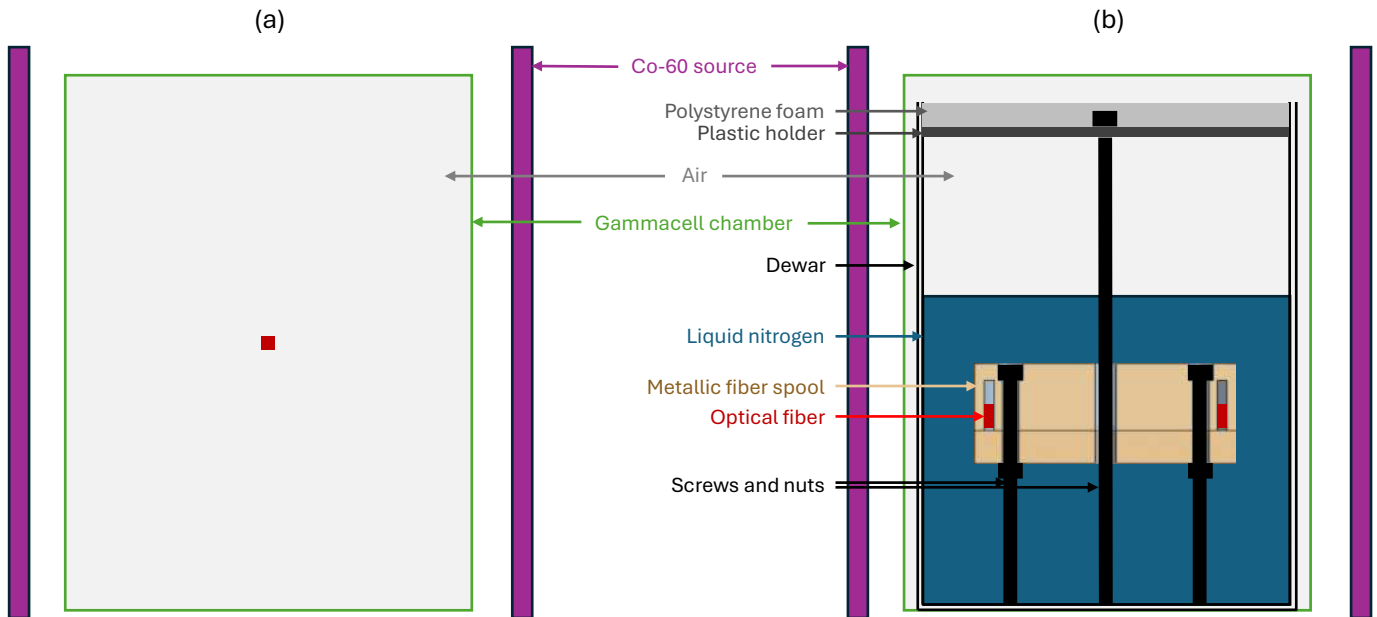
Figure 2.12: Two configurations to compare : (a) Chamber containing only air (the calibrated central dose rate is given for the position represented by a red square), (b) Chamber containing the liquid nitrogen dewar and the fiber spool for absorption spectroscopy.

top of the spool holder or the bottom of the dewar, as the source geometry favors radial exposure. The sample is considered as a 1 cm high rectangular torus occupying the bottom of the spool sample cavity. The liquid nitrogen level can vary. The dewar wall thicknesses were obtained from the manufacturer and the vacuum insulation thickness was deduced from them. The geometry for this simulation has circular symmetry around the z-axis, making figure 2.13 a comprehensive representation.

2.5.3 Material assumptions and mass-energy absorption coefficients

The material distribution can be found in figure 2.13. The chosen compositions of the steels are chosen as the middle of the ranges specified in the standards for the minor elements (weight fractions):

- Stainless steel SUS304 (dewar) : 70.1725% Fe, 19% Cr, 9.25% Ni, 0.04% C, 1% Mn, 0.0225% P, 0.015% S, 0.5% Si.

- Stainless steel SS316L (spool) : 67.0225% Fe, 17% Cr, 2.5% mo, 0.015% C, 1% Mn, 0.0225% P, 0.015% S, 0.375% Si, 0.05% N.

The rest of the chemical compositions can be found in appendix D. Vacuum is represented as low-density air [4].

---

[4]10^{-6} times the density of air at atmospheric pressure, which is the low end of industrial vacuum. This value was chosen based on the information given by the dewar manufacturer.
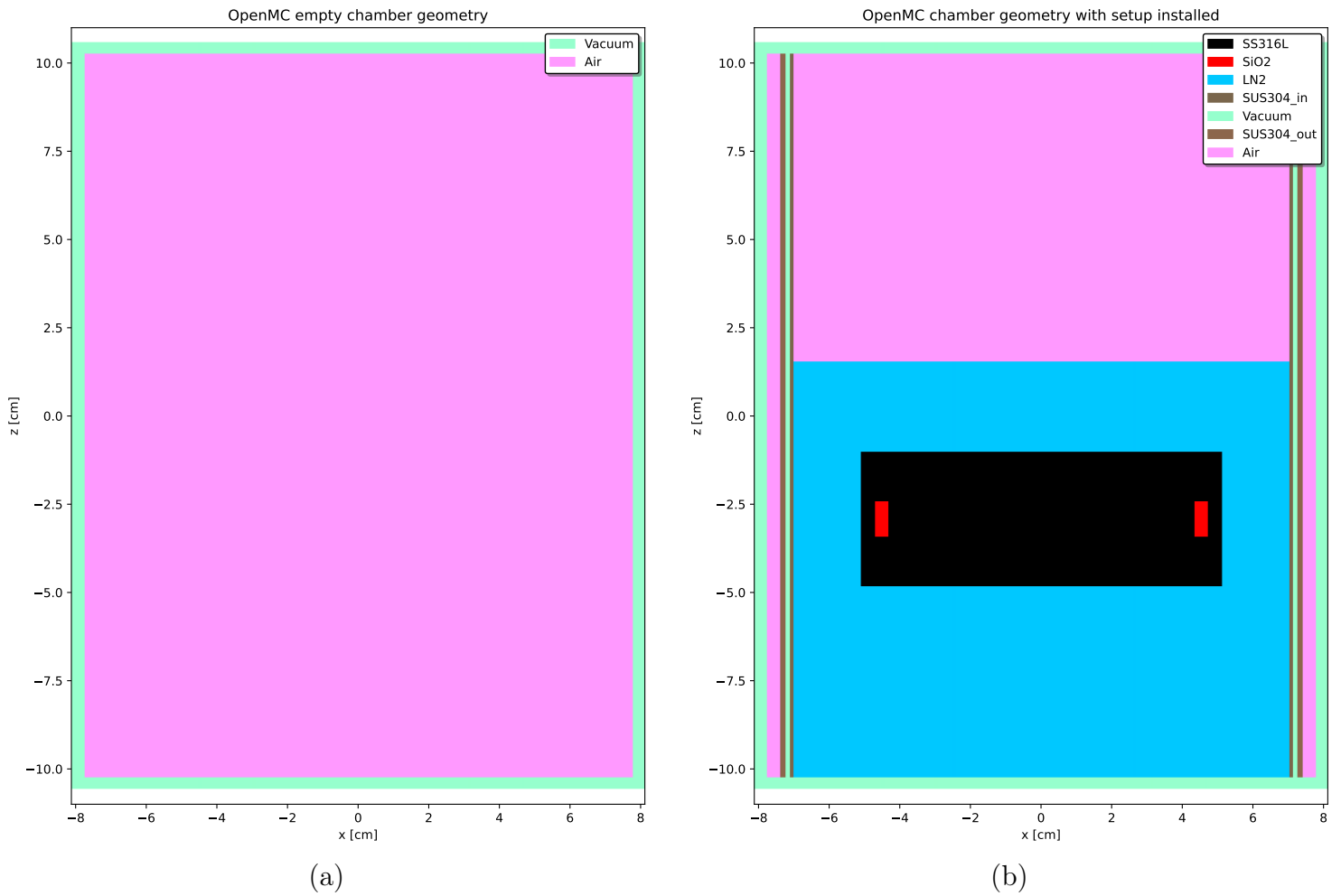
Figure 2.13: Vertical cross-section of the geometry simulated in OpenMC for the two cases, colored by material. (a) Empty chamber for the central dose rate calculation, (b) Chamber with the dewar for the fiber dose rate calculation.

From these material compositions, we calculate the mass-energy absorption coefficient based on the data from the NIST XCOM database [61]. We merged all the lists of energies of the tabulated data, and, at each energy, the sum for each material's mass-energy absorption coefficients $\frac{\mu_{en}}{\rho}$ of every element multiplied by its weight fraction. We obtain a material mass-energy absorption coefficient $\frac{\mu_{en}}{\rho}$ which can be used to tally the dose rate in each material. These calculated coefficients are plotted in figure 2.14.
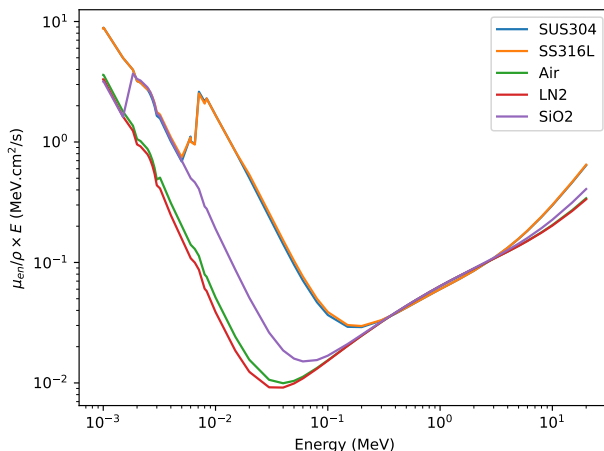
Figure 2.14: Mass energy absorption coefficients multiplied by energy as a function of energy for each material, based on the NIST XCOM database [61].

2.5.4 OpenMC simulation settings for dose rate tallying

The source previously described is set at 667.5 TBq (Source: MDS Nordion for a 15kGy/h Gammacell), distributed uniformly in the 48 pencils, with an isotropic angular distribution, and a discrete distribution over the two main Co-60 decay gamma rays (1.1732 and 1.3325 MeV [62]). The fixed source simulation was set with 200 batches and 10^5 particles per batch. For this estimation of the dose rate, we set the temperature of the cold materials (inner wall, liquid nitrogen, spool, and sample) to the minimum temperature of 293.15 K, independently of the density, as the nuclear data library (ENDF-B7.1) did not contain cross-sections at cryogenic temperatures for interpolation at 77 K.

We tally the dose rate in a central cell (0.508 cm radius, 1 cm height) for the empty chamber configuration, and in the silica region in the other configuration. This tally is an energy function filter, multiplying the flux tally by $\frac{\mu_{en}}{\rho} \times E$ for all energies. The result is then multiplied by the activity of the source, divided by the cell volume and converted into kGy/h. The important quantity resulting from this calculation is the ratio between the two dose rates, eliminating the importance of the accuracy of these proportionality factors in our case, but the raw dose rates tallied are given for reference.

2.5.5 Results and discussion

In the configuration presented in figure 2.13(a), the central dose rate obtained is 14.76 ± 0.14 kGy/h in air. In the second configuration (2.13(b)), the dose rate obtained in the silica

region is 11.02 ± 0.03 kGy/h. This result does not change in the silica cell when the liquid nitrogen level is at the top of the dewar, and changes to 11.24 ± 0.03 kGy/h when it is at the top of the metallic spool. In the default liquid nitrogen level case, the calculated dose rate in the center is 6.08 ± 0.08 kGy/h in steel, which emphasizes the impact of filling the chamber with materials other than air.

In the rest of this thesis, the actual dose rates in silica using the setup presented in this chapter will be calculated by multiplying the calibrated central dose rate in air by $\frac{11.02}{14.76} = 0.75$. The subscript "act" in Gy_{act} will indicate an actual dose or dose rate as defined here, while doses and dose rates with no subscript will indicate Gammacell calibrated central doses and dose rates in air.

Chapter 3

20K-77K equivalence: can we neglect thermal annealing at and below 77K?

3.1 Motivation and background

For the experiments presented in this thesis, for experimental ease and cost reasons, we decided to use liquid nitrogen and cool the samples down to 77 K instead of 20 K with liquid helium, the operating temperature for SPARC magnets. However, to ensure that the results obtained in these experiments will be applicable to SPARC systems, it is necessary to prove that going from 20 K to 77 K does not affect the kinetics of RIA (no change in defect buid-up and annealing rate) by proving that no thermally enabled evolution of the irradiated glass structure happens below 77 K. To answer this question, Commonwealth Fusion Systems builds an experimental setup to perform tests at 20 K and validate the results obtained at 77 K. In the meantime, we attempted to determine whether the white light spectroscopy setup presented in chapter 2 could be used to prove that no thermal annealing was enabled at 77 K.

In a 1991 EPR study [22], Griscom highlighted that STH annealing started above 130 K and disappeared by 200 K, all of these temperatures being well above 77 K. He added that "it is safe to assume that H^0 diffusion is the sole cause of all thermally activated processes occurring below $\sim$ 130 K since larger atoms and molecules have much lower diffusivities." As the fibers studied here are made from low-OH pure synthetic silica tubes (Heraeus F300), they are less likely to be affected by these hydrogen-related processes.

To investigate the activation of thermal annealing processes at 77 K in the Exail optical fibers samples, we implemented two different approaches. When the spectrum is being probed, the white light sent through the fiber causes optical annealing. To mitigate this issue, as we want to isolate thermal annealing, our first method consists of irradiating one fiber sample for the same amount of time multiple times and waiting for a varying amount of time after irradiation, while keeping the sample cold, before probing the RIA spectrum. This method, presented in section 3.2, aims to show that the RIA spectrum does not evolve if the fiber is kept at 77 K and dark. Furthermore, we will see that it helped us learn about the differences between optical and thermal annealing and the combined importance of optical annealing and trigger timing uncertainties. In a second approach, presented in section 3.3,

we used a narrowband laser to only probe RIA around 1550 nm and see if it would limit optical annealing to negligible levels while probing the spectrum continuously during and after irradiation.

3.2 First method: arbitrary waiting time

3.2.1 Aims and hypotheses

In this experiment, we aim to study how the absorption spectrum of one irradiated optical fiber evolves when kept at 77 K in the dark. As we cannot probe the spectrum without shining light through the fiber, we repeated cycles after fully annealing the fiber, irradiating it for a fixed duration and probing the spectrum only after varying amounts of time, as explained in more details in the following sections. If the annealing step fully returns the glass structure to an equivalent of the pristine fiber structure, this becomes equivalent to observing how the spectrum evolves in time after one irradiation in the dark. We indirectly investigate *a posteriori* how much light-absorbing radiation-induced defects remain in the fiber by comparing its transmission spectrum before each irradiation to its transmission spectrum before the first irradiation.

Our hypothesis is that these spectra will be the same or strongly overlap, meaning that transmission does not increase while the fibers are kept at 77 K with no irradiation and no light shining through them, or in other terms, that there is no thermal annealing at 77 K. If all thermal processes are "frozen" at this temperature, it will then mean that they will also be frozen at lower temperatures and that performing the experiments at 77 K is equivalent to performing them at 20 K.

If we do not see an overlap of the spectra, multiple cases can be checked. If the transmission increases with the waiting time, it would mean that there is thermal annealing at 77 K. If transmission decreases with the waiting time, it would mean that we did not successfully keep the fiber away from the radiation source (which is unlikely, given the arguments presented below). If transmission decreases as the fiber goes through the multiple irradiation cycles, it means that RIA becomes more and more effective, and that the annealing step between the cycles did not bring it back to a glass structure equivalent to that of the pristine fiber: either some light-absorbing point defects remain in the fiber or non-absorbing ("precursor") sites that facilitate the formation of new color centers in subsequent irradiations. If transmission increases as the fiber goes through the multiple cycles, it means that the decay of the source is significant on the experiment timescale: we ensure that it is not by performing each experiment at the same dose rate to a precision of 1 Gy_{act}/min (0.6% of the dose rate).

3.2.2 Description of the method

In this first experiment, using the experimental setup presented in chapter 2, we irradiated an 18.2-meter long spool (29.6 m including the fiber ends coming out of the spool) multiple times for 10 minutes in the Gammacell at 181 Gy_{act}/min. Experiments 1.x and 2.x were performed over a four-day period; therefore we neglected the decay of the dose rate. Between

irradiations, we waited for a varying amount of time with the sample kept cold, dark and with no irradiation (Gammacell chamber in its upper position) before probing the transmission spectrum. We then let it optically anneal until the spectrum stabilized. The different irradiations are numbered from 1.a to 1.c and from 2.a to 2.f in the order they were performed, and the sample was thermally annealed at room temperature back to its original transmission spectrum between 1.c and 2.a. Table 3.1 summarizes the different steps of this experiment.

3.2.3 First results and discussion

Figure 3.1 shows the first transmission spectra obtained after irradiations 1.a to 1.c and the corresponding waiting times. These spectra do not overlap and, as the fiber goes through the multiple irradiations, the transmission spectrum gets weaker (RIA is higher). No additional RIA is built up during the waiting time, because the Gammacell is designed so that the dose rate in the upper position of the chamber is sufficiently low for the user to access it and because we do not observe RIA in the fiber samples that we place in the chamber before moving it down. A possible explanation is that the white light optical annealing step between the 3 experiments did not anneal the glass structure back to an equivalent of its pristine structure. Precursor sites, weakly or not absorbing, may be left in the glass structure and facilitate RIA build-up for subsequent irradiation. This prevents us from concluding on thermal annealing with these 3 experiments. However, experiments to follow in the next section will allow us to do so, with thermal annealing intermediate steps and light source synchronized triggering.

Figure 3.2 shows the first transmission spectra obtained after irradiations 2.a to 2.f and the corresponding waiting times. We observe that, indeed, no matter how the waiting times vary, transmission seems to decrease as the total irradiation dose increases from 2.a to 2.c. After 2.c, the post-waiting time spectrum stabilizes, which may mean, in the precursor site hypothesis, that precursor site creation reached a saturation level.

Nonetheless, if we look closely at the results for 2.c to 2.f, the transmission does not decrease monotonically as the total irradiation dose increases. A possible explanation for this small uncertainty may arise from figure 3.3. In this figure, we compare the first full transmission spectra probed, previously shown in figure 3.2, with the preceding spectra, during which the waiting time ended and the light source was turned on. Indeed, to measure the spectra after the waiting times, we kept the spectrometer in permanent sweeping mode, and turned on the white light exactly at the end of the planned waiting time. However, as sweeping is not instantaneous (it is done from left to right in 1.813 s, with a period of 2.261 s, which exceptionally increases when a zeroing operation happens), the fiber can be annealed by the light source used to probe it: we see that all first full spectra in figure 3.3 are higher than their preceding spectra. Furthermore, this figure shows that the light is being turned on (vertical jump in transmission) with varying advance times before the first full spectrum is probed. This leads to varying optical annealing durations before the first full spectrum is probed. Moreover, all later experiments show that a correction of the spectra accounting for a longer optical annealing time for the higher wavelength end may be needed. For this particular experiment, to remove this uncertainty, we decided to perform the experiment again while synchronizing the light source triggering with the start of the first next spectrum sweep rather than with the exact end of the waiting time. This iteration

Table 3.1: Experiment summary - Probing thermal annealing at 77 K with arbitrary waiting times - First iteration - 1.a to 2.f - 18.2 m spool, 181 Gy_{act}/min dose rate. The goal is to prove that the RIA spectrum does not evolve when the fiber is kept dark at 77 K by waiting for varying amounts of time after irradiation before probing the spectrum.

Irradiation ID	Irradiation time (min)	Waiting time (min:s)	Temperature (K)
1.a	10	0:00	77
White light optical annealing			77
1.b	10	5:00	77
White light optical annealing			77
1.c	10	10:00	77
White light optical annealing			77
THERMAL ANNEALING			room temperature
2.a	10	5:00	77
White light optical annealing			77
2.b	10	0:00	77
White light optical annealing			77
2.c	10	5:00	77
White light optical annealing			77
2.d	10	10:00	77
White light optical annealing			77
2.e	10	10:05	77
White light optical annealing			77
2.f	10	5:00	77
White light optical annealing			77
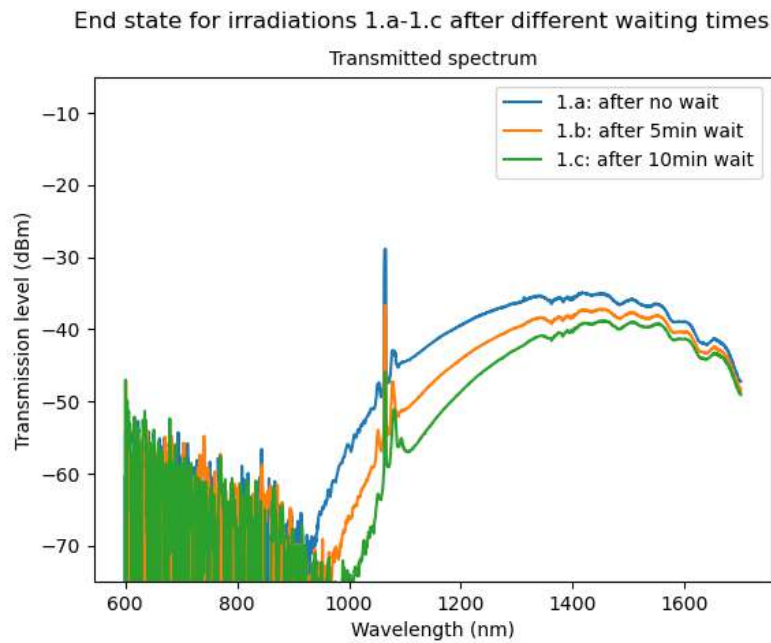
Figure 3.1: Transmitted spectrum of the white light source through the fiber sample at the end of irradiations 1.a to 1.c, first full spectrum probed at the end of each waiting time. We observe that the transmission level decreases with the total irradiation dose or the waiting time (less likely given the aforementioned arguments). Another experiment is needed to separate these two possible causes. If it is the number of cycles, we need to switch from optical annealing to a long thermal annealing step. If it is the waiting time, we need to keep the sample farther away from the source. (see 3.2.1)

Figure 3.2: Transmitted spectrum of the white light source through the fiber sample at the end of irradiations 2.a to 2.f, first full spectrum probed at the end of each waiting time. From the non-monotonically increasing waiting times, we can tell that transmission levels increase with total irradiation dose (number of cycles) and reach a saturation level from 2.c to 2.f. This tends to confirm that the optical annealing step left RIA precursor sites in the glass structure between the different irradiations, and that there may be a saturation of the precursor site formation or annealing mechanisms.
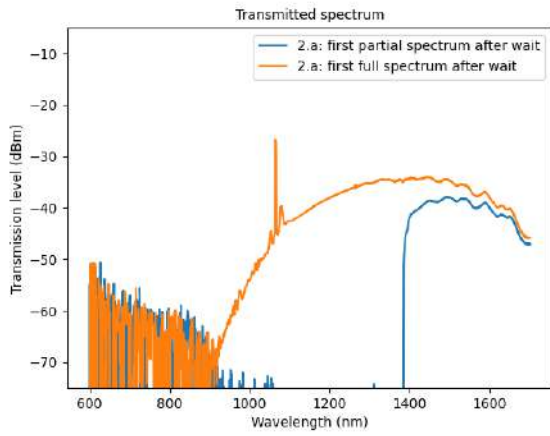
(2.a)
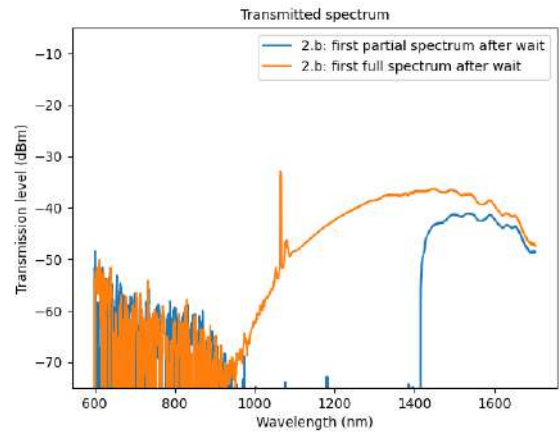
(2.b)
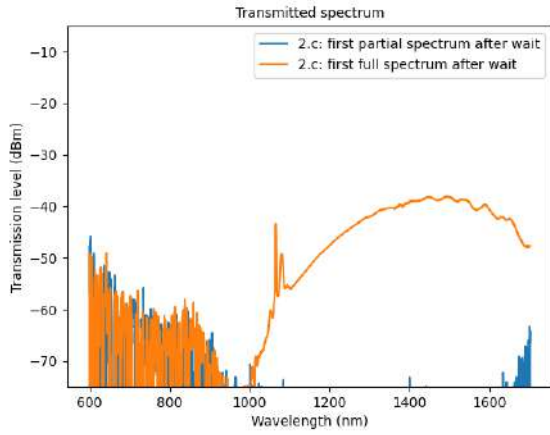
(2.c)
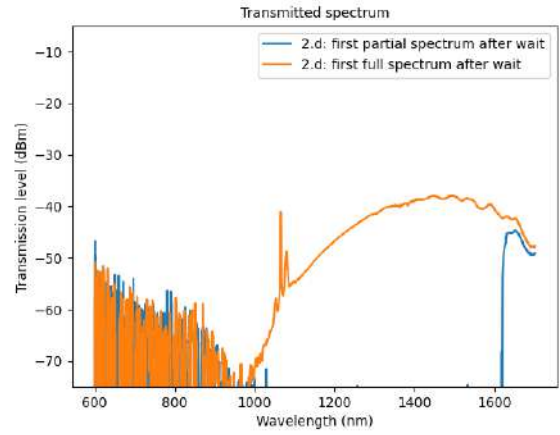
(2.d)
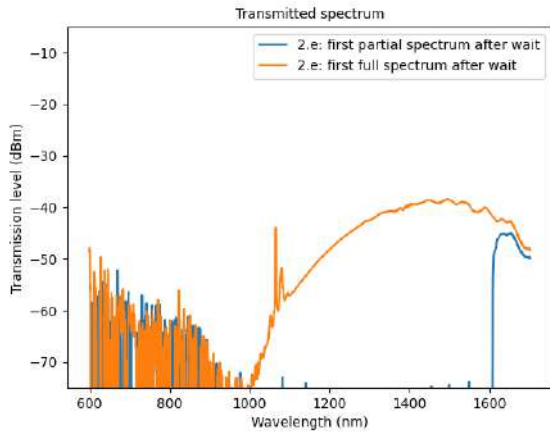
(2.e)
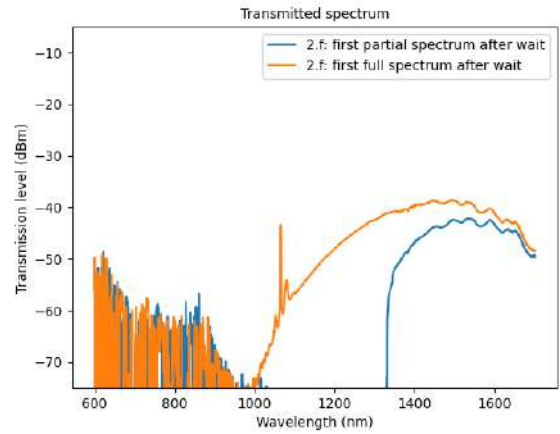
(2.f)

Figure 3.3: Comparison of the first partial white light transmission spectrum probed at the end of the waiting time with the first full spectrum (next sweep) for irradiations 2.a to 2.f. At the end of the waiting time, we simply turn on the light source without synchronizing it with the sweep trigger. This means that the white light is on for a varying duration before the first full spectrum is recorded, optically annealing some fraction of the defects differently in every case. This issue is fixed in the following section.
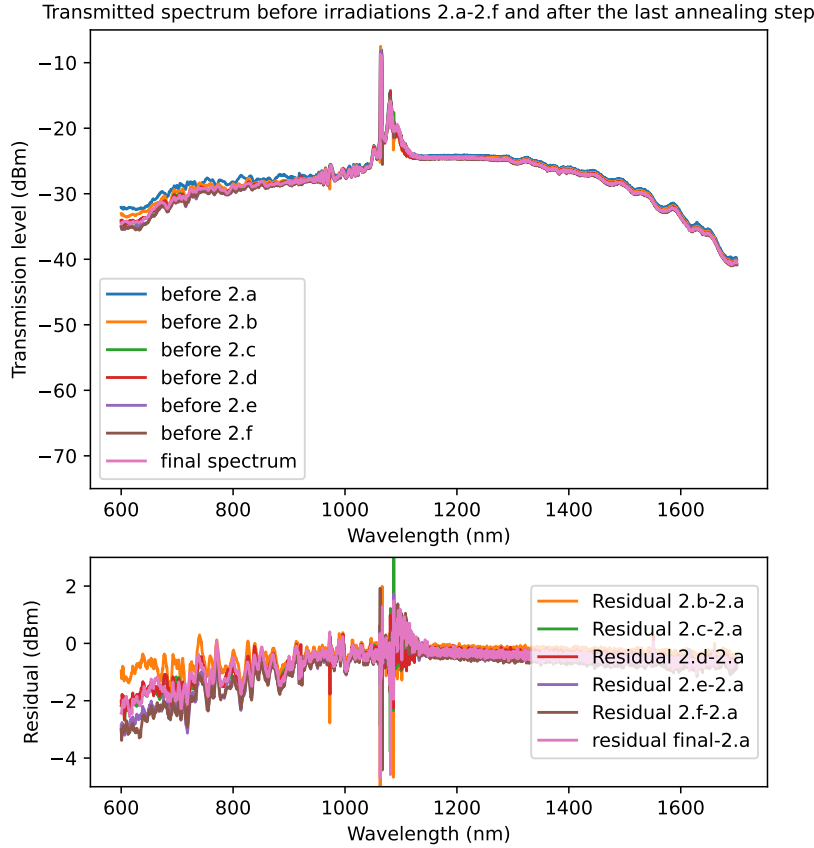
Figure 3.4: Transmitted spectrum of the white light source through the fiber sample before irradiations 2.a to 2.f and at the end of the last optical annealing. There is a good overlap of these initially transmitted spectra at high wavelengths, but the slight difference at low wavelengths may mean that some fraction of the light-absorbing defects remain in the fiber after the optical annealing step.

of the experiment is presented in section 3.2.4.

To further investigate the precursor site hypothesis, figure 3.4 compares the starting transmission spectra, the last probed before the white light is turned off and irradiations 2.a to 2.f start, and the final spectrum after optical annealing. We observe that, even if they had all been stabilized by annealing, they do not perfectly overlap, particularly in the lower wavelengths. Though slight, this difference strengthens the hypothesis that optical annealing does not restore the pristine glass structure, and it may mean that the potential precursor sites absorb mostly at lower wavelengths. This low wavelength remaining absorption may also simply be another type of defect with no correlation to STH. On the contrary, we see very little difference between the first full spectra measured after 1.a and 2.a and shown in figure 3.5(B), with the same irradiation history post-thermal annealing. This difference may be due to the earlier triggering of the light source in 2.a (shown in figure 3.5(A)), which we
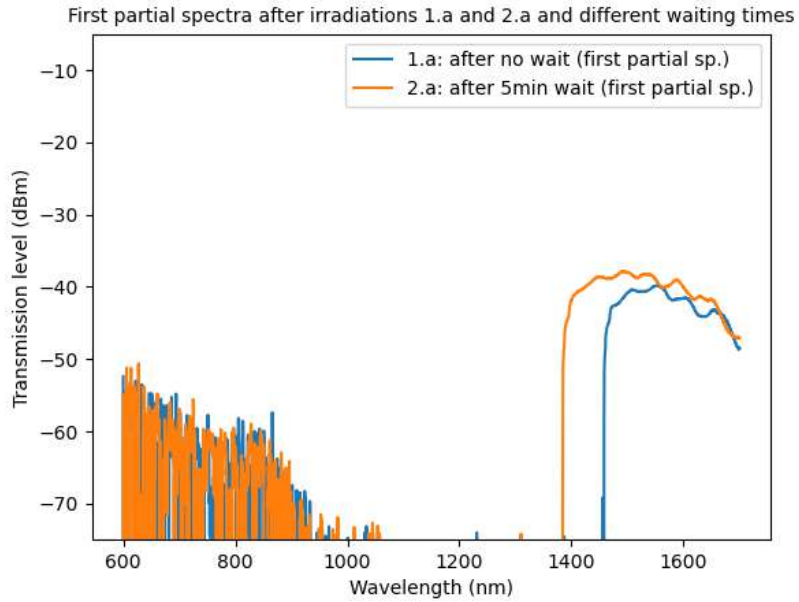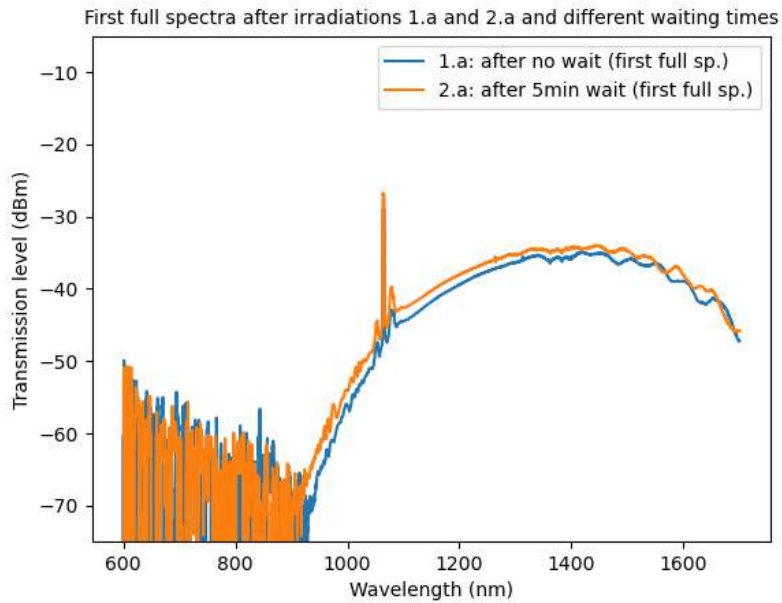
Figure 3.5: Comparison of the transmission spectra measured after irradiations 1.a and 2.a. (A) first partial spectra (B) first full spectra

attempt to determine in .

3.2.4 Synchronized sweeping and light source triggering

To determine whether the difference in optical annealing duration before the first spectrum is acquired is the sole explanation for the absence of overlap in figure 3.5(B), we made a

system to synchronize the lighting of the broadband source with the start of the first next spectrum sweep. This box made with an Arduino Nano board and, as shown in figure 3.6, takes as input the sweep trigger signal from the spectrometer and turns on the broadband light source switch at the start of the first next sweep when the button is pressed.

(a)

(b)
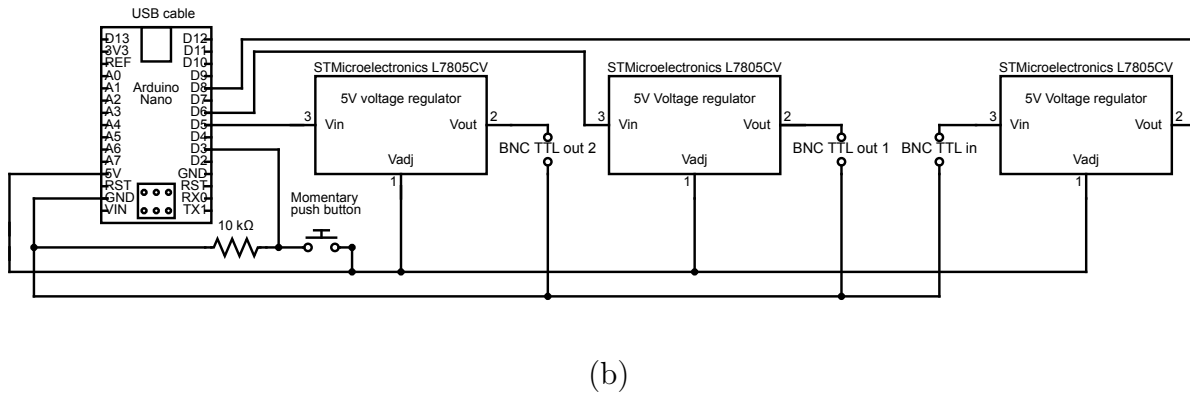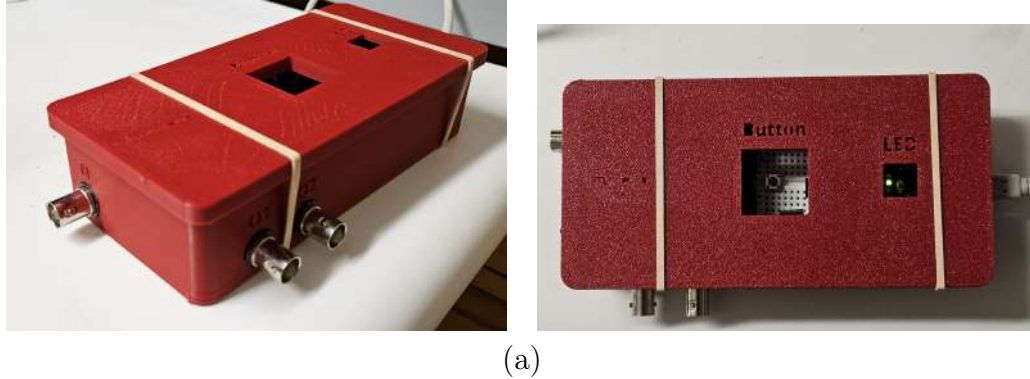
Figure 3.6: TTL trigger box with 1 BNC logic input, 2 BNC logic outputs (only one is needed in this experiment) and a push button. (a) External aspect of the trigger box. (b) Circuit diagram of the trigger box. (Inspired by [63])

With this synchronized trigger, we performed the experiment described in table 3.2. This time, the sample was thermally annealed to room temperature between each irradiation to get rid of the partial effect of optical annealing which may leave precursor sites for RIA build up.

The result of this experiment is given in figure 3.7, which presents the first spectra measured after irradiations a to d and different waiting times. These spectra overlap much better than in figure 3.5 and their difference is not monotonically evolving with waiting time, which confirms the absence of thermal annealing at 77 K and the idea that the main source of difference between 1.a and 2.a in the previous experiment was the unsynchronized lighting which led to uneven optical annealing.

However, from the residual plot at intermediate wavelengths, we still see a very slight increase of attenuation with total irradiation dose, which suggests that the thermal annealing at room temperature that occurred between each of these four experiments may not have been sufficient to fully anneal all the radiation-induced defects.

Figure 3.7: Comparison of the transmission spectra measured after irradiations a to d with synchronized triggering of the white light source with sweep start

Table 3.2: Experiment summary - Probing thermal annealing at 77 K with arbitrary waiting times - Second iteration - a to d - 18.2 m spool, 176 Gy_{act}/min dose rate. Irradiations a and b happened on day 1, c on day 2 and d on day 3. The goal is to prove that the RIA spectrum does not evolve when the fiber is kept in the dark at 77 K by waiting for varying amounts of time after irradiation before probing the spectrum. In this experiment, the fiber is thermally annealed between each irradiation.

Irradiation ID	Irradiation time (min)	Waiting time (min:s)	Temperature (K)
THERMAL ANNEALING			room temperature
a	10	10:00	77
White light optical annealing			77
THERMAL ANNEALING			room temperature
b	10	00:10	77
White light optical annealing			77
THERMAL ANNEALING			room temperature
c	10	05:00	77
White light optical annealing			77
THERMAL ANNEALING			room temperature
d	10	03:00	77
White light optical annealing			77

3.3 Second method: narrowband continuous observation

3.3.1 Aims and hypotheses

While the experiment presented above proves that there is no thermal annealing at 77 K, we would like to perform a second experiment to see if it is possible to monitor continuously a stable RIA spectrum after irradiation in a fiber kept at 77 K. The method for this experiment is presented in the following section. The challenge that led us to design the arbitrary waiting time method is that RIA can be optically annealed, and shining light through the fiber is necessary to directly measure attenuation. We thus wanted to check whether it was possible to limit the optical annealing effects of the probing light source. We know that optical annealing is optimal for photobleaching wavelengths in the low infrared and its effectiveness decreases in the visible and at telecommunication wavelengths [49], [51], [64]. Thus, we only probe the RIA level at the critical wavelength for our application, around 1550 nm, instead of shining a broadband light source, which is why we connect a laser diode to the fiber input. We also try in this experiment to go to the lowest probing power levels that still enable us to monitor the RIA evolution without falling below the OSA noise floor (see figure 2.2).

If these choices are sufficient to limit the effect of optical annealing, we should observe an increase in RIA during irradiation with an evolution profile similar to the ones presented in

[64] and, after irradiation and while keeping the sample fiber cold, an attenuation plateau. If we instead observe a decrease of RIA after irradiation, this will mean that annealing still takes place and, from what we concluded in our previous experiment (3.2.4), that it is optical annealing. This would mean that we cannot perform any non-destructive[1] measurement of attenuation in our test setup and would give important information on optical annealing contribution to the results presented in chapter 4.

3.3.2   Description of the method

To complement the results from section 3.2, this method attempts to determine whether only probing RIA at high wavelengths would limit the optical annealing effect enough to observe a stable attenuation over multiple sweeps after irradiation, when keeping the sample at 77 K. We added a narrowband 1550 nm light source in the spectroscopy setup to this end, as presented in 2.1. As this fiber-pigtailed laser (Thorlabs LPS-1550-FC) includes a photodiode, it is operated at constant power and constant temperature (25°C). The spectrum of this light source through the absorption spectroscopy setup is given in figure 3.8.
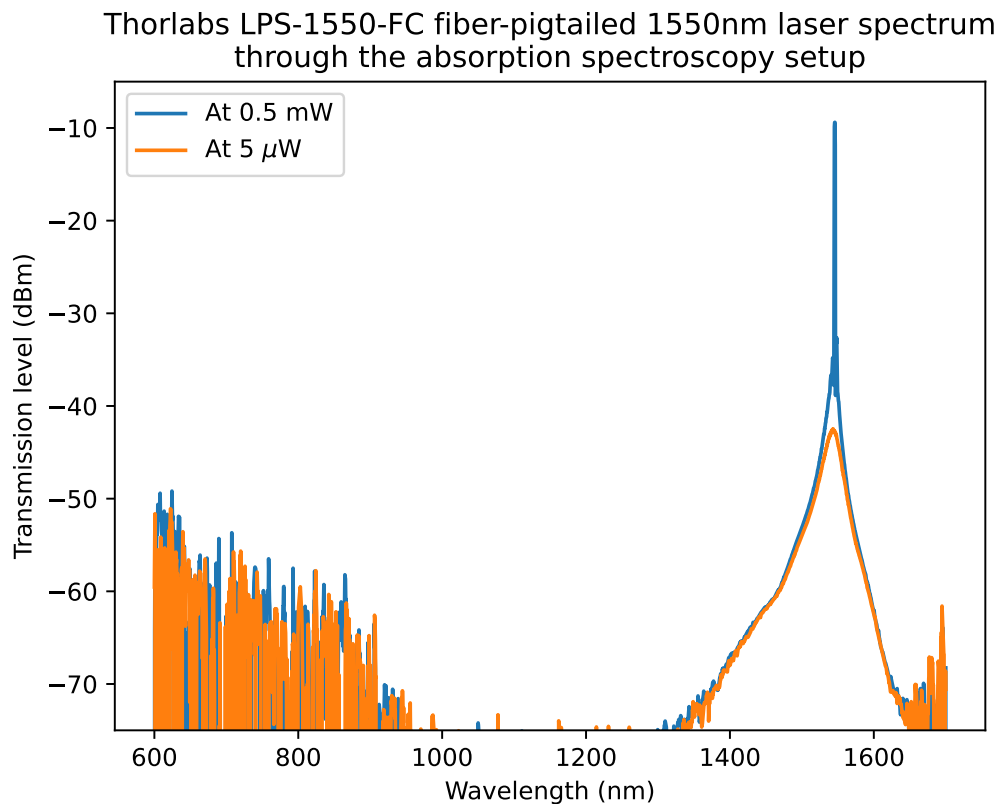
Figure 3.8:   Spectrum of the Thorlabs LPS-1550-FC light source through the absorption spectroscopy setup at 2 operating powers (0.5 mW and 5 μW).

To perform this experiment, we prepare a 18.24 m long sample and, while looping over

---

[1]Which does not optically anneal the light-absorbing point defects

the spectrum with the 1550 nm light source turned on, we irradiate the sample for 45 minutes at 176 Gy_{act}/min immersed in liquid nitrogen, and then keep it in liquid nitrogen after the end of the irradiation, in the upper position of the Gammacell chamber.

To obtain the RIA profile over the course of the experiment, we subtract every spectrum from the initial transmission spectrum and average the difference over all the points in the [1540, 1560] nm interval. We compare this RIA evolution for two different operating powers, 0.5 mW and 5 μW, the latter being on the low end of stable operating powers reachable with the light source while giving a spectrum sufficiently intense compared to the noise floor in our different experiments. Between these experiments, the fiber is thermally annealed overnight at room temperature. Figure 3.9 compares the white light source spectrum through the sample fiber before these two experiments. Before the second experiment, we notice that the fiber transmission is not completely recovered at low wavelengths, which could lead to a slightly faster defect build-up during irradiation, as seen in the experiments previously discussed. However, we here focus on whether the RIA level decreases after irradiation, and not necessarily on how it increases during irradiation.

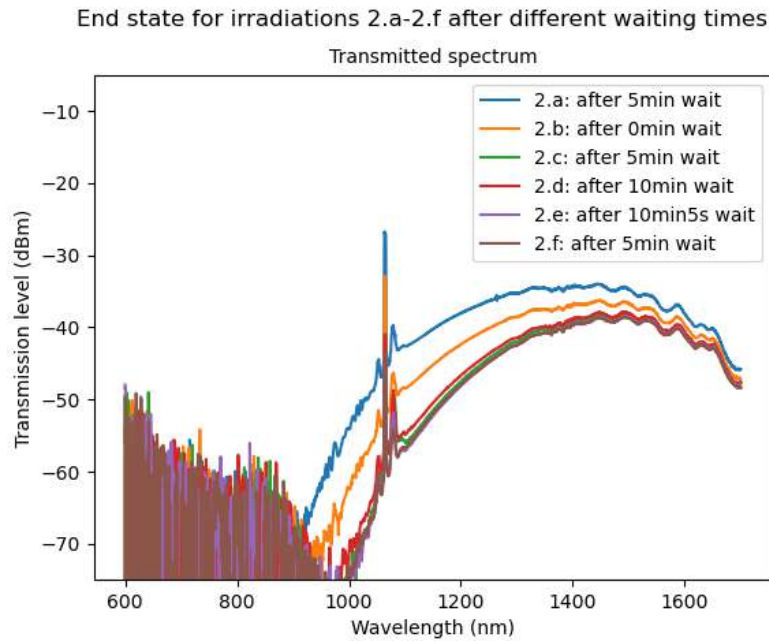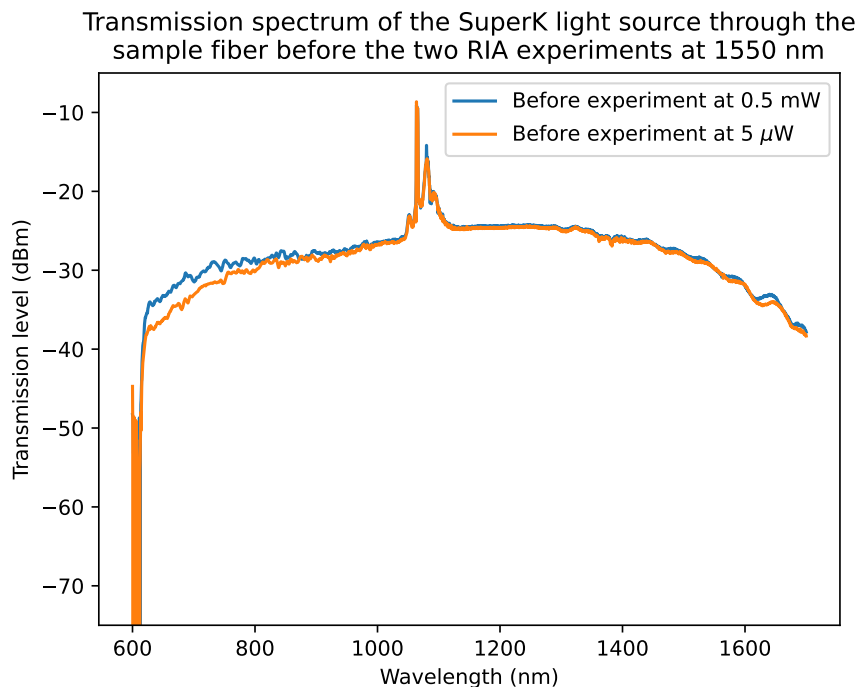Figure 3.9: Transmitted spectrum of the white light source at full power probed once before the beginning of each irradiation cycle of the experiment probing annealing around 1550 nm at two different powers. Before the second experiment, we notice that the fiber transmission is not completely recovered at low wavelengths.

3.3.3 Results and discussion

The results of these two experiments are shown in figure 3.10. After irradiation, we notice that the RIA level does not remain stable, which means that, even at 5 μW, the probe

light source optically anneals the radiation damage. Similarly to what was observed by Fernandez et al. [51] for secondary optical annealing light, the RIA level increases faster during irradiation for the lowest probe light power. This is because, as defects are created by irradiation, the probe light source anneals them faster at higher power. The small periodic peaks that can be seen during irradiation are due to zeroing operations of the spectrometer, during which the interval between two spectrum sweeps increases and RIA builds up faster as no light is circulated through the fiber.

Because of the impact of optical annealing even for a light source at high wavelengths and low power, this experiment cannot be used to confirm the results from 3.2.4 on the absence of thermal annealing at 77 K.

However, they help us understand the inevitable optical annealing rate that will impact other experiments performed in chapter 4. In figure 3.11, we plot the annealing rate, defined as $-\frac{\mathrm{d}RIA}{\mathrm{d}t}$, as a function of the RIA level during the post-irradiation annealing steps of these two experiments after downsampling using local linear fits to smooth the derivative. The optical annealing rate seems to increase exponentially[2] with the RIA level[3], with different coefficients depending on the light source power. Furthermore, we note that these results tend to indicate a saturation of the optical annealing effects preventing fiber transmission from going back to its pre-irradiation level and supporting the first observations made in figure 3.4. We draw no further conclusion at this point on the modeling of optical annealing at 1550 nm, and future work should focus on furthering investigation on power dependence. This question is one of the focus points for the full modeling of thermo-optical annealing in fibers, which we started investigating in this work and particularly in chapter 4.

---

[2]Except for the data point at the highest RIA in both experiments

[3]It should be noted that RIA is here strongly correlated with time, and this fit is more an observation than a very broad conclusion.
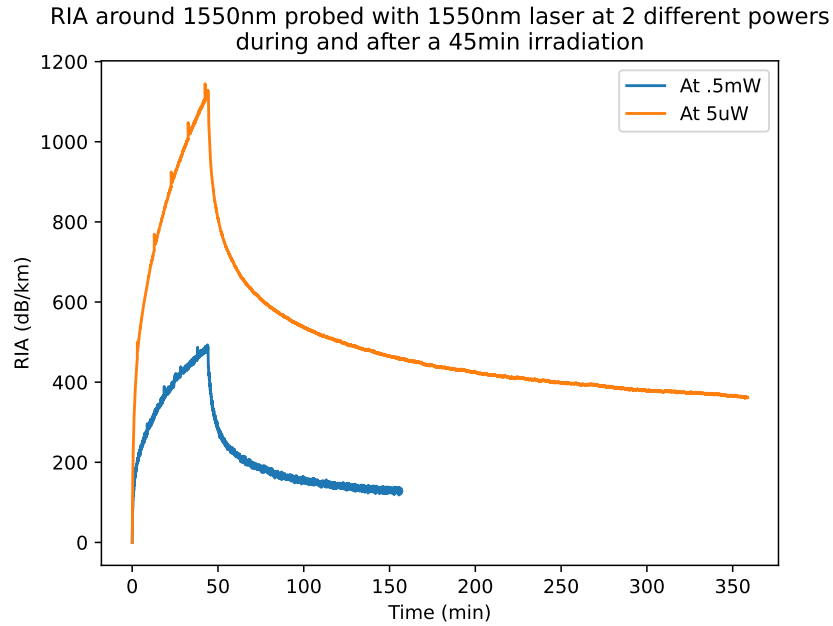
Figure 3.10: Evolution of the mean RIA level between 1540 nm and 1560 nm during and after a 45 min irradiation at 176 Gy$_{\text{act}}$/min, probed with the Thorlabs LPS-1550-FC laser diode at 2 operating powers (0.5 mW and 5 μW). The fiber is kept at 77 K for each experiment.
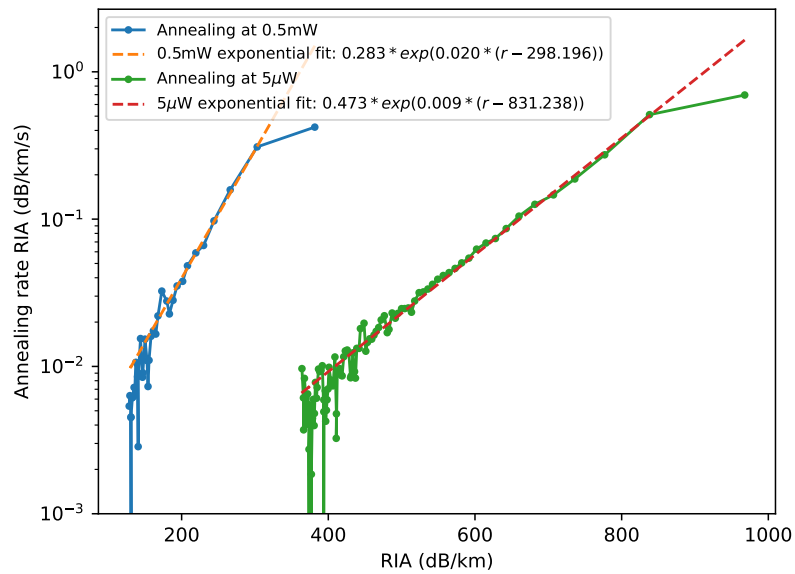
Figure 3.11: RIA optical annealing rate $(-\frac{\mathrm{d}RIA}{\mathrm{d}t})$ after irradiation as a function of the RIA level for the experimental results presented in 3.10.

3.4 Conclusion

In this chapter, we aimed to investigate with the absorption spectroscopy setup presented in chapter 2 whether thermal annealing was essentially "frozen" at liquid nitrogen temperatures, meaning that it would not matter on the RIA evolution rates and defect stability whether experiments are performed at 77 K or 20 K.

In the first experiment, we probed the white-light transmission spectrum of an optical fiber after a fixed-duration irradiation and varying waiting times, to reconstruct the evolution of RIA when an irradiated fiber is kept in liquid nitrogen and in the dark. Based on this experiment, we concluded that the RIA profile did not evolve under these conditions, confirming our hypothesis that thermal annealing would not have an impact. We observed a slight increase in attenuation as the fiber underwent multiple cycles of irradiation, indicating that the fibers may not have been perfectly thermally annealed between the irradiation steps. This could be confirmed by increasing the thermal annealing time between each experiment to multiple days.

In the second experiment, we continuously probed the RIA spectrum around 1550 nm during and after irradiation, at 77 K, and for 2 optical annealing powers. These tests showed that, even at a probe power of 5 μW, optical annealing had a significant impact. We calculated the annealing rate for these experiments, which seems to increase exponentially with the RIA level, in order to compare them with subsequent experiments.

In the next chapter, we decompose the different defect contributions to radiation-induced attenuation spectra and continue the exploration of RIA kinetics.

Chapter 4

Decomposing the mechanisms and kinetics of RIA with white light absorption spectroscopy

4.1   Motivation and background

This chapter focuses on the experimental efforts to better understand multiparameter kinetics of RIA, using the absorption spectroscopy setup presented in chapter 2, and to relate it to the radiation-induced point defects discussed in chapter 1.

Indeed, to be able to predict the RIA evolution in the optical fibers of the SPARC quench detection system, various scenarios must be tested experimentally to support modeling efforts. Commonwealth Fusion Systems led a first series of tests measuring attenuation specifically at 1550 nm in various irradiation, thermal and optical annealing conditions[1]. The experiments reported in this chapter attempt to better understand what defects are the main source of attenuation in the Exail IXF-RAD-SM-1550-014-PI optical fibers by performing Gaussian decomposition on the continuous absorption spectra obtained, as explained in 4.2.3. Understanding the shape and kinetics of the absorption bands helps expand the data obtained at 1550 nm and better predict how other wavelengths, including the chosen optical annealing wavelength, will be absorbed by the fiber.

More than just the initial RIA build-up kinetics needs to be tested in order to improve RIA predictive models. While decomposing the spectra observed to improve the analysis of the microscopic mechanisms, multiple questions must be addressed:

(a) How does RIA evolve when the optical fiber is warmed up? How does it depend on the warm-up rate or the maximum temperature reached, as these parameters could induce operational constraints? Answering this question is necessary to design optimal outages aiming at restoring fiber transmission.

(b) As a fiber undergoes thermal annealing cycles, do the RIA build-up or annealing kinetics evolve? Can this be detrimental to long-term operation of a system like the quench

---
[1]Proprietary data

detection system? These questions are essential to make sure that the chosen restoration plans do not have a significant negative impact on RIA build-up during subsequent irradiations, as would be the case if precursor sites are left in the post-annealing glass structure.

(c) What are the kinetics of optical annealing? How does it evolve if it is used continuously or only after irradiation? How does its effectiveness vary with optical power? The goal is to answer these questions for fixed wavelengths, as they are the main candidates for optical annealing during fiber operation, and not for white light annealing, so that the results directly apply to the SPARC system. This will help choose the optimal light source, optical annealing parameters and quench detection system design to maximize the allowed operation time between two thermal annealing outages.

(d) How does the RIA response to optical annealing evolve with total irradiation dose or cycles? This can help plan multiple operational cycles and the consequences of optical annealing source failures.

(e) When used jointly, how do thermal annealing and optical annealing combine in terms of RIA response? As these techniques will most likely be used in conjunction, understanding their joint usage requires bridging the gap between independent models of thermal and optical annealing.

(f) Contrary to thermal annealing that happens at the same rate in the entire spool in our experimental setup, optical annealing is asymmetrical as the laser enters on one end of the fiber and is attenuated as it passes through the fiber. Therefore, what is the impact of fiber length on optical annealing? This can lead to limitations on the length of fibers that can be used for the quench detection system, in relation to the optimization of optical annealing parameters.

The following section presents the experiments designed to begin answering these questions and complement the existing literature.

4.2   Method

4.2.1   Aims and hypotheses

The kinetics of thermal annealing from cryogenic temperatures to room temperatures after irradiation yet lack extensive study[2]. Thus, we decided to focus on studying this post-irradiation thermal annealing. Indeed, since we have seen in the previous chapter that the effects of optical annealing tend to saturate (from both white light and 1550 nm laser diode annealing), downtimes in reactor operation may be necessary to warm up the fibers and thermally anneal the radiation-induced defects. There is a strong economic incentive to optimize such potential downtimes, because they would require stopping electrical production. Therefore, understanding the kinetics of thermal annealing is crucial.

---

[2]For studies on the RIA build-up kinetics at cryogenic temperatures, one can refer to [64] and [51].

To this end, we perform multiple irradiations at 77 K while probing RIA around 1550 nm and, during post-irradiation warm-up, we investigate the evolution of the thermal annealing rate as a function of time, temperature and RIA level, at two different warm-up rates. We expect to observe an activation of thermal annealing processes as temperatures go over the stability limits of different kinds of defects. For example, if self-trapped holes are part of the RIA contributors, based on studies by Griscom et al. [22], we expect to see activation of their annealing at around 130 K. If annealing is mostly driven by temperature, we would expect an increase in the annealing rate constant as temperatures increase, with increases starting at certain defects' stability temperatures. However, as concentration of light-absorbing centers will decrease during the annealing process, if it starts being a limiting factor, we expect to mostly see a strong correlation of annealing rate with RIA level (directly related to the concentration of defects).

These observations will be complemented by a decomposition of the attenuation spectrum to identify the main point defects responsible for RIA in the fibers[3] under study under gamma irradiation.

4.2.2   Description of the scenarios probed

In order to not perturb the post-irradiation thermal annealing kinetics with a white light measurement, we decided arbitrarily to choose a spectrum from the experiment presented in 3.2 for our decomposition of RIA into defect contributions. This decomposition is presented in 4.3.1.

Table 4.1 summarizes our thermal annealing kinetics measurements. We irradiate a 41.4 m long sample 5 times for 14 minutes at 175 Gy_{act}/min. Before steps k and n (fourth and fifth cycles), the sample is annealed overnight. For the first three cycles, the sample is warmed up in its metallic spool in ambient air. For the last two, in order to reach slower annealing rates and a better low-temperature resolution, the sample is warmed up in its metallic spool in the cold dewar emptied of its liquid nitrogen content after irradiation. The RIA level is probed the same way as in 3.3, with the Thorlabs fiber-pigtailed 1550 nm laser diode, and averaged over the $[1540, 1560]$ nm range.

4.2.3   Spectrum processing and decomposition method

To extract the radiation-induced attenuation spectra from the raw spectrometer data and perform a decomposition over different defect contributions, multiple steps are required. The Python code associated with the procedure reported in this section can be found in appendix E with details on the chosen parameters.

First, for each transmission spectrum recorded, the part that does not fall below the noise floor is isolated. To achieve this, as the signal strongly oscillates where the spectrum reaches the noise floor, a test is performed on the neighborhood of each point of the spectrum from the lowest wavelengths to the highest. If, in the neighborhood of this point, a data point falls below a certain transmission level, the data point is considered to be in the noise region. In the data gathered during these experiments, the part of the spectrum that falls below

---

[3]Exail IXF-RAD-SM-1550-014-PI: pure silica core and 0.5 w% F-doped silica cladding.

Table 4.1: Experiment summary - Post-irradiation thermal annealing kinetics at different warm-up rates - 41.4 m spool, 175 Gy_{act}/min dose rate, sweeping period 2.261 s, sweeping time 1.813 s. This experiment is performed to record thermal annealing kinetics around 1550 nm after multiple cycles of irradiation at 77 K with different warm-up rates and annealing times. Steps a, d, g, k, and n correspond to the cool-down steps before irradiation. Steps b, e, h, l, and o are the irradiation steps, which can give us information on whether the RIA build-up kinetics evolves as the fiber undergoes multiple annealing cycles. Steps c, f, i, m, and p are the post-irradiation warm-up steps during which we probe RIA as it is thermally annealed, m and p being overnight (end of these steps not recorded, past a certain number of sweeps). Step j is an overnight warm-up to room temperature (not recorded).

ID	Irradiation	Target (min:s if duration)	Temperature (K)	Optical annealing	Full spectrum probing times
a	No	Temperature	$\longrightarrow$ 77 K	Probe (5 μW)	At the end
b	Yes	14:00	77 K	Probe (5 μW)	Never
c	No	Temperature	$\longrightarrow$ 275 K	Probe (5 μW)	Never
d	No	Temperature	$\longrightarrow$ 77 K	Probe (5 μW)	At the end
e	Yes	14:00	77 K	Probe (5 μW)	Never
f	No	Temperature	$\longrightarrow$ 275 K	Probe (5 μW)	Never
g	No	Temperature	$\longrightarrow$ 77 K	Probe (5 μW)	At the end
h	Yes	14:00	77 K	Probe (5 μW)	Never
i	No	Temperature	$\longrightarrow$ 251 K	Probe (5 μW)	Never
j	No	Temperature	$\longrightarrow$ Room temperature	None	Never
k	No	Temperature	$\longrightarrow$ 77 K	Probe (5 μW)	At the end
l	Yes	14:00	77 K	Probe (5 μW)	Never
m	No	Temperature (slow warm-up)	$\longrightarrow$ Room temperature	Probe (5 μW)	Never
n	No	Temperature	$\longrightarrow$ 77 K	Probe (5 μW)	At the end
o	Yes	14:00	77 K	Probe (5 μW)	Never
p	No	Temperature (slow warm-up)	$\longrightarrow$ Room temperature	Probe (5 μW)	Never

the noise floor is always the low wavelength end (higher attenuation), and the portion at higher wavelengths than the first data point not in the noise region is kept. If the portion kept is not significant (number of data points below a fixed number), the whole spectrum is discarded for the rest of the absorption spectrum calculation.

Then, on the portion of the transmission spectra that is kept, a modified sinc filter is applied, following recommendations from Schmid et al. on "why and how Savitzky-Golay filters should be replaced" [65]. In particular, this filter improves the behavior near the boundaries of the data. To calculate, the absorption spectrum, the difference between the filtered spectrum recorded at the beginning of the experiment (before the first irradiation) and the current filtered spectrum is calculated on the current spectrum wavelength range.

Finally, using the list of possible attenuation contributions reported in section 1.3.2 and figures 1.6-1.7, we use a non-linear least squares algorithm (the `curve_fit` from `scipy.optimize`) to fit the spectrum with a combination of these absorption bands, letting the full-width at

half maximum (FWHM) be a free parameter when it is not known from the literature. The whole set of data from the literature on the absorption bands that are used for the decomposition is included in the appendix E code.

Possibilities for improvement include giving some optimization margin for the strictly fixed parameters known from the literature and restraining the optimization ranges for the FWHM when it is unknown.

Finally, even if reports tend to indicate that radiation-induced defect luminescence mostly happens in the UV range [15], in order to make sure that the transmitted spectrum was not the result of both radiation-induced attenuation and emission, an experiment was performed with a fiber connected to the spectrometer without any light source. While irradiating the fiber to 15 kGy at 77 K, no luminescence signal was recorded above the noise level on the spectrometer, confirming that it could be ignored in the rest of our experiments.

4.3   Results and discussion

4.3.1   Decomposition of the RIA spectrum into defect contributions

Figure 4.1 presents the result of the Gaussian decomposition obtained for the RIA spectrum corresponding to spectrum 2.d in figure 3.2.

We note that the fit obtained by this automatic decomposition is very accurate, with a residual multiple orders of magnitude smaller than the spectrum, except at two locations: the intensity peak of the SuperK light source (between 1050 and 1100 nm) and the high wavelength end of the spectrum. The former is due to the peaky aspect of the spectrum in this range[4], which causes an artifact in the smoothed absorption spectrum. The latter may be due to another band such as the LTIRA (see figure 1.6), but its impact in the measured range being very low, fitting it would not be very meaningful.

From this decomposition, the main contributions to the RIA spectrum in the experimental range are STH and the composite 1-eV band, tentatively associated with STH [30]. This makes STH the main defect that should be annealed in order to maintain good performance of the optical fiber sensor at 1550 nm.

It is important to note that, to perform the decomposition, we use the data from the literature without unevenly *a priori* favoring one defect compared to another in the chosen set of defects: the default magnitude of each peak is the same. Furthermore, all peaks are independent for this optimization. The defects taken into account for this decomposition are STH of type 1 and 2, E' centers, ODC of types I and II, NBOHCs, and the composite 1-eV band. Extrapolation of the spectrum at lower wavelengths should not be taken as a prediction of the spectrum where no experimental data was recorded: only the bands that have a significant contribution to the experimental spectrum range should be considered here. We plot all the bands for transparency on the exact result of the fitting algorithm. The fit plotted is the sum of all of the contributions.

---

[4]This peaking is standard for this light source, as shown by the typical SuperK COMPACT spectrum presented in the datasheet. [66]
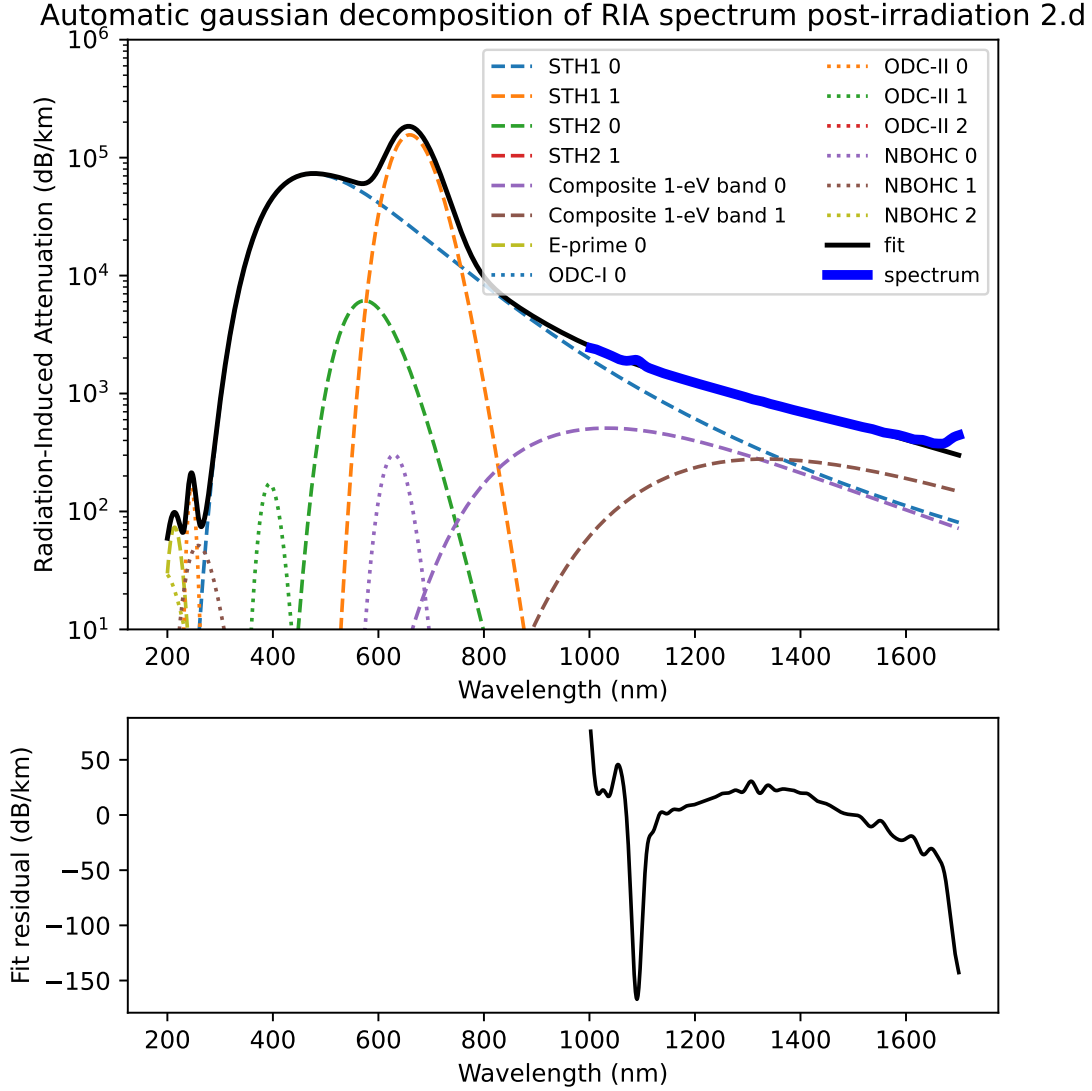
Figure 4.1: Automatic decomposition of RIA spectrum from experiment 2.d (3.2) over the absorption bands of STH of type 1 and 2, E' centers, ODC of types I and II, NBOHCs, and the composite 1-eV band, all presented in figure 1.6. It is worth noting that these bands are Gaussians in energy and that this plot is given as a function of wavelength. The difference between the fit and the experimental spectrum is displayed in the bottom part of the figure. We obtain a good fit over the whole infrared experimental spectral range, mostly based on STH and the composite 1-eV band, which was tentatively associated with STH [30].
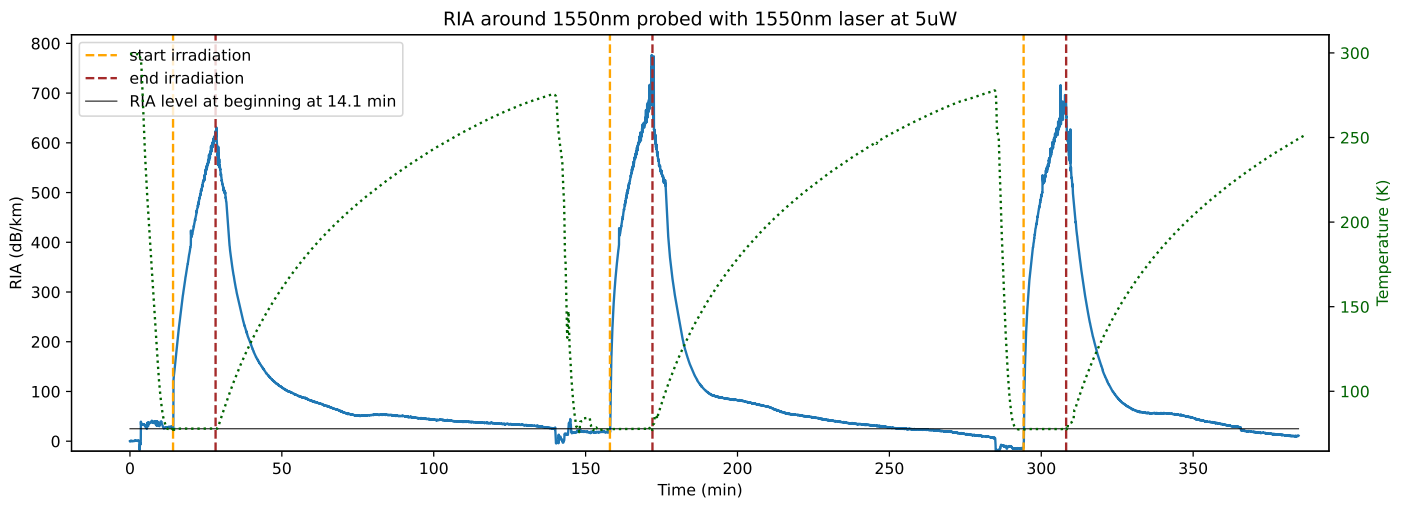
(a-i)
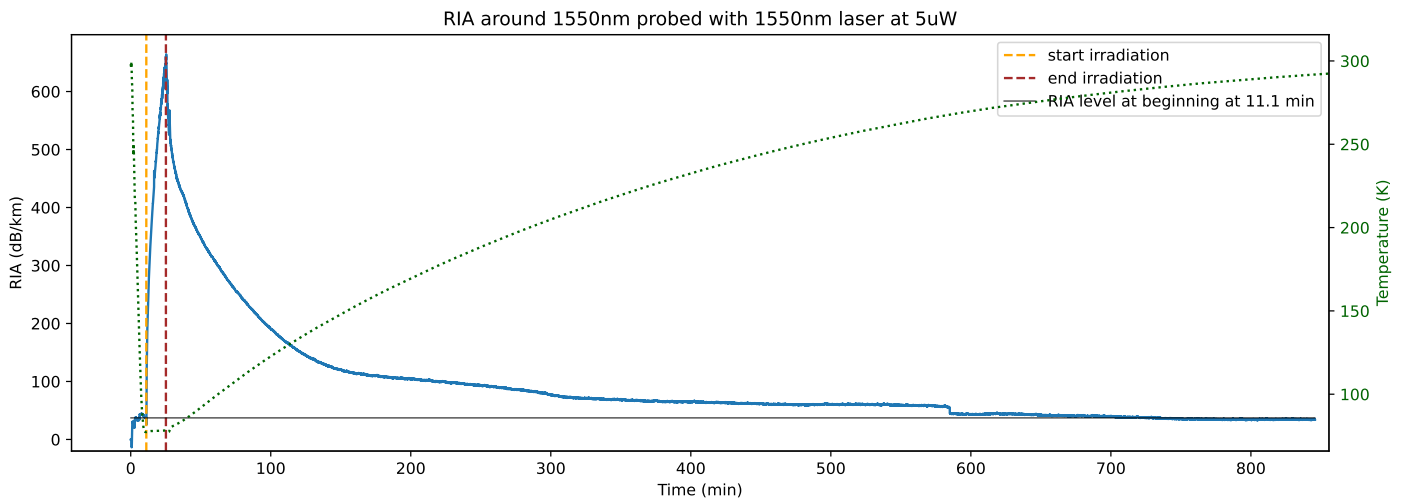
(k-m)
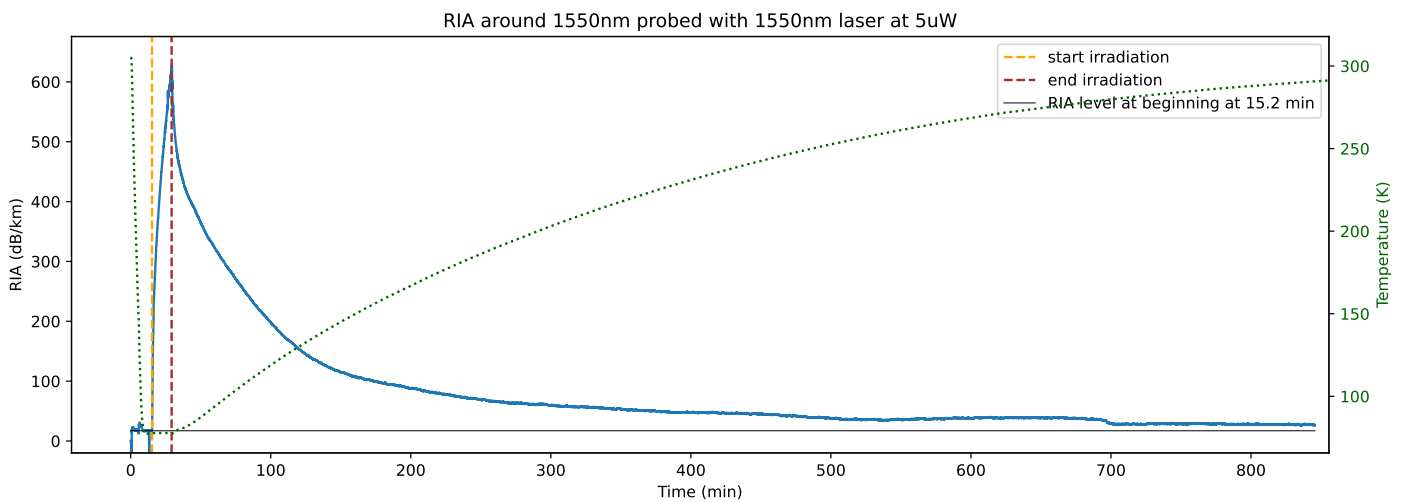
(n-p)

Figure 4.2: Temperature measured by the Cernox sensor (in green) and RIA (in blue, probed around 1550 nm evolution as a function of time for the thermal annealing kinetics experiment, divided between step a to i, k to m, and n to p. Irradiations are all 14 min long at 175 Gy_{act}/min. The irradiated sample fiber is 41.4 m long.

4.3.2 Thermal annealing kinetics

Figure 4.2 presents the thermal annealing experimental results throughout the experiments as a function of time. RIA is calculated based on the transmission spectrum at time $t = 0$ min in each plot. For each subpart of this experiment (a-i, k-m and n-p), the horizontal line corresponds to the RIA level recorded at the beginning of the first irradiation. The highest RIA levels are close to the spectrometer noise floor, resulting in some noise in the calculated attenuation. At low RIA levels, the noise also dominates the difference between the corresponding transmission spectra and the initial transmission spectrum. In the first subplot, we note that the calculated RIA level goes under the level calculated before the first irradiation. The initial step increase in loss between $t = 0$ min and $t = 14.1$ min should be investigated, but this study is not performed in this thesis.

For the first irradiation step in each subfigure, we observe a similar RIA build-up, with a maximum at around 600 dB/km. However, for the subsequent irradiations in the first subfigure (steps e and h), RIA increases faster, indicating that the thermal annealing did not successfully anneal all the defects in the glass structure, leaving light-absorbing point defects or non-absorbing precursor sites that facilitate their creation. Figure 4.3 shows the white light transmission spectrum recorded before the beginning of each irradiation, confirming that none of the annealing steps brought the fiber back to its original transmission level. Regarding the thermal annealing kinetics, we observe a slower annealing rate at slower heating rates, with similar annealing profiles at similar heating rates. Furthermore, we note that in all annealing steps (c, f, i, m, p), annealing instantly starts when irradiation is stopped, despite the low temperature. However, at these temperatures, according to our experimental results from 3.2, thermal annealing should be negligible. One hypothesis that could reconcile these two visions is that the annealing at low temperatures is due to optical annealing by the probe laser, as we have seen in 3.3 that it could not be neglected even at 5 μW of power.

To further investigate the annealing kinetics recorded in this experiment, figure 4.4 presents the downsampled[5] RIA data as a function of time, and a smoothed calculated order 1 annealing rate constant[6] for the 5 annealing steps (c, f, i, m, p) overlapped, as a function of temperature[7]. Figure 4.5 presents the annealing rate for these 5 annealing steps as a function of the RIA level, image of the light-absorbing defect concentration, as well as a copy of the annealing rate interpolation from figure 3.11 for reference. First, we should note that the data above 470 dB/km is probably mainly numerical artifacts due to the lack of data points at the beginning (fast part) of the annealing and the data reduction. Regarding the optical annealing hypothesis previously mentioned, it is one order of magnitude lower than the annealing rates recorded here. Therefore, it needs further investigation to see whether and why its magnitude could be higher in this experiment compared to the experiment from 3.3 and if it could be due to the lower attenuation levels reached here, due to the shorter irradiation time. More experiments to better grasp optical annealing rates as a function of

---

[5]We linearly interpolate the time evolution of RIA on short time intervals and replace the data points by the interpolated RIA for the mean time in this interval. The data is reduced once by a factor of 9 for the fast warm-up experiments and twice for the slow warm-up experiments.

[6] $\frac{1}{RIA} \frac{\mathrm{d}RIA}{\mathrm{d}t}$

[7]The address of the repository containing these data analysis codes is given in appendix E.
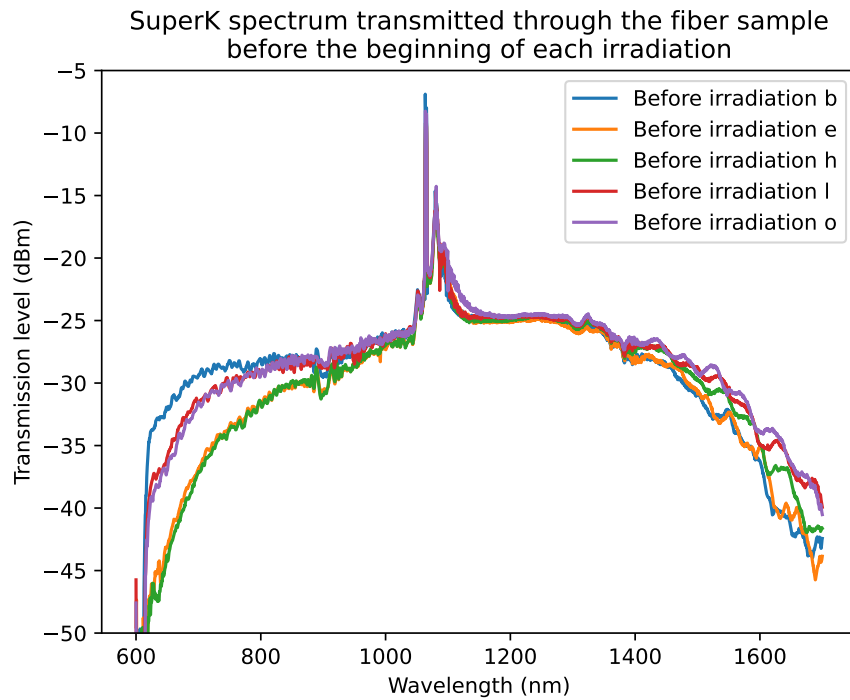
Figure 4.3: White light source spectrum transmitted through the fiber sample before the beginning of each irradiation step of this annealing experiment. It shows clearly at low wavelengths that the initial transmission of the fiber is never recovered during the thermal annealing steps, and that overnight warm-ups (before i and o) led to better recoveries.

power and RIA level are proposed in the next section.

Finally, from figure 4.5, profiles for the five curves seem to match, with an offset between slow and fast warm-up curves, which requires further investigation. The temperatures at similar RIA levels do not differ much, which makes it hard to separate the impact of defect concentration and temperature on the annealing rate. Below 210 dB/K, when temperatures reach the $120 - 130$ K temperature range, the annealing rate constant and the annealing rate drops. This can be linked to the self-trapped holes stability limit found around this temperature by Griscom [22], but the relation is not very clear, as we would expect annealing to be faster once the stability limit is reached. This could be due to the strong correlation in this experiment between temperature and RIA level. It is important to state here that the estimated maximum temperature offset between the fibers and the temperature measured by the sensor can reach an order of magnitude of 10 K, as shown in appendix C. This data is important as it replicates a warm-up scenario likely to be followed for heat treatment in practical systems: warming up magnets and fibers in a fixed thermostat. However, to fully understand the kinetics of these scenarios, better isolation of the different key parameters is needed, which leads us to propose future experiments in the section 4.4.

4.4 Conclusion and recommended future work

In this chapter, through white light absorption spectrum decomposition, we showed that self-trapped holes were probably the main defect responsible for attenuation at telecommunication wavelengths in our sample fibers under gamma irradiation. In the next chapter, we perform electron paramagnetic resonance spectroscopy to support this conclusion.

We performed experiments to study post-irradiation annealing kinetics, starting to explore the large parameter space of these phenomena. These experiments highlighted the need for an improved decorrelation of the experimental parameters. In particular, the next step for this experiment would be to decorrelate the temperature evolution from the RIA level and time by enabling isothermal annealing steps, rather than continuously increasing the temperature. This could be achieved by adapting the temperature control spool to adding feedback control with heaters and changing the cooling system. It is likely to yield better results to feed multiparameter modeling of annealing. Moreover, as seen in the previous chapter and confirmed here, optical annealing modeling also demands more investigation, especially as it seems unavoidable even in experiments designed to mostly probe thermal annealing, and its effect needs to be subtracted from the total annealing rate. To achieve this better understanding of optical annealing, more experiments similar to the ones presented in 3.3 can be performed, to probe annealing at fixed liquid nitrogen temperature. The power and dose reached can be changed, to better understand RIA at 1550 nm first. Then, other wavelengths can be studied, such as 785 nm, which is already included in the test setup. To study the power to optical annealing rate relation, one other possible experiment would be to decrease the power from 100% during irradiation until an RIA stability limit is found between radiation-induced defect creation and optical annealing.

To help separate these different effects and the underlying mechanisms at the point defect level, more experimental techniques can be leveraged, as presented in the next chapter.
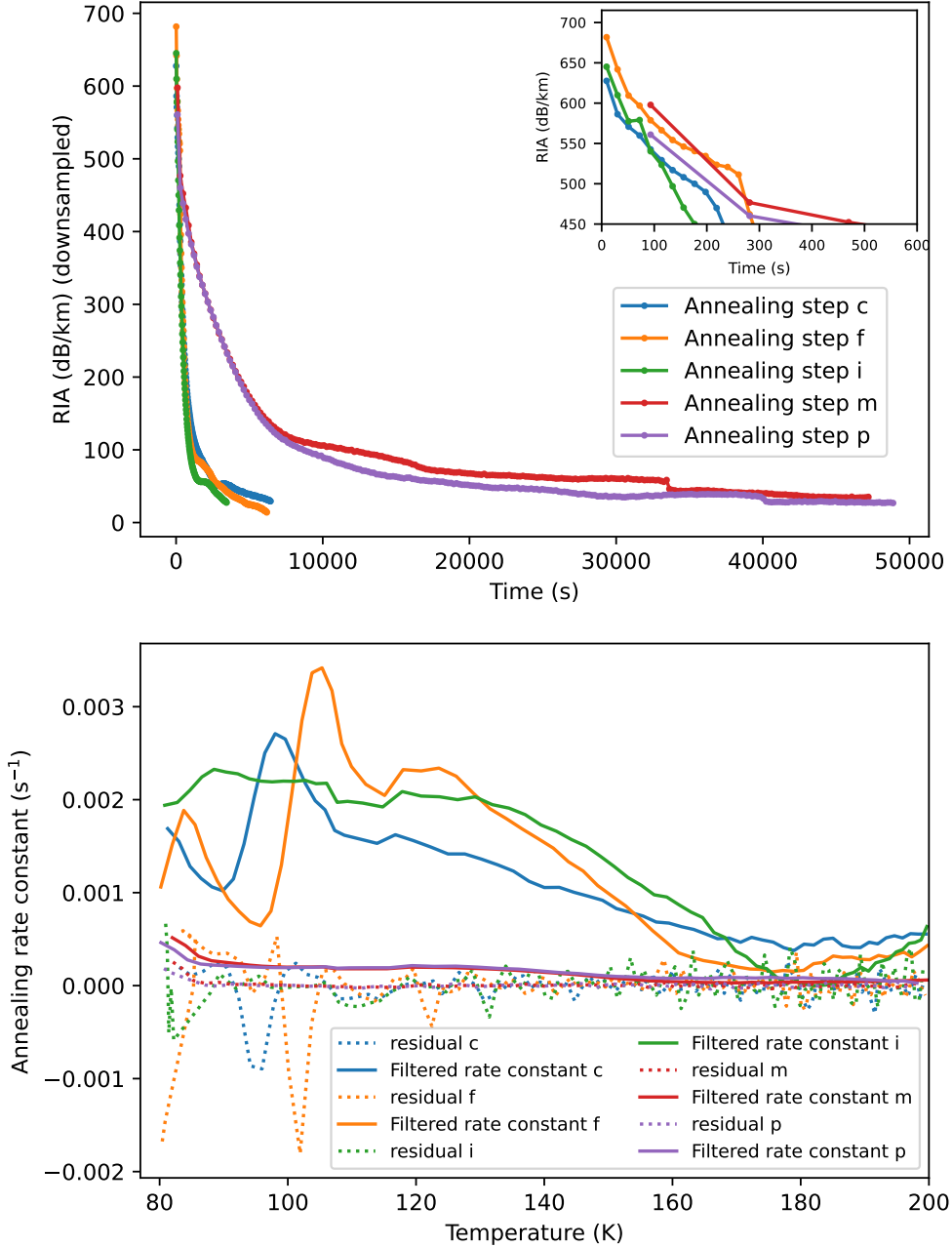
Figure 4.4: Results from the thermal annealing 5-step experiment. Top: calculated RIA level as a function of time, downsampled by local linear interpolation. Bottom: calculated annealing rate constant ($\frac{1}{RIA}\frac{\mathrm{d}RIA}{\mathrm{d}t}$, assuming a reaction of order 1, even if the data obtained does not necessarily point towards a specific reaction kinetics order) as a function of temperature as the sample is warmed up. RIA decreases as soon as the irradiation is stopped and until the end of the annealing step, with a gradually decreasing rate. The annealing rate constant seems to increase between 100 K and 130 K, which could be related to self-trapped holes' instability starting at these temperatures, but the data displayed here is not sufficient to firmly assert it. The separation of RIA level, temperature and optical annealing requires further studies.
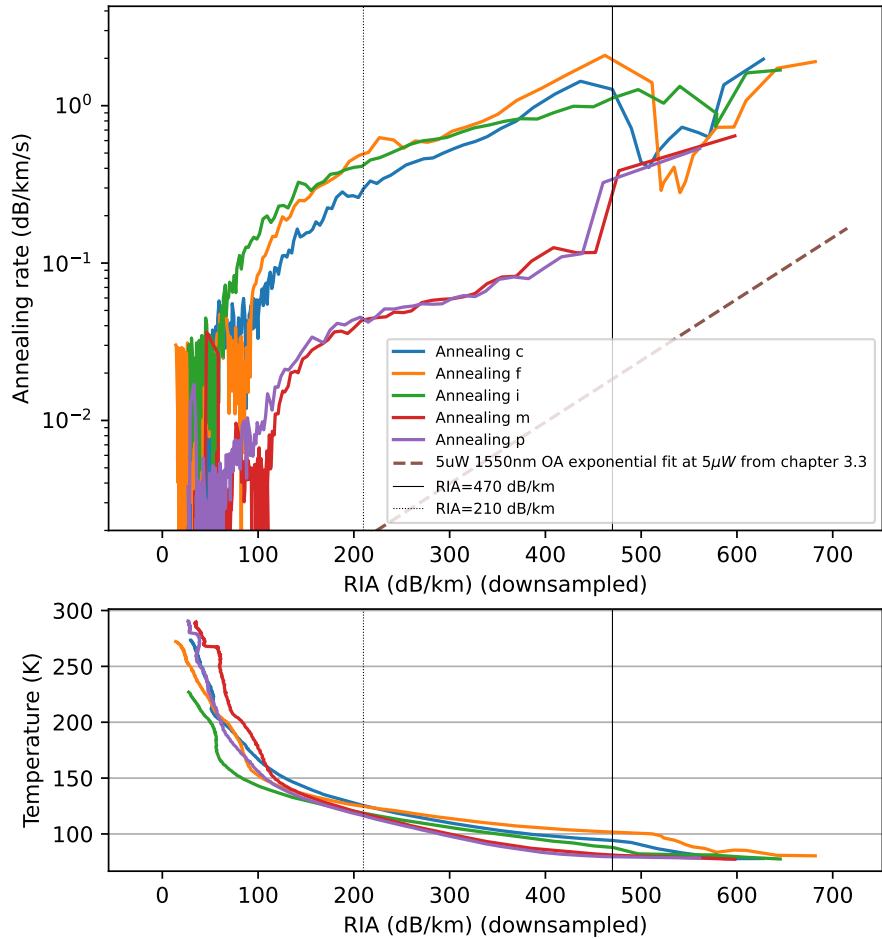
Figure 4.5: Annealing rate and temperature as a function of the RIA level during the thermal annealing 5-step experiment. In this figure, time flows from right to left. The data above 470 dB/km is probably mainly numerical artifacts due to the lack of data points at the beginning (fast part) of the annealing and the data reduction. Below this point and above 200 K, all annealing rates tend to follow an exponential decay (as a function of RIA), similarly to the optical annealing results from 3.3. Lower than 210 dB/km, after temperatures reach around $120-130$ K, we observe a sudden drop in the annealing rate, possibly linked to the self-trapped holes' stability limit, if they anneal quickly and the remaining defects are more stable, but this mostly demonstrates the need for more experiments with a better separation of the annealing parameters.

Chapter 5

Complementary methods for understanding RIA mechanisms

In this chapter, we cover two other experimental techniques that can complement absorption measurements to characterize the radiation-induced defects and better understand the kinetics of RIA.

In the first section, we present the use of electron paramagnetic resonance spectroscopy to identify the paramagnetic radiation-induced defects. We detail measurements performed on optical fiber preform fragments to validate the main conclusion of the RIA spectrum decomposition presented in chapter 4.

In the second section, we describe our first efforts to implement transient grating spectroscopy to glass samples at cryogenic temperatures, after irradiation, and with *in-situ* annealing. As this technique can non-destructively record thermal and acoustic properties of materials in real-time [67], it would complement other characterization techniques and better probe and model the annealing kinetics in optical fiber materials by relating changes in thermal and acoustic properties to radiation-induced defect populations.

5.1 Electron paramagnetic resonance spectroscopy (EPR)

5.1.1 Motivation and method

Electron paramagnetic resonance spectroscopy is a technique that relies on the Zeeman effect: under an external magnetic field H, the energy levels of a spin S are split into $2S + 1$ states. For a paramagnetic center with one single electron ($S = 1/2$), the magnetic field creates two states with $m_s \in \{-1/2, 1/2\}$ and with associated magnetic energy of $m_s g \mu_B H$, with m_s the spin quantum number, g the Lande factor, μ_B Bohr's magneton and H the intensity of the magnetic field. The transition of energy $\Delta E = g \mu_B H$ can be excited by an electromagnetic wave of frequency $\nu = \frac{\Delta E}{h}$ where h is Planck's constant. By sweeping continuously over different values of H, resonance can be found. The resonance peak in absorption of the electromagnetic wave gives information on the g factor and the interactions undergone by the probed spins. [68]

A simplified representation of an EPR spectrometer is given in figure 5.1.
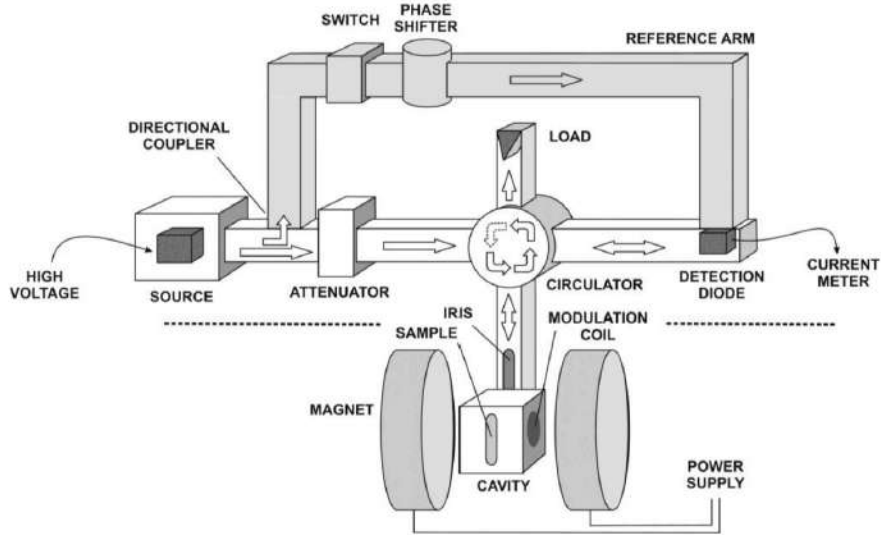
Figure 5.1: Simplified representation of an EPR spectrometer. [69]

In a molecular or crystalline environment and, most importantly, in silica glass, the EPR spectrum of the paramagnetic centers will depend on the orientation of the center relative to the magnetic field, and the g factor is replaced by a $\mathbf{g}$ matrix. This g matrix, which can also be calculated through density functional theory (DFT) simulations, can be diagonalized and is expressed in the eigenvector system as $\mathbf{g} = \text{diag}(g_1, g_2, g_3)$. The eigenvalues are more commonly called the "g values" and characterize the center. In glass, due to the amorphous structure, each center can be found in multiple orientations and the resulting spectrum is a superposition of the resonances at the g-value of each orientation. This results in spectral shapes called "powder patterns," such as the one shown in figure 5.2.
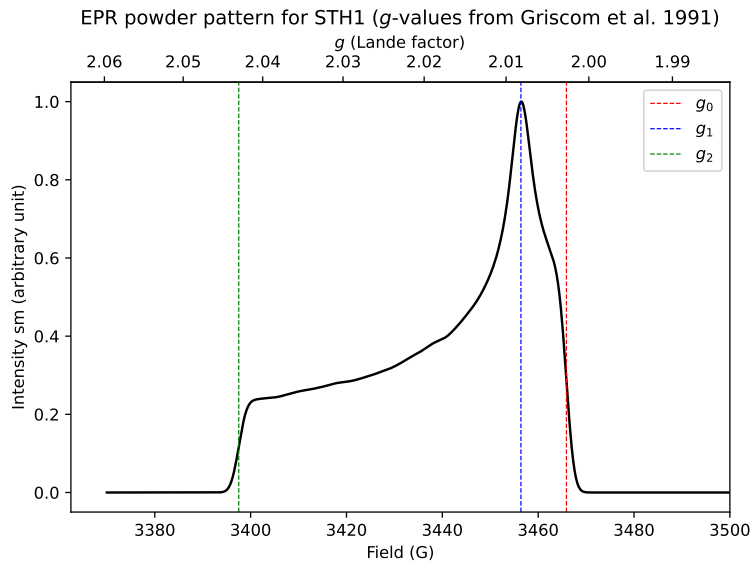
Figure 5.2: Simulated powder pattern EPR spectrum for self-trapped holes of type 1, with g values from [22]. Simulation microwave frequency: 9.714986 GHz.

It is confirmed in the literature that EPR can be used to identify paramagnetic defects in amorphous silica [15], [22], assisted by numerical simulations confirming the underlying structures [43], [55], [70]. The defects that can be found using this technique are the paramagnetic defects: E' centers, NBOHC, POR and STH. It is especially valuable given that STH, NBOHC and POR are among the most important contributors to absorption at low energies according to figure 1.6. For NBOHC, STH_1, STH_2, POR, E'_α, E'_β, E'_γ and E'_δ, we can find a list of the associated sets of g-values in studies led by Griscom et al. [22] and Lancry et al. [71] This last study is actually performed on bulk Heraeus F300 synthetic pure silica glass, which is the base material for the fibers studied here.[1] We use this past work to corroborate our own conclusions. After gamma irradiation, this study identified STH, POR and E'_γ contributions to the EPR spectrum of this bulk pure silica glass.

We perform an EPR experiment on the fiber material under study after gamma irradiation, while keeping the samples at cryogenic temperatures to avoid losing defects through thermal annealing and validate the results of our absorption spectrum decomposition from chapter 4. To achieve this, we place the samples in a small glass jar in a liquid nitrogen bath placed in the sample chamber of the Gammacell for irradiation to 30 kGy[2]. The entire bath is kept dark and transferred to the EPR facility. There, in the dark, the bottle is brought to the surface of the bath with tweezers, opened, and the samples are quickly transferred[3] to the EPR X-band pure silica tube, which is inserted in the EPR cavity cooled down to 40 K. We then probe the EPR spectrum at a microwave frequency of 9.714986 GHz (X-band EPR). Finally, we aim to decompose the resulting spectrum into known powder pattern contributions of paramagnetic point defects, to confirm their presence in the irradiated glass. We expect to find self-trapped holes from the decomposition performed in chapter 4 and from [71], and we might observe POR and E'_γ contributions [71].

The spectrometer used for this experiment is the Bruker EPR spectrometer managed by the Griffin group at MIT, and shown in figure 5.3.

5.1.2 Sample preparation

Multiple sample preparation methods were tested to achieve a high enough quantity of paramagnetic centers to obtain a significant EPR spectrum and to make the fast transfer of the sample from the liquid nitrogen bath to the EPR cavity as easy as possible. When simply stripping 10 cm long fiber samples of their polyimide coating with 200°C concentrated sulfuric acid [72], getting enough fibers down the EPR tube in a short amount of time did not yield good results. The technique that achieved the best performance was cutting fragments of the fiber preform. This glass cylinder with the same properties as the fiber is normally drawn homothetically in an oven into fibers. Before probing the irradiated EPR spectrum

---

[1]"These fibers (Exail IXF-RAD-SM-1550-014-PI) present ultra-low impurity levels with some residual chlorine and some hydroxyl content. The cladding typically presents a 0.5 weight % fluorine content, while the core is pure silica, with some fluorine that comes from migration during the collapse, around 0.1 weight %." (Information provided by the manufacturer)

[2]Here, the value is given based on the calibrated central dose rate in air, as the setup differs slightly from the white light spectroscopy configuration described in 2.5. The same dewar is used, but the sample bottle is in the middle of the bath and not surrounded by a metallic spool.

[3]The sample spends on the order of 1 s in ambient air.

Figure 5.3: EPR spectrometer managed by the Griffin group at MIT (Francis Bitter Magnet Laboratory) and used for this experiment.

of these samples, we confirmed that they did not have any pre-irradiation EPR signature. Figure 5.4 shows the samples before irradiation.

Figure 5.4: EPR samples : fragments of Exail IXF-RAD-SM-1550-014-PI fiber preform in a glass jar.

5.1.3 Results and discussion

The spectrum obtained with this procedure is presented in figure 5.5. The spectrum intensity was normalized and the data was smoothed using a moving mean filter with a window of size 5. We identify two main peaks in this spectrum. The right peak presents a very low g-anisotropy which we can relate to E'_γ centers, already found by Lancry et al. in Heraeus F300 pure silica glass [71]. This helps us identify a slight magnetic field offset (which needs to be calibrated regularly) of 3 G and the displayed spectrum incorporates this recalibration of the magnetic field. The main peak presents higher G anisotropy and can be associated with STH of types 1 and 2. The fit parameters are the following:

- g values (from Griscom et al. [22]): $[2.0027, 2.0082, 2.043]$ for STH_1, $[2.0054, 2.0078, 2.013]$ for STH_2, and $[2.0018, 2.0006, 2.0003]$ for E'_γ. (The microwave frequency is 9.714986 GHz)

- Intensities: 0.14 for STH_1, 0.85 for STH_2, and 0.34 for E'_γ.

- Standard deviation (σ) for isotropic Gaussian broadening: 1.3 G for STH_1, 2 G for STH_2, and 1.5 G for E'_γ.

This validates the decomposition from the previous chapter, which identified self-trapped holes as the main contributor in the gamma irradiated samples studied in this work. The composite 1-eV band used in the RIA spectrum decomposition had been tentatively associated with self-trapped holes [30], which tends to be confirmed by this EPR study[4]. E'_γ gamma centers absorbing mostly ultraviolet light, they were not significant in our white-light spectrum decomposition that focused on the infrared spectrum. POR, identified by Lancry et al. [71], may be present here as a low contribution (they have a high g anisotropy, similar to STH_1), but it is difficult to say as they did not appear in our white light decomposition and their g-values overlap with those of self-trapped holes.

---

[4]We mostly see two types of paramagnetic defects in the EPR spectrum obtained: E'_γ and STH. In the white light absorption spectrum decomposition, the main bands with a significant effect in the probed $[1000, 1700]$ nm range were STH bands and the composite 1-eV band. We know that E' centers absorption bands are in the UV range, at photon energies closer to 6 eV (see 1.6). Then, it is very likely that the 1-eV band is linked to the lower energy defects that STH are. However, it could be linked to diamagnetic centers (not E' centers, NBOHC, POR or STH), which are not be probed by EPR. Nevertheless, none of the other absorption bands from figure 1.6 above 600 nm are associated with diamagnetic defects (the LTIRA band is also believed to be linked to self-trapped holes[31]), which makes it unlikely.
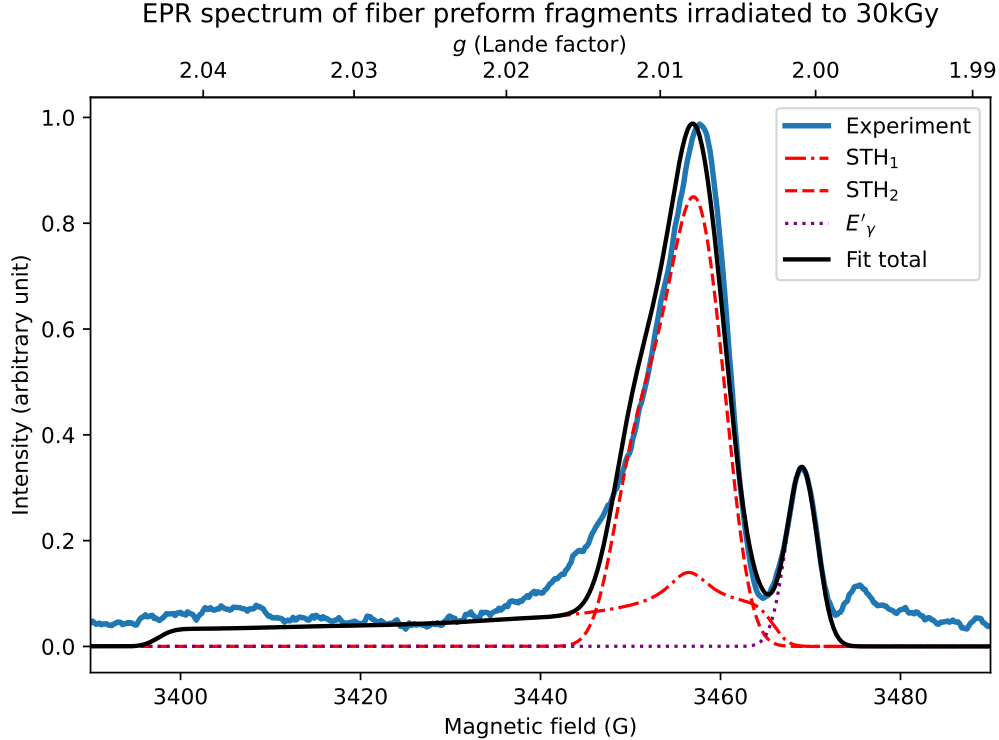
Figure 5.5: EPR results : spectrum of preform fragments after 30 kGy gamma irradiation at 77 K, probed at a frequency of 9.714986 GHz, and decomposition into STH_1, STH_2, E'_γ powder pattern contributions. We observe that the spectrum is dominated by self-trapped holes, which confirms the results of the decomposition performed in chapter 4 and tends to confirm the association of the composite 1-eV band with self-trapped holes. The presence of an E'_γ, easily identified by its low g-anisotropy and its presence in the spectrum from [71], indicates that other absorption bands exist in the UV part of the absorption spectrum (see figure 1.6) and serves as a good calibration element for the magnetic field measurement. The magnetic field offset is here calibrated based on this E'_γ peak. The relative intensities of the powder patterns of the fit are 0.85 for STH_2, 0.14 for STH_1, and 0.34 for E'_γ. The standard deviation for the Gaussian broadening of the powder patterns used in the fit are 2 G for STH_2, 1.3 G for STH_1, and 1.5 G for E'_γ. The g values are taken from [22]

5.2 Transient grating spectroscopy (TGS)

5.2.1 Description of the technique and motivation

Transient grating spectroscopy (TGS) enables the measurement of both thermal diffusivity and the speed of sound in a bulk material sample. Thus, TGS could allow one to probe the evolution of these quantities in optical fiber glass samples at different dose levels, thermal annealing profiles and exposures to photobleaching light sources. Suppose irradiation defects have a significant impact on one of these two quantities in silica, as is the case for other materials (for example, see [73], [74]). In that case, the evolution of the decay signals will give us information on changes in the populations of these defects.

As detailed in [67], TGS works by generating surface acoustic waves (SAWs) and a well-defined temperature grating. They are created by overlapping two short excitation laser beams (532 nm) with a fixed angle θ, generating an periodic intensity interference pattern. Absorption of the light generates a spatially periodic temperature grating, which results in a periodic variation of the specimen surface height due to thermal expansion. In addition, rapid thermal expansion launches two monochromatic, counterpropagating SAWs. The decay of the SAWs and temperature grating is then measured by the diffraction of a probe laser on the sample surface, which is compared to a reference beam reflected from the sample surface. The SAW frequency and the decay measured can then be directly related to the speed of sound and the thermal diffusivity respectively.

Figure 5.6 shows the TGS apparatus adapted for this study and described in [75]. Samples need to be kept in the dark, except for optical annealing testing, and cold during irradiation and spectroscopy measurement to avoid any unwanted annealing. To that end, a fixture in which the glass samples can be immersed in liquid nitrogen, irradiated, probed with TGS, and subjected to optical annealing has been designed to replace the vacuum chamber. It is described in the following section.
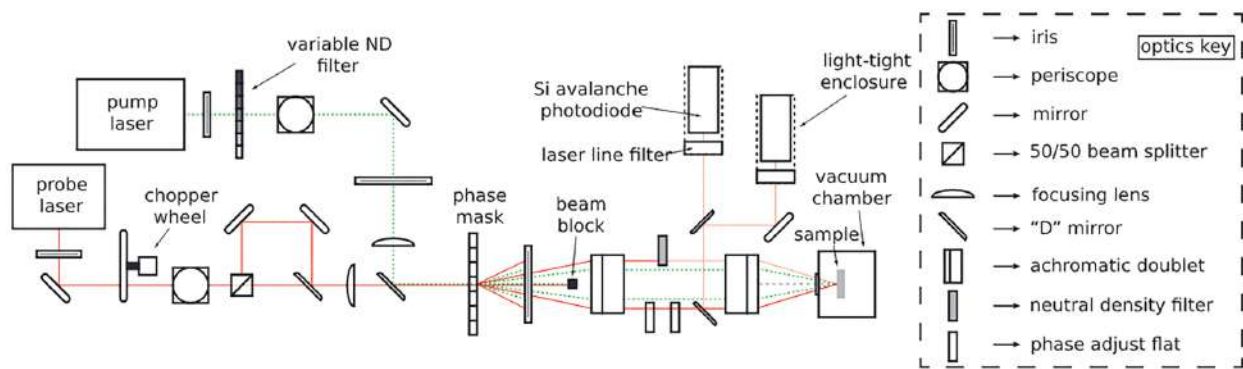
Figure 5.6: Description of the dual-heterodyne TGS apparatus. Reproduced from [75]. The vacuum chamber is here replaced by a liquid nitrogen chamber.

5.2.2 Design of a cryogenic fixture for TGS

In order to keep the sample at 77 K from irradiation to TGS measurement, it was decided to design a dewar to keep it immersed in liquid nitrogen at all times. To obtain a sample with a large enough polished surface, the sample chosen for this experiment are coins made from the optical fiber preform, as detailed in 5.2.3. The different requirements for this cryogenic fixture were:

- To hold liquid nitrogen, the inside of the container needed to be insulated from the outside. A double wall vacuum insulation and a lid with spaces left for cables were chosen.

- The sample needs to be at the right distance from the achromatic doublet, precisely at the focal point. It required the sample coin to be close to the window.

- Furthermore, the angled laser needed to go through the windows of the dewar, requiring these windows to be large enough. These windows also needed to be resistant to radiation-induced darkening. Sapphire is among the standard window materials for cryogen applications[76], and widely used for space applications, and some studies demonstrated the low impact of RIA in sapphire [77], which is why sapphire viewports were chosen. However, as no previous study on RIA in sapphire at liquid nitrogen temperature was found, initial RIA testing of the viewports at 77 K is planned to validate this choice.

- The dewar needs to fit on optical rotation stages for proper alignment of the sample.

- The whole fixture needs to fit in the Gammacell cylindrical chamber (see 2.4).

- For simplicity, the sample holder must be adaptable to different coin diameters.

- The design must enable *in situ* optical annealing. It is achieved by attaching a collimator to the sample holder, facing the back of the sample coin, and connected outside of the dewar to a 100 mW fiber-pigtailed laser at the optical annealing wavelength (see chapter 2).

A preliminary representation of the TGS setup can be found in figure 5.7.

The final dewar, base and sample holder design are represented in figure 5.8, 5.9 and 5.10. Part 2 of the sample holder can be changed to accommodate for different coin sizes.
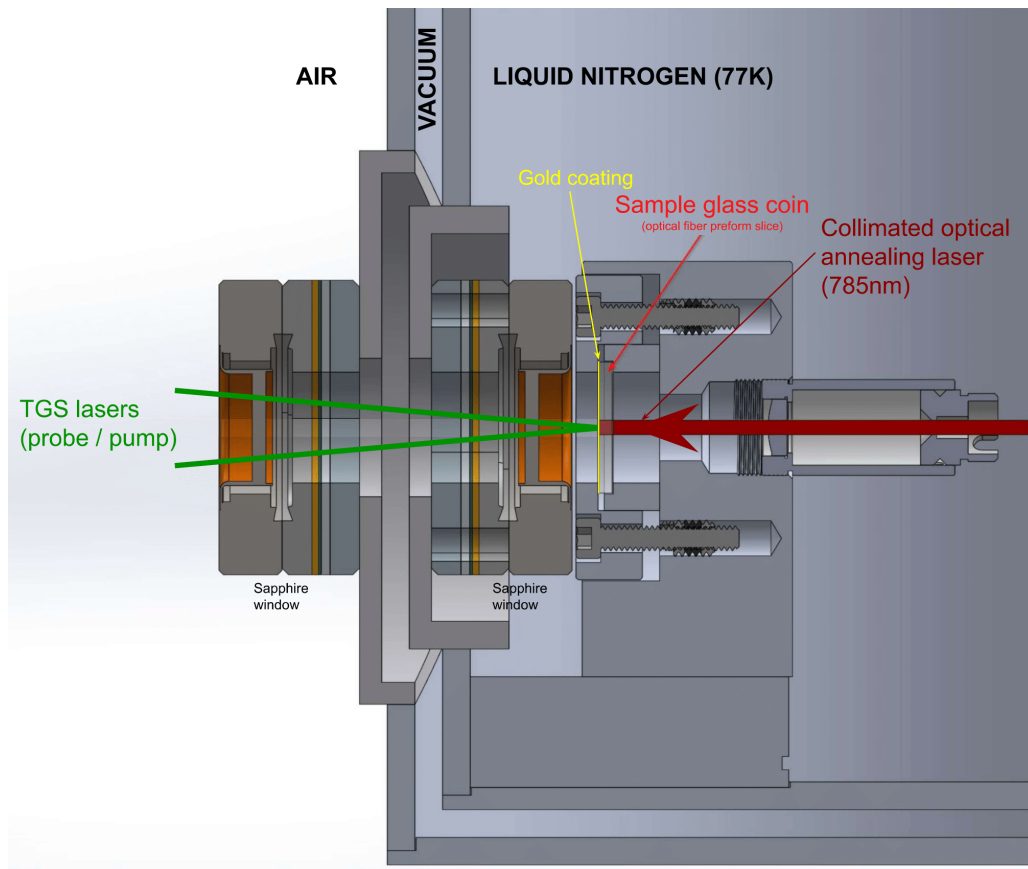
Figure 5.7: Preliminary representation of the transient grating spectroscopy (TGS) setup that will be used for irradiated fiber preform coins
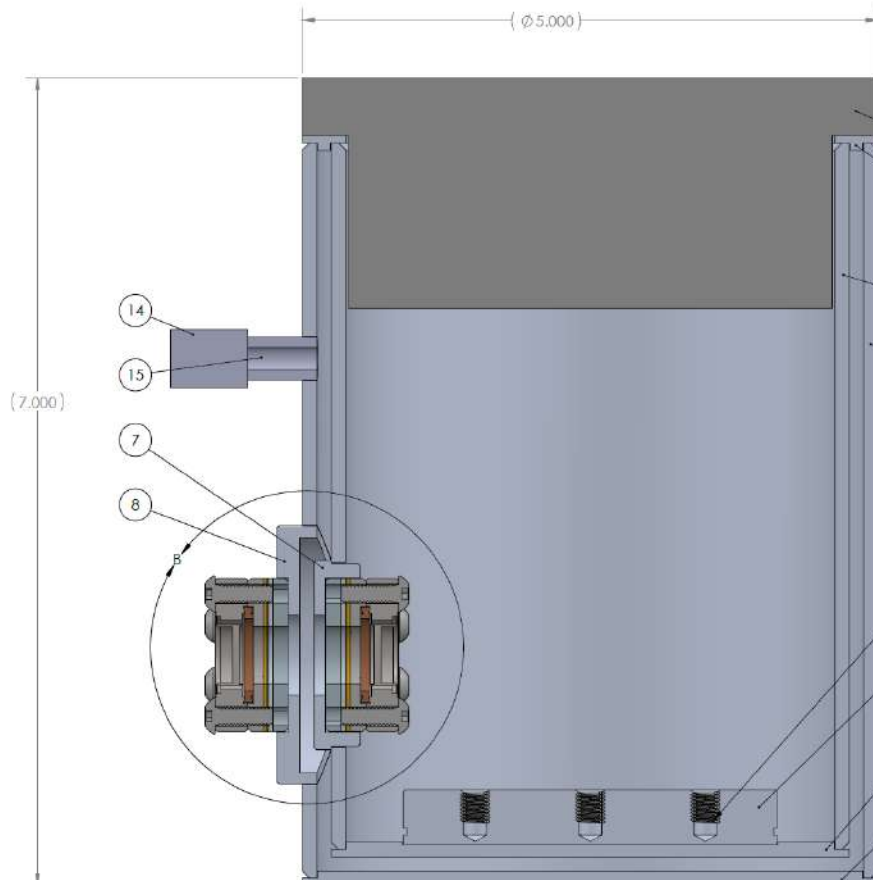
Figure 5.8: CAD representation of the TGS Dewar
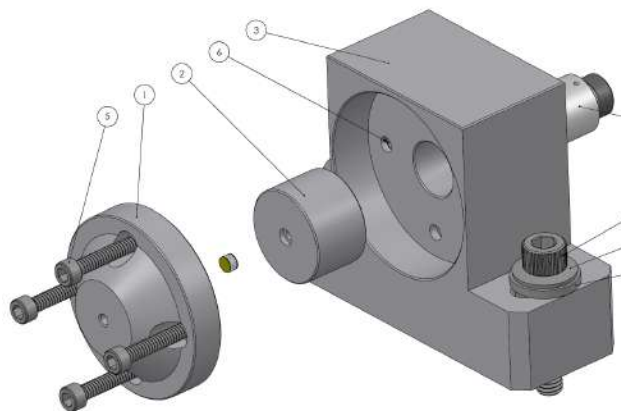
Figure 5.9: CAD representation of the TGS sample coin holder that will be installed inside the Dewar (figure 5.8)

5.2.3 Method

Sample preparation

Before the drawing process, optical fibers are in the form of a large preform cylinder (20 mm diameter, 500 mm long) with the same propertie as the fibers. In order to perform TGS on a large enough sample, sample coins were made out of this preform material provided by Exail. The following procedure is the one that was found to be the most likely to obtain well-polished samples of standard size without shattering them. The preform was mounted in epoxy for cutting, cut with a Buehler Isomet low speed saw into multiple smaller sections for epoxy mounting, and $\approx$ 1 mm-thick slices were cut with a low speed saw using a 15LC blade. These preform sections were mounted on a plate with wax, and 3 mm diameter discs were cut out from the center of these coins using a Fischione 170 ultrasonic disc cutter with silicone carbide abrasive powder. The resulting samples were cleaned by sonication in acetone. To polish these coins, hand polishing them one at a time was necessary. They were mounted with wax on metal cylinders and polished with a Dace Technologies NANO-1000S and FEMTO-1500S polisher following these steps (inspired from the recommended Buehler methods[78]):

- Polishing on an Apex DGD 15 μm surface at low speed until uniformity of the scratches is reached (checked under a microscope).

- Polishing on an Apex DGD 3 μm surface at low speed until uniformity of the scratches is reached (checked under a microscope).

- Finishing with MiroMet Polish on a MasterTex surface at low speed for a few minutes, until satisfactory surface polish is reached.

The sample is then water-cleaned, unmounted, and sonicated in acetone.

Gold coating

The polished glass coins cannot be directly used for the experiment. The TGS probe and pump lasers must not be able to go through the transparent coin, or they would probably lead to unwanted optical annealing during the measurement. To increase the reflectivity of the sample and prevent the TGS lasers from annealing out radiation-induced defects, a thin gold coating is deposited on the surface of the samples with a sputter coater. To determine the coating time necessary to attenuate the lasers enough, as shown in figure 5.11, we sputter coated a plano-concave lens on its planar side with gold for an increasing amount of time, and measured the transmission level evolution on the TGS setup by putting a photodiode sensor on the concave side of the lens, connected to a Thorlabs PM100D power meter. Figure 5.12 shows the results of this test.

This test confirms an exponential attenuation as gold thickness linearly increases with coating time, and we can use it in conjunction with optical annealing results similar to the ones from 3.3 to determine the appropriate coating time to mitigate the effects of optical annealing on the TGS results. The total coating thickness at the end of this experiment (19 minutes and 16 seconds of sputter coating time) was measured by adding a carbon layer on

top of the gold, cutting a cross section with a focused ion beam (FIB) and capturing it with a scanning electron microscope (Helios NanoLab 660) (see figure 5.13). Figure 5.14 shows the images obtained with the frontier between the silica surface and the gold layer and the frontier between the gold and carbon layers. The average thickness is between 45 and 48 nm. With this gold coating, we successfully recorded surface acoustic waves with the TGS system in the laboratory, confirming this technique's applicability to glass samples.

5.2.4   Recommended future work

When the TGS cryogenic fixture is delivered, we recommend taking a baseline TGS spectrum of a fiber glass sample and comparing it with the irradiated spectrum. Changes in SAW frequency or diffusivity could be correlated with the radiation-induced defects identified by other techniques. Then, we recommend optically annealing the sample and regularly probing its TGS spectrum. Its evolution can be compared with the results from 3.3 on optical annealing to further associate changes in the TGS spectrum with the known evolution of RIA. Finally, the TGS spectrum after annealing should be compared with the initial spectrum, to see what changes in the TGS spectrum can be related to the defects that cannot be optically annealed. This will indicate whether TGS can serve as a good complementary method to witness the evolution of diamagnetic color centers (not probed by EPR) or defects absorbing at low wavelengths (not probed by white light absorption spectroscopy).

   In situ warm-up kinetics can also be probed in future TGS experiments to better grasp the mechanisms and kinetics of defect annealing. Despite the "elusive role of electron-phonon interaction in phonon heat transport," TGS is a technique that can experimentally measure its impact on thermal conductivity [79]. This leads us to think that even electronic defects induced by irradiation in silica glass could slow down thermal transport to a level measurable by TGS. Other radiation-induced defects, such as network coordination defects, could also contribute to the evolution of heat transport that will be measured by TGS, but it is still uncertain what this impact and its magnitude will be.
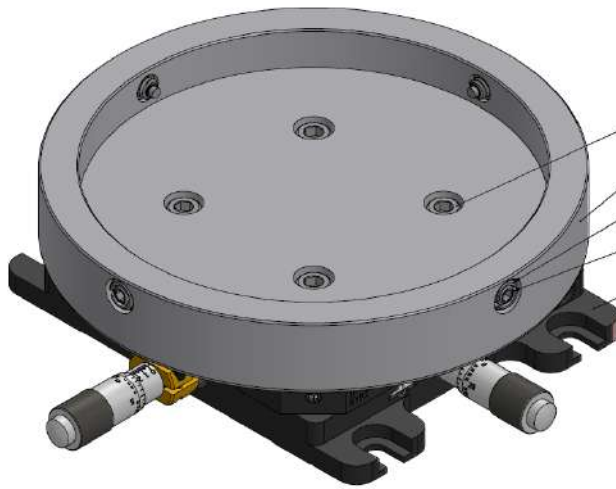
Figure 5.10: CAD representation of the TGS dewar base for attachment to an optical breadboard stage
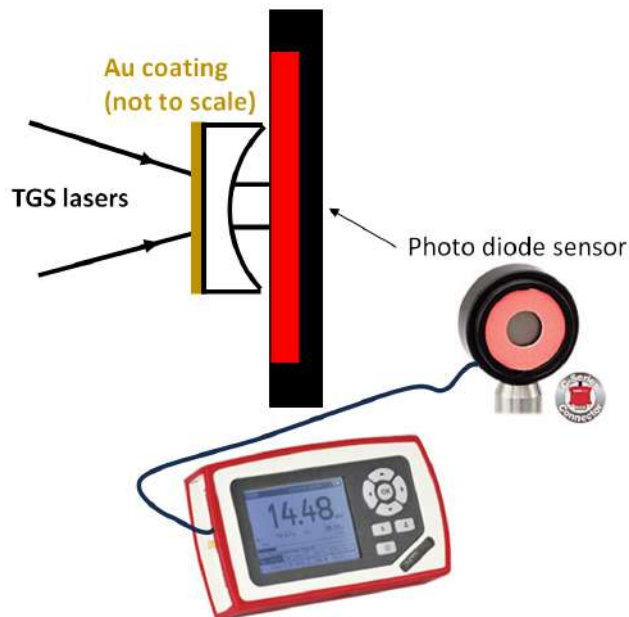
Figure 5.11: Gold coating transmission test diagram
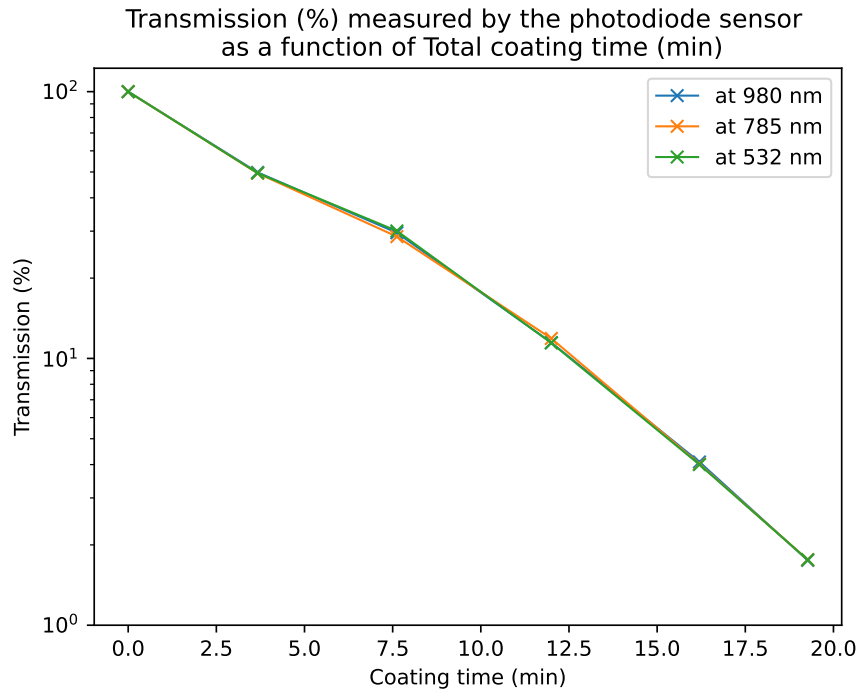
Figure 5.12: Transmission (%) measured by the photodiode sensor (Thorlabs S12xC connected to PM100D) as a function of total coating time (min) at three different wavelengths (980 nm, 785 nm, 532 nm)
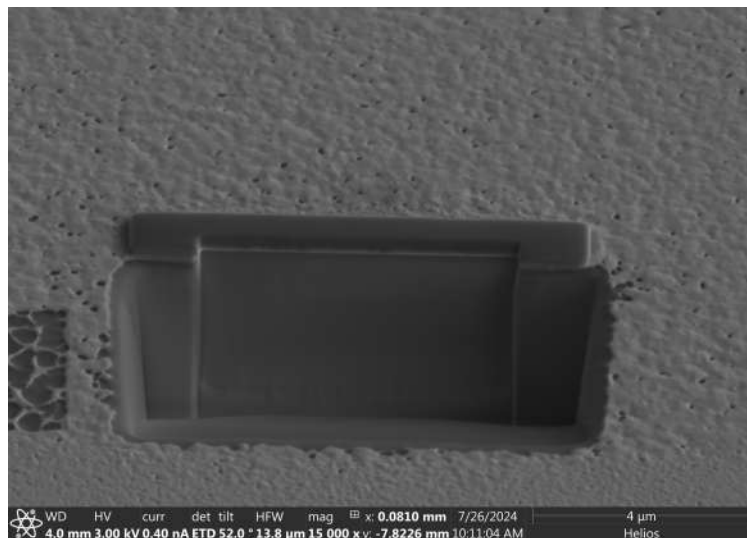
Figure 5.13: Scanning electron microscope image of the gold coating on the planar surface of the lens and the carbon layer deposited on it. A trench has been created with a focused ion beam to observe the cross-section and measure the gold coating average thickness.
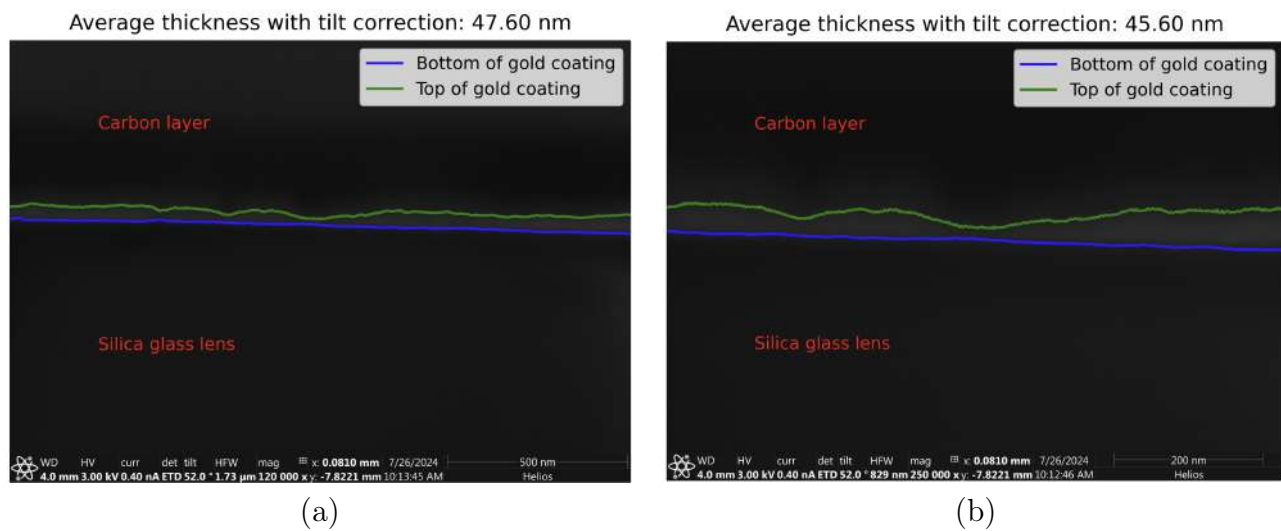
Figure 5.14: Scanning electron microscope (SEM) image of the gold coating on the planar surface of the lens and the carbon layer deposited on it. The frontiers between the three layers, found by setting an intensity threshold at 55% of the maximum intensity in the image, are represented in green and blue. A projection is used to account for the 52° tilt angle at which the cross-section is observed in the thickness calculation. (a) The average thickness measured on this first image is 47.60 nm. (b) The average thickness measured on this second image with a higher magnification is 45.60 nm.

Chapter 6

Conclusion and future work

In this work, we have answered multiple key questions regarding the mechanisms and kinetics of radiation-induced attenuation. After designing an experimental setup to be able to perform white light absorption spectroscopy during irradiation, we performed an experiment to artificially reconstruct the thermal annealing kinetics of RIA in fibers kept at 77 K and in the dark. This experiment proved that thermal annealing processes were essentially frozen at 77 K, validating the equivalence between RIA experiments performed at 77 K and applications at 20 K. This result will be the object of further investigation with comparisons to 20 K experiments, and the duration of the experiment performed in 3 could be extended for increased certainty. By decomposing the radiation-induced absorption spectrum and probing the electron paramagnetic resonance of irradiated optical fiber samples, we also established that self-trapped holes were the main contributors to RIA for the pure silica core under study, at liquid nitrogen temperature and under gamma irradiation. As their instability above 130 K is known [22], this information is crucial for an operator designing a heat treatment outage. With EPR, we confirmed the presence of the UV-absorbing E'_γ centers in these fibers, found by Lancry et al. [71] in bulk samples of similar glass. We highlighted the destructive impact of optical annealing, limiting absorption spectroscopy measurements. Furthermore, we were able to prove the applicability of post-irradiation transient grating spectroscopy to optical fiber glass samples, and designed a fixture and a working procedure to operate this technique on glass at cryogenic temperatures. In the exploration of thermo-optical annealing processes, we conducted experiments to improve our understanding of thermal annealing kinetics and proposed first hypotheses to account for the effects of defect concentration, temperature and heating rate.

Much remains to be explored. In order to achieve full predictive modeling or radiation-induced attenuation and thermo-optical annealing, even limited to one kind of optical fiber, many questions need to be answered. Regarding thermal annealing, more experiments are required to fully separate the effects of defect concentration, warm-up rate and temperature. In particular, we propose isothermal annealing experiments to achieve this separation. For optical annealing, the key variables (wavelength, power, and fiber length related to attenuation level) have started to be explored, but these efforts need to be furthered to develop strong predictive models. This can be done with the experimental setup built during this project. While the applicability of transient grating spectroscopy to glass has been proven, future experiments should confirm whether it can bring new information about the popula-

tions of defects present in irradiated glass and how destructive it can be on easily annealed radiation-induced defects.

For companies like Commonwealth Fusion Systems, which aim to operate optical fiber systems under irradiation at cryogenic temperatures for extended times; this data can be used to optimize the operation and outage planning for such systems. Knowing that RIA for this application is mostly governed by self-trapped holes and that these defects are unstable above 130 K, [22] can strongly help limit the duration of these outages or the temperature at which they are performed, which are two parameters that can represent cost or system constraints. Having a model able to predict directly the evolution of RIA during annealing and subsequent irradiation is key. Additionally, understanding optical annealing supports the prevention of magnet downtimes and the knowledge of its limitations. Furthermore, proving that experiments can be performed at liquid nitrogen temperature can also facilitate and accelerate the development of these RIA kinetics models.

In this work, we successfully designed and ran experiments that provide solid foundations for the comprehension of thermo-optical annealing mechanisms and kinetics of RIA in optical fibers at cryogenic temperatures.

Appendix A

Optical spectrum analyzer settings and program

The following program is used to loop over the sweeping of the spectrum by the Yokogawa AQ6370D OSA and saving every spectrum to an external storage device. It automatically sets the analyzer settings to keep them consistent throughout the experiments. This program leads to a sweep period of 2.261 s, except when the OSA performs its automatic zeroing operation between two sweeps, and a duration of 1.813 s). These values were obtained by recording the sweep trigger output signal with the Arduino TTL box presented in 3.2.4. Should we wish to increase the sweep period, the duration parameter in line 22 can be increased.

```
1  INIT
2  ' We define the settings of the OSA and the output format
3  N = 100000
4  TRIGGER OUTPUT SWEEP STATUS
5  SMOOTHING ON
6  FIBER CONNECTOR ANGLED
7  AUTO FILE NAME DATE
8  REFERENCE LEVEL -10.0dBm
9  LEVEL SCALE 10.0dB/D
10 RESOLUTION WL 2.000nm
11 SENS MID
12 AVERAGE TIMES   1
13 SAMPLING POINT AUTO ON
14 SAMPLING INTERVAL  0.400nm
15 SWEEP SPEED 2×
16 TRACE WRITE:CSV
17
18
19 ' We loop over sweeping and writing the spectrum in the external storage
20 SINGLE
21 WRITE TRACE A EXT
22 WAIT 0s  ' This wait time can be increased to lower the sweep frequency
23 N = N-1 ; IF N<>0 GOTO 20
24
25 END
```

Appendix B

Temperature monitoring program for Cernox sensor

The following Jupyter notebook was used to monitor interactively the temperature measured by the Cernox sensor, by interrogating the Lake Shore Cryotronics model 211 temperature controller through its serial output.

```
In [2]:  %matplotlib inline
         %matplotlib widget
         import serial
         from serial.tools import list_ports
```

```
In [3]:  serial.PARITY_NONE
```

```
Out[3]:  'N'
```

```
In [4]:  for port in list_ports.comports():
             print(port)
```

```
COM4 - Prolific PL2303GT USB Serial COM Port (COM4)
COM3 - Silicon Labs CP210x USB to UART Bridge (COM3)
COM5 - USB Serial Port (COM5)
```

```
In [5]:  PORT="COM4"

         ser = serial.Serial(port=PORT, baudrate=9600, bytesize=serial.SEVENBITS,
                             parity=serial.PARITY_ODD, stopbits=serial.STOPBITS_ONE, timeout=1)

         for i in range(3):
             print(ser.write(bytes('KRDG?\r\n','utf-8')))
             print(float(ser.readline().decode('utf-8')))

         ser.close()
```

```
7
304.85
7
304.85
7
304.85
```

```
In [6]:  import matplotlib.pyplot as plt
         import numpy as np

         from IPython.display import display, clear_output, Javascript
         import ipywidgets as widgets
         import threading
         import time
         import csv

         global ser
         ser = serial.Serial(port='COM4', baudrate=9600, bytesize=serial.SEVENBITS,
                             parity=serial.PARITY_ODD, stopbits=serial.STOPBITS_ONE, timeout=1)
         global i
         i=0

         def out_print(message):
             global out, outlines
             out.outputs=()
             outlines=outlines[1:]+[f"{message}\n"]
             for o in outlines:
                 out.append_stdout(o)

         # Function to generate random numbers and update the plot
         def update_plot():
             global running
             global i
             global fig, ax
             while running:
                 data.append(getDataPoint())
                 times.append(round(time.time()-starttime,3))
                 out_print(f"{times[-1]} s, {data[-1]} K")
                 ax.clear()  # Clear the previous plot
                 ax.set_xlabel('Time (s)')
                 ax.set_ylabel('Temperature [K]')
                 ax.set_title('Temperature in fiber spool')
                 ax.grid(True)
                 ax.plot(times, data, marker='o', label=f"last temp : {data[-1]}K")
                 ax.legend()
                 fig.canvas.draw()
                 plt.pause(1)  # Pause for 1 second
```

```python
        ser.close()
        plt.close()

def getDataPoint():
    ser.write(bytes('KRDG?\r\n','utf-8'))
    r = float(ser.readline().decode('utf-8'))
    return r

# Start button click event
def on_start_button_click(b):
    global running, times, data
    times = []
    data = []
    if not(ser.is_open):
        ser.open()
    global starttime
    global startdate
    startdate=time.strftime("%Y-%m-%d %a %Hh%Mmin%Ss",time.localtime())
    out_print(f"START: {startdate}")
    starttime=time.time()
    running = True
    thread = threading.Thread(target=update_plot)
    thread.start()

# Stop button click event
def on_stop_button_click(b):
    on_save_button_click("")
    global running
    running = False
    out_print("STOP")

def on_save_button_click(b):
    filename=startdate+f" - fiber T curve - dur {int(times[-1]-times[0])}s"
    with open(filename+".csv",'w') as f:
        writer=csv.writer(f)
        writer.writerows(zip(times,data))
    plt.savefig(filename+".png")
    out_print("data saved in "+filename)
    return

# Create start and stop buttons
start_button = widgets.Button(description='Start')
start_button.on_click(on_start_button_click)

stop_button = widgets.Button(description='Stop & Save')
stop_button.on_click(on_stop_button_click)

save_button = widgets.Button(description='Save')
save_button.on_click(on_save_button_click)

global out, outlines
out = widgets.Output(layout={'border': '1px solid black'})
outlines=5*["\n"]
for o in outlines:
    out.append_stdout(o)

# Display the buttons
display(widgets.HBox([start_button, stop_button, save_button]))

# Initialize the plot
times = []
data = []

global fig, ax
fig, ax = plt.subplots(figsize=(9, 5))
ax.set_xlabel('Time (s)')
ax.set_ylabel('Temperature [K]')
ax.set_title('Temperature in fiber spool')
ax.grid(True)

display(out)

# Global variable to control the running state of the plot
running = False
```

```
HBox(children=(Button(description='Start', style=ButtonStyle()), Button(description='Stop & Save', style=
Butto…
Output(layout=Layout(border_bottom='1px solid black', border_left='1px solid black', border_right='1px so
lid b…
```

Figure

Temperature in fiber spool

Temperature [K]

Time (s)
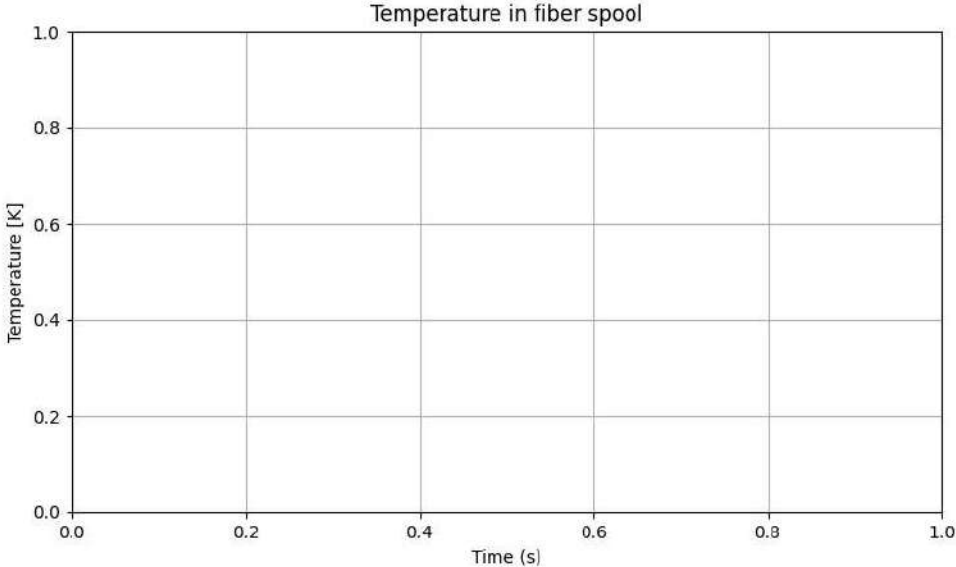
Appendix C

Difference between temperature measured by the spool sensor and actual fiber temperature

As presented in 2.3, the temperature sensor is embedded in the metallic spool next to the inner wall of the cavity containing the fiber spool. Therefore, during thermal transients, the temperature measurement we obtain may differ from the actual temperature of the fiber sample in the cavity. I plan to measure this difference by placing a temperature sensor in the cavity to measure the temperature difference but, to obtain a first estimate of the order of magnitude of the temperature difference, I decided to perform a heat transfer simulation of the spool warming up from liquid nitrogen temperature to room temperature.

This simulation was performed using COMSOL Multiphysics® with the heat transfer physics package. [80] The geometry was simplified to a 2D axially symmetric configuration, presented on figure C.1. The blue dot represents the position of the temperature sensor in the real geometry, while the grey rectangle is the sample cavity. This figure also presents the materials and boundary condition assumptions. Some parameters of the boundary conditions, stated in the figure, were manually tuned to approach the warm-up profile measured in step c of the thermal annealing experiment presented in chapter 4. This simulation output times ranged from 0 to 6620 s in steps of 10 s, while the tolerance and mesh were set to "Physics controlled". To simplify the comparison with the experimental data, we start with an initial temperature of 78.026 K, which is higher by about 1 K than the actual equilibrium temperature in liquid nitrogen.

From this simulation, we extract three temperatures as a function of time:

- the temperature at the point corresponding to the middle of the sensor, represented in blue in the figure,

- the average temperature at the inner cavity vertical wall next to it,

- and the maximum temperature in the air cavity.

The results of this simulation are presented in figure C.2. With the tuning of the boundary condition parameters (air temperature inside the sample chamber and characteristic height

of the vertical wall), we obtain a warm-up profile similar to the experimental sensor data. It confirms that the cavity temperature increases faster than the sensor position temperature, which is close the cavity inner wall temperature. This is due to the outer radial position of the sample cavity (closer to the heat source) and the low conduction air layer slowing down the temperature increase in the central part of the spool.

The maximum difference between the cavity temperature and the sensor position temperature in the simulation is reached early in the transient (220 s) and is equal to 8.11 K. As this is only an estimation, the reader should remember that the difference between the fiber samples and the sensor in our experiments can be on the order of 10K.

At $t = 0s, T = 78.026K$ (first data point from experimental data used for comparison)
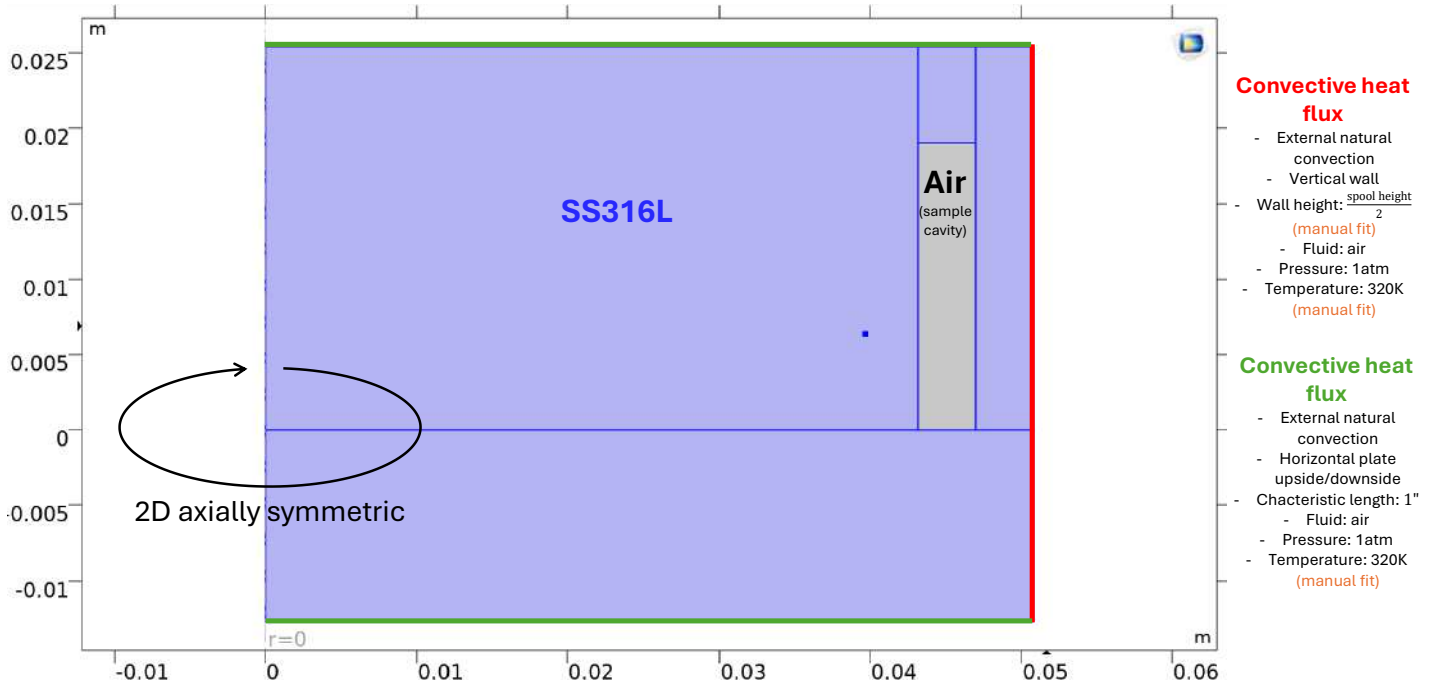
Material parameters:
- **Air**: COMSOL default
- **SS316L**: Thermal conductivity $14\,W/(m \cdot K)$, Density $8000\,kg/m^3$, Heat capacity $500\,J/(kg \cdot K)$ (Source: www.matweb.com)

Figure C.1: Geometry and parameters for the 2D axially symmetric COMSOL simulation of a spool warm-up.

Figure C.2: Results from the COMSOL simulation to compare the temperature at the sensor position and in the sample cavity. The maximum temperature difference between the sample cavity and the sample position obtained from this simulation is 8.11 K. An experiment will be conducted in the future to confirm the maximum sensor offset reached during temperature transients.

Appendix D

OpenMC code for effective dose rate simulation

I used the following Jupyter notebook to calculate the effective dose rate using the OpenMC Monte-Carlo code [81]. The methodology and results are presented in 2.5.

```python
%matplotlib inline
import matplotlib.pyplot as plt
%env OPENMC_CROSS_SECTIONS = /home/aulegoup/openmc_config/endfb71_hdf5/cross_sections.xml
import openmc
import os
import numpy as np
from uncertainties import ufloat
```

env: OPENMC_CROSS_SECTIONS=/home/aulegoup/openmc_config/endfb71_hdf5/cross_sections.xml

General parameters of the model

```python
#%% Geometry and material definition

#Increase details
Sample_height = 1 #cm
Spool_height= 1.5*2.54 #cm
Chamber_height= 20.47 #cm
Source_height = 21.11 #cm
Source_pitchcirclediameter = 20.91 #cm
Nb_pencils=48
Diam_pencil=np.pi*Source_pitchcirclediameter/Nb_pencils #cm , estimated from gammacell manual,
                                                         #it seems that they occupy the whole circle


#Changes from model with dewar and spool to empty chamber
only_air_in_chamber = False
#Sample vertical position
# z_spool = 0
z_spool = -Chamber_height/2 + 2.54*(7.625-(6.75-2)) #z coordinate of the center of the spool and of the
                                                     #center of the dose rate calculation cell
                                                     #(origin is center of the chamber)
print(z_spool)
#Liquid N2 level
z_ln2 = -Chamber_height/2 + 2.54*(7.625-3) #z coordinate of the ln2 surface level
# z_ln2 = +Chamber_height/2 - 1e-3 #if filled with LN2
# z_ln2 = z_spool + Spool_height/2 #if filled with LN2


#GENERAL PARAMETERS
C0=667.5e12 #Bq : total source activity
ENERGIES = [1.1732,1.3325] #MeV


#GEOMETRY
inwallD=5.5 #in
ouwallD=5.81 #in
inwallth=0.04 #in (between 0.020" and 0.060")
ouwallth=0.065 #in (between 0.030" and 0.100")
vacuumgap = (ouwallD-inwallD)/2 - inwallth - ouwallth #in (between 0.040" and 0.200")
print(f"The vacuum gap is {vacuumgap} inches. It is supposed to be between 0.040in and 0.200in")
##################################

radiusforevalofcentraldoserate = 0.2*2.54 #cm

RADII =     [3.4/2   ,3.7/2,4/2      ,inwallD/2,inwallD/2+inwallth,ouwallD/2-ouwallth,ouwallD/2,6.1/2] #in
print(f"Layers (r in in.) : {RADII}")
RADII = [2.54*r for r in RADII] #cm
MATERIAL = ["SS316L","Air","SS316L","LN2","SUS304","Vacuum","SUS304" ,"Air"]


FIBER = {"r_f":3.55/2*2.54, #cm
         "mat":"SiO2"}

# MATERIAL
Dic_Density ={ #g/cc  #Hypothesis: to conserve mass, we choose to set the density at ambiant temperature
                      #density, because the geometry corresponds to ambiant temperature geometry
    "SS316L":8.00, # https://matweb.com/search/DataSheet.aspx?
```

```python
                        #MatGUID=a2d0107bf958442e9f8db6dc9933fe31&ckck=1
    "Air":1.204e-3, # https://www.princeton.edu/~maelabs/hpt/mechanics/mecha_36.htm#:
                        #~:text=Air%20at%20atmospheric%20pressure%20(1.013,of%201.204%20kg%2Fm3.
    "LN2":0.808, # https://lasers.colostate.edu/wp-content/uploads/2019/04/Cryogenic-Safety-Manual.pdf
    "SUS304":8.00, # https://matweb.com/search/DataSheet.aspx?MatGUID=abc4415b0f8b490387e3c922237098da
    "Vacuum":1.204e-3*1e-6, #We replace vacuum by low pressure air (1e-6)
    "SiO2":2.2, # (roughly) https://www.sciencedirect.com/topics/
                            #earth-and-planetary-sciences/silica-glass
    }

OinCO2=2*15.999/(12.011+2*15.999)
CinCO2=12.011/(12.011+2*15.999)
print(OinCO2,CinCO2)

Weight_fractions={
    "SUS304":{"Cr":19/100,
              "Ni":9.25/100,
              "Mo":0,
              "C":0.04/100,
              "Mn":1/100,
              "P":0.0225/100,
              "S":0.015/100,
              "Si":0.5/100,
              "N":0,
              "Fe":70.1725/100}, #https://matmatch.com/learn/material/sus304-stainless-steel-ss304
    "SS316L":{"Cr":17/100,
              "Ni":12/100,
              "Mo":2.5/100,
              "C":0.015/100,
              "Mn":1/100,
              "P":0.0225/100,
              "S":0.015/100,
              "Si":0.375/100,
              "N":0.05/100,
              "Fe":67.0225/100}, #https://www.sandmeyersteel.com/images/316-316l-317l-spec-sheet.pdf
    "Air":{"N":75.511/100,
           "O":23.14/100 + OinCO2*0.063/100,
           "Ar":1.29/100,
           "C":CinCO2*0.063/100}, #Last ones ignored in https://www.engineeringtoolbox.com/
                                                #air-composition-d_212.html

    "LN2":{"N":1},
    "SiO2":{"O":0.532565,"Si":0.467435},
    #"Vacuum":{} We replace vacuum by low pressure air
    "Vacuum":{"N":75.511/100,
           "O":23.14/100 + OinCO2*0.063/100,
           "Ar":1.29/100,
           "C":CinCO2*0.063/100}, #Last ones ignored in
                                    #https://www.engineeringtoolbox.com/air-composition-d_212.html
    }

#Renormalize to 1 for Air
sair=np.sum(list(Weight_fractions["Air"].values()))
for elem in Weight_fractions["Air"].keys():
    Weight_fractions["Air"][elem]/=sair

#Check that all weight fractions add up to 1 for each material
for mat in Weight_fractions.keys():
    s=np.sum(list(Weight_fractions[mat].values()))
    print(f"{mat} total :{s}")

#Mass energy absorption coefficient NIST XCOM
 #First, determine the most precise energy grid:
database='/home/aulegoup/Optical_fibers/GammaDoseRateCalc/NIST_XCOM_data'
ENERGYLIST=[]
for file in [f for f in os.listdir(database) if ".txt" in f]:
    with open(os.path.join(database,file),'r') as f:
        LINES= f.readlines()[1:]
        for l in LINES:
            e = float(l.split(' ')[0])
            if e not in ENERGYLIST:
```

```
                    ENERGYLIST+=[e]
ENERGYLIST=np.sort(ENERGYLIST)

MassEnergyAbsCoeftimesE={}
for mat in Weight_fractions.keys():
    coefmat=np.zeros(len(ENERGYLIST))
    for elem in Weight_fractions[mat].keys():
        file=f"nist_{elem}.txt"
        with open(os.path.join(database,file),'r') as f:
            LINES= f.readlines()[1:]
            LINES=[l for l in LINES if '.' in l]
            Energies_elem, MUenRHO_elem = [float(l.split(' ')[0]) for l in LINES],[float(l.split(' ')[2]) fo
        coefmat += Weight_fractions[mat][elem]*np.interp(ENERGYLIST, Energies_elem, MUenRHO_elem)
    MassEnergyAbsCoeftimesE[mat]=coefmat*ENERGYLIST

ENERGYLIST*=1e6

for mat in MassEnergyAbsCoeftimesE.keys():
    if mat!="Vacuum":
        plt.plot(ENERGYLIST/1e6,MassEnergyAbsCoeftimesE[mat],label=mat)
plt.xscale("log")
plt.yscale("log")
plt.legend()
plt.xlabel("Energy (MeV)")
plt.ylabel(r"$\mu_{en}/\rho\times E$ (MeV.cm$^2$/s)")

save=False
if save:
    plt.savefig("MassEnergyAbsCoef.pdf", bbox_inches='tight')
else:
    plt.show()
```

```
-2.932499999999999
The vacuum gap is 0.049999999999999795 inches. It is supposed to be between 0.040in and 0.200in
Layers (r in in.) : [1.7, 1.85, 2.0, 2.75, 2.79, 2.84, 2.905, 3.05]
0.7270785521143402 0.27292144788565975
SUS304 total :1.0
SS316L total :1.0
Air total :0.9999999999999999
LN2 total :1
SiO2 total :1.0
Vacuum total :1.00004
```
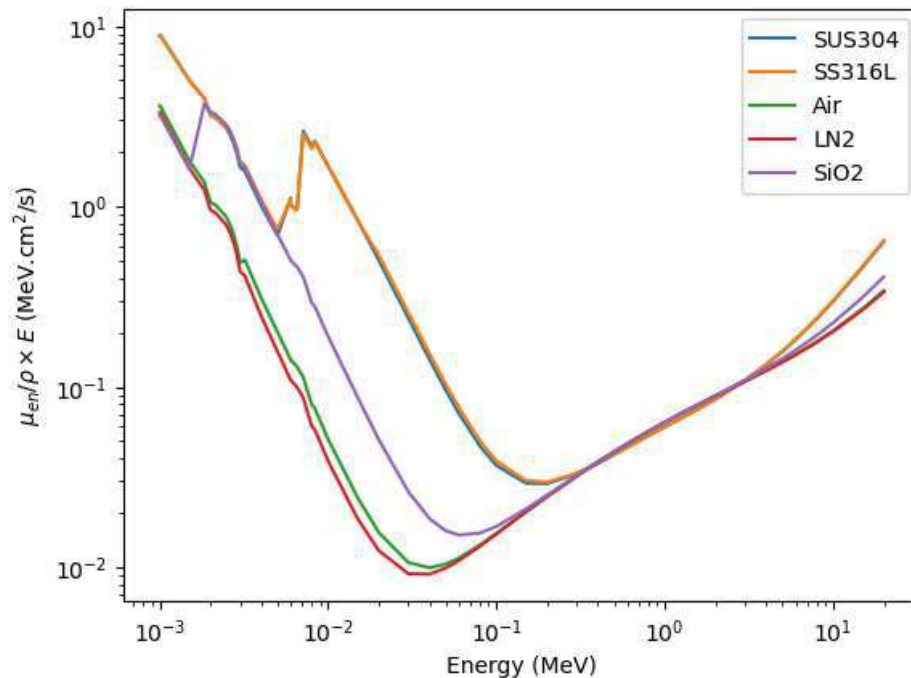
Defining settings

```
In [3]: print([99.85/(99.85+99.9826),99.9826/(99.85+99.9826)])
```

```
[0.49966822230206676, 0.5003317776979331]
```

```
In [4]: settings = openmc.Settings()
        #Photon source

        SOURCES=[]
        for theta in [2*np.pi*i/Nb_pencils for i in range(Nb_pencils)]:
            r_stat,phi_stat,z_stat = openmc.stats.Uniform(0.0,Diam_pencil/2),openmc.stats.Uniform(0.0, 2*np.pi),open
            SOURCES += [openmc.IndependentSource()]
            SOURCES[-1].space = openmc.stats.CylindricalIndependent(r_stat, phi_stat, z_stat, origin=(Source_pitchci
            SOURCES[-1].angle = openmc.stats.Isotropic()
            SOURCES[-1].energy = openmc.stats.Discrete([1.173228e6,1.332492e6], [99.85/(99.85+99.9826),99.9826/(99.8
            SOURCES[-1].particle = 'photon'
            SOURCES[-1].strength = 1/Nb_pencils
        settings.source = SOURCES

        #Enable photon transport
        settings.photon_transport = True

        #Nb particles & batches
        settings.batches = 200
        settings.inactive = 0 # Not needed in fixed source simulation
        settings.particles = 100000
        settings.temperature = {'method': 'interpolation','range':(77,300)}
        settings.verbosity = 5
        settings.run_mode = 'fixed source'

        #Entropy mesh
        entropy_mesh = openmc.RegularMesh()
        r_m=RADII[-1]+0.5
        entropy_mesh.lower_left = (-r_m, -r_m)
        entropy_mesh.upper_right = (r_m, r_m)
        entropy_mesh.dimension = (8, 8)

        settings.export_to_xml()
```

Defining materials

```
In [5]: Tcold=293.15
        Tamb=295

        #For each material, set name, id, temperature, density and composition
        def addMaterial(id, name, temp, key):
            mat=openmc.Material(id,name,temperature=temp)
            WFdict=Weight_fractions[key]
            for elem in WFdict.keys():
                if elem=='C':
                    mat.add_nuclide('C0',WFdict[elem],percent_type='wo')
                else:
                    mat.add_element(elem,WFdict[elem],percent_type='wo')
            mat.set_density('g/cm3',Dic_Density[key])
            return mat

        # SS316L
        ss316l = addMaterial(1,"SS316L",Tcold,"SS316L")
        # SiO2
        sio2 = addMaterial(2,"SiO2",Tcold,"SiO2")
        # LN2
        ln2 = addMaterial(3,"LN2",Tcold,"LN2")
        # SUS304 inside
        sus304in = addMaterial(4,"SUS304_in",Tcold,"SUS304")
        # Vacuum
```

```
vacuum = addMaterial(5,"Vacuum",Tamb,"Vacuum")
# SUS304 outside
sus304out = addMaterial(6,"SUS304_out",Tamb,"SUS304")
# Air
air = addMaterial(7,"Air",Tamb,"Air")

mats = openmc.Materials([ss316l,sio2,ln2,sus304in,vacuum,sus304out,air])
mats.cross_sections = '/home/aulegoup/openmc_config/endfb71_hdf5/cross_sections.xml'
mats.export_to_xml()
```

Defining geometry

```
In [6]:  # Define the surfaces
CYLINDERS = [openmc.ZCylinder(r=R) for R in RADII[:]]+[openmc.ZCylinder(r=(Source_pitchcirclediameter+Diam_p
CylCenterDReval = openmc.ZCylinder(r=radiusforevalofcentraldoserate)

LowPlane_sample = openmc.ZPlane(z0=z_spool-Sample_height/2)
HighPlane_sample = openmc.ZPlane(z0=z_spool+Sample_height/2)

LowPlane_spool = openmc.ZPlane(z0=z_spool-Spool_height/2)
HighPlane_spool = openmc.ZPlane(z0=z_spool+Spool_height/2)

HighPlane_ln2 = openmc.ZPlane(z0=z_ln2)

LowPlane_chamber = openmc.ZPlane(z0=-Chamber_height/2)
HighPlane_chamber = openmc.ZPlane(z0=Chamber_height/2)

LowPlane_model = openmc.ZPlane(z0=-Source_height/2-1e-6,boundary_type='vacuum')
HighPlane_model = openmc.ZPlane(z0=Source_height/2+1e-6,boundary_type='vacuum')

# Define the regions
centDReval_region = -CylCenterDReval & +LowPlane_sample & -HighPlane_sample
center_region    = +CylCenterDReval & -CYLINDERS[0] & +LowPlane_sample & -HighPlane_sample
sample_region    = +CYLINDERS[0] & -CYLINDERS[1] & +LowPlane_sample & -HighPlane_sample
outer316_region  = (+CYLINDERS[1] & -CYLINDERS[2] & +LowPlane_sample & -HighPlane_sample) | (-CYLINDERS[2] &
ln2_region       = (-CYLINDERS[3] & +LowPlane_chamber & -HighPlane_ln2) & ~(-CYLINDERS[2] & +LowPlane_spool
airaboveln2_region = -CYLINDERS[3] & +HighPlane_ln2 & -HighPlane_chamber #NEW
sus304in_region  = +CYLINDERS[3] & -CYLINDERS[4] & +LowPlane_chamber & -HighPlane_chamber
vacuum_region    = +CYLINDERS[4] & -CYLINDERS[5] & +LowPlane_chamber & -HighPlane_chamber
sus304out_region = +CYLINDERS[5] & -CYLINDERS[6] & +LowPlane_chamber & -HighPlane_chamber
air_region       = +CYLINDERS[6] & -CYLINDERS[7] & +LowPlane_chamber & -HighPlane_chamber
extvacuum_region = (-CYLINDERS[8] & +LowPlane_model & -HighPlane_model) & ~(-CYLINDERS[7] & +LowPlane_chambe

# Make Cells and Fill
if not(only_air_in_chamber):
    centDReval_cell= openmc.Cell(10, 'centDReval', fill=ss316l, region=centDReval_region)
    center_cell    = openmc.Cell(1, 'center', fill=ss316l, region=center_region)
    sample_cell    = openmc.Cell(2, 'sample', fill=sio2, region=sample_region)
    outer316_cell  = openmc.Cell(3, 'outer316', fill=ss316l, region=outer316_region)
    ln2_cell       = openmc.Cell(4, 'ln2', fill=ln2, region=ln2_region)
    airaboveln2_cell = openmc.Cell(11, 'airaboveln2', fill=air, region=airaboveln2_region) #NEW
    sus304in_cell  = openmc.Cell(5, 'sus304in', fill=sus304in, region=sus304in_region)
    vacuum_cell    = openmc.Cell(6, 'vacuum', fill=vacuum, region=vacuum_region)
    sus304out_cell = openmc.Cell(7, 'sus304out', fill=sus304out, region=sus304out_region)
    air_cell       = openmc.Cell(8, 'air', fill=air, region=air_region)
    extvacuum_cell = openmc.Cell(9, 'extvacuum', fill=vacuum, region=extvacuum_region)

else:
    centDReval_cell= openmc.Cell(10, 'centDReval', fill=air, region=centDReval_region)
    center_cell    = openmc.Cell(1, 'center', fill=air, region=center_region)
    sample_cell    = openmc.Cell(2, 'sample', fill=air, region=sample_region)
    outer316_cell  = openmc.Cell(3, 'outer316', fill=air, region=outer316_region)
    ln2_cell       = openmc.Cell(4, 'ln2', fill=air, region=ln2_region)
    airaboveln2_cell = openmc.Cell(11, 'airaboveln2', fill=air, region=airaboveln2_region) #NEW
    sus304in_cell  = openmc.Cell(5, 'sus304in', fill=air, region=sus304in_region)
    vacuum_cell    = openmc.Cell(6, 'vacuum', fill=air, region=vacuum_region)
    sus304out_cell = openmc.Cell(7, 'sus304out', fill=air, region=sus304out_region)
    air_cell       = openmc.Cell(8, 'air', fill=air, region=air_region)
```

```python
    extvacuum_cell = openmc.Cell(9, 'extvacuum', fill=vacuum, region=extvacuum_region)

DicVolCell={
10: Sample_height*np.pi*radiusforevalofcentraldoserate**2,
1 : Sample_height*np.pi*(RADII[0]**2-radiusforevalofcentraldoserate**2),
2 : Sample_height*np.pi*(RADII[1]**2-RADII[0]**2),
3 : Sample_height*np.pi*(RADII[2]**2-RADII[1]**2)+(Spool_height-Sample_height)*np.pi*RADII[2]**2,
4 : Spool_height*np.pi*(RADII[3]**2-RADII[2]**2)+(Chamber_height-Spool_height)*np.pi*RADII[3]**2 - (Chamber_
11: (Chamber_height/2-z_ln2)*np.pi*RADII[3]**2,
5 : Chamber_height*np.pi*(RADII[4]**2-RADII[3]**2),
6 : Chamber_height*np.pi*(RADII[5]**2-RADII[4]**2),
7 : Chamber_height*np.pi*(RADII[6]**2-RADII[5]**2),
8 : Chamber_height*np.pi*(RADII[7]**2-RADII[6]**2),
9 : Chamber_height*np.pi*(((Source_pitchcirclediameter+Diam_pencil)/2+1e-6)**2-RADII[7]**2)
    +(Source_height+2e-6-Chamber_height)*np.pi*((Source_pitchcirclediameter+Diam_pencil)/2+1e-6)**2,
}


root = openmc.Universe(cells=(centDReval_cell,center_cell, sample_cell, outer316_cell, ln2_cell, sus304in_ce
geom = openmc.Geometry(root)
geom.export_to_xml()

print(root.bounding_box)

#Plot the geometry
diccolors={ss316l:(0,0,0),
           sio2:(255,0,0),
           ln2:(0,200,255),
           sus304in:(122,102,76),
           vacuum:(150,255,205),
           sus304out:(140,102,76),
           air:(255,153,255)}
root.plot(origin=(0., 0., -3.), width=(6*2.54+1, 6*2.54+1), pixels=(500, 500), color_by='material',colors=di
root.plot(origin=(1.5*2.54, 1.5*2.54, -3), width=(3*2.54, 3*2.54), pixels=(500, 500),color_by='material',col
root.plot(origin=(0., 0., 0.), width=(6*2.54+1, 22), basis='xz', color_by='material',colors=diccolors, pixel

from matplotlib.patches import Patch
legend_elements = []
for mat in mats:
    # print(mat.name)
    MatIsHere = mat in [V.fill for V in root.cells.values()]
    if MatIsHere:
        colr = tuple([i/255 for i in diccolors[mat]])
        legend_elements += [Patch(facecolor=colr, edgecolor=colr,label=mat.name)]
plt.legend(handles=legend_elements, loc='best', shadow=True, facecolor="white", edgecolor="black",framealpha
if not(only_air_in_chamber):
    plt.title("OpenMC chamber geometry with setup installed")
else:
    plt.title("OpenMC empty chamber geometry")

save=False
if save:
    if not(only_air_in_chamber):
        plt.savefig("OpenMC_geom_full.pdf", bbox_inches='tight')
    else:
        plt.savefig("OpenMC_geom_empty.pdf", bbox_inches='tight')
else:
    plt.show()
```

BoundingBox(lower_left=(-11.139279149860027, -11.139279149860027, -10.555000999999999), upper_right=(11.13927
9149860027, 11.139279149860027, 10.555000999999999))
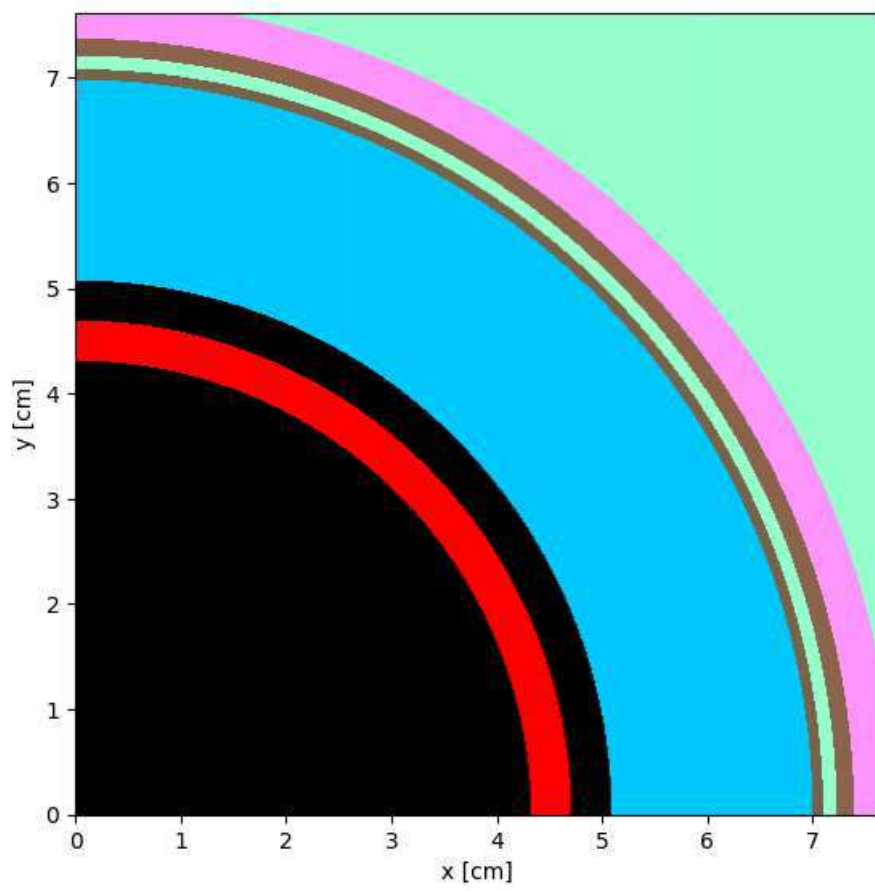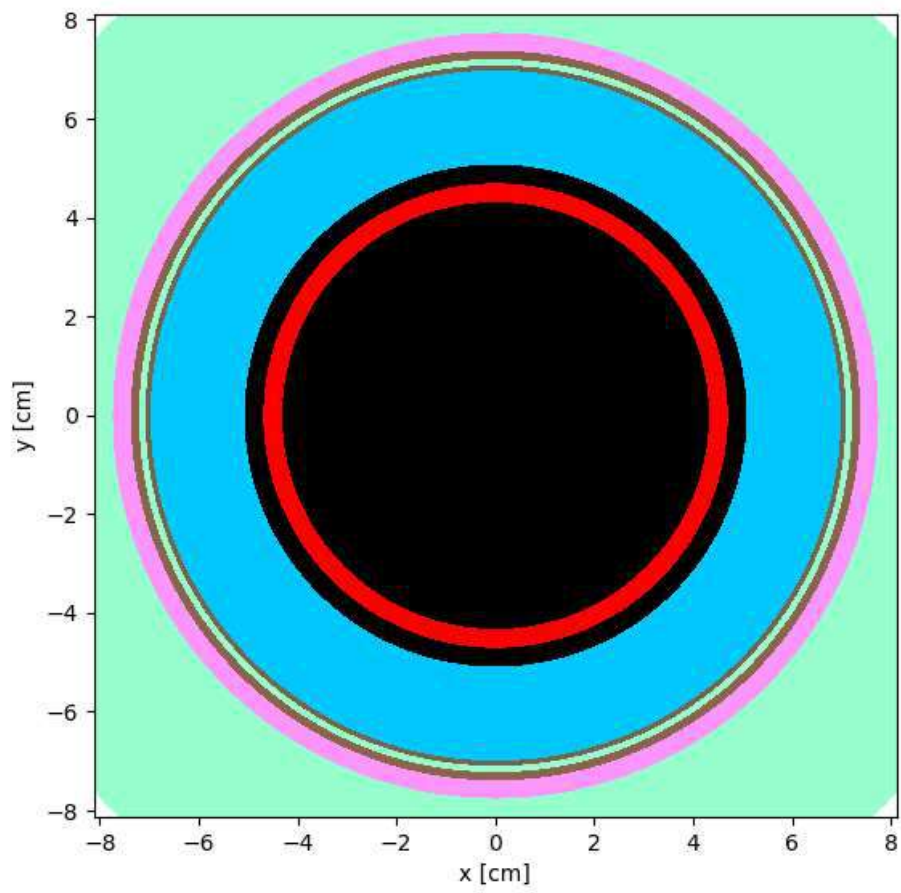
OpenMC chamber geometry with setup installed
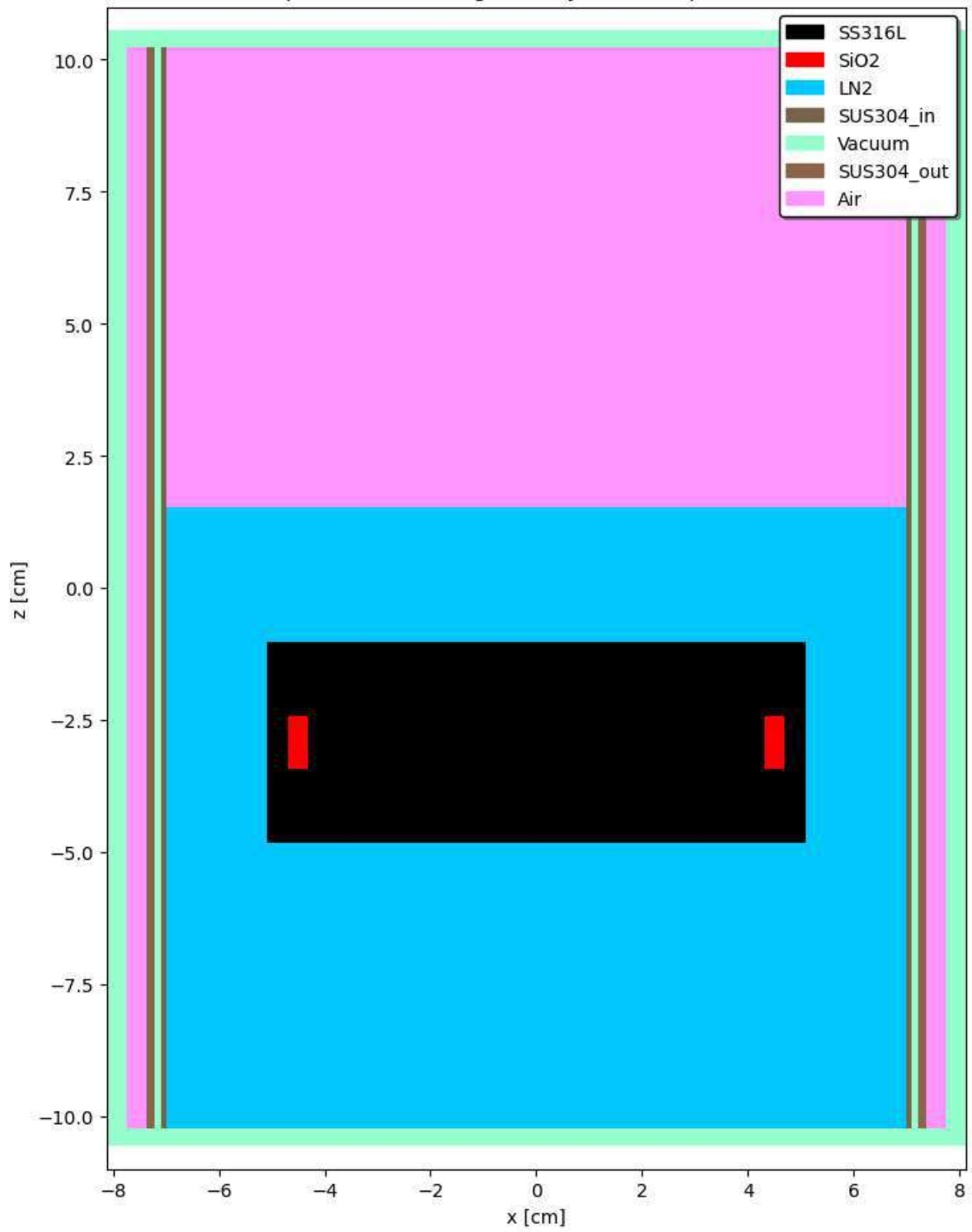
```
In [7]:  for mat in mats:
             print(mat.name)
             print(mat in [V.fill for V in root.cells.values()])
```

```
SS316L
True
SiO2
True
LN2
True
SUS304_in
True
Vacuum
True
SUS304_out
True
Air
True
```

Define the Tallies

```python
In [8]: def get_var_name(var):
            for name, value in globals().items():
                if value is var:
                    return name

        for cell in [centDReval_cell,center_cell, sample_cell, outer316_cell,ln2_cell, sus304in_cell, vacuum_cell, s
            print(get_var_name(cell),'\t', cell.fill.name.split('_')[0])
```

```
centDReval_cell          SS316L
center_cell       SS316L
sample_cell       SiO2
outer316_cell     SS316L
ln2_cell          LN2
sus304in_cell     SUS304
vacuum_cell       Vacuum
sus304out_cell    SUS304
air_cell          Air
extvacuum_cell    Vacuum
```

```python
In [ ]: tallies_file = openmc.Tallies()

        particle_filter = openmc.ParticleFilter('photon')

        #energy, dose = openmc.data.dose_coefficients('photon kerma', 'ISO')
        #dose_filter = openmc.EnergyFunctionFilter(energy, dose)
        #ENERGYLIST,MassEnergyAbsCoeftimesE[mat]
        DOSETALLIES=[]
        for cell in [centDReval_cell,center_cell, sample_cell, outer316_cell,ln2_cell, sus304in_cell, vacuum_cell, s
            name=get_var_name(cell)
            mat=cell.fill.name.split('_')[0]
            dose_filter = openmc.EnergyFunctionFilter(ENERGYLIST,MassEnergyAbsCoeftimesE[mat])
            cell_filter = openmc.CellFilter(cell)
            DOSETALLIES += [openmc.Tally(name=f"Photon dose tally - cell {name}")]
            DOSETALLIES[-1].filters = [particle_filter,dose_filter,cell_filter]
            DOSETALLIES[-1].scores = ['flux']
            tallies_file.append(DOSETALLIES[-1])

        FluxCylTally = openmc.Tally(name="Photon total flux - cylindrical mesh")
        r_grid=np.linspace(0.0, (Source_pitchcirclediameter+Diam_pencil)/2, 100)
        cylindrical_mesh = openmc.CylindricalMesh(r_grid = r_grid,
                                                  phi_grid = [0.0, 2*np.pi],
                                                  z_grid = [z_spool-Sample_height/2, z_spool+Sample_height/2])
        cylindrical_mesh_filter = openmc.MeshFilter(cylindrical_mesh)
        FluxCylTally.filters = [particle_filter,cylindrical_mesh_filter]
        FluxCylTally.scores = ['flux']
        tallies_file.append(FluxCylTally)

        samplecell_filter = openmc.CellFilter(sample_cell)
        energies = np.logspace(np.log10(1e-5), np.log10(2.0e6), 100000)
        e_filter = openmc.EnergyFilter(energies)
        fluxtally = openmc.Tally(name="Photon flux tally")
        fluxtally.filters = [particle_filter,e_filter]
```

```
fluxtally.scores = ['flux']
tallies_file.append(fluxtally)

tallies_file.export_to_xml()
```

Run OpenMC

In [10]:
```
openmc.run()

sp = openmc.StatePoint(f'statepoint.{settings.batches}.h5')

# os.remove('geometry.xml')
# os.remove('materials.xml')
# os.remove('settings.xml')
# os.remove('statepoint.100.h5')
# os.remove('summary.h5')
# del sp
```

[ASUS-Aurlien:208294] mca_base_component_repository_open: unable to open mca_btl_openib: librdmacm.so.1: cann
ot open shared object file: No such file or directory (ignored)

```
                         %%%%%%%%%%%%%%%
                    %%%%%%%%%%%%%%%%%%%%%%%%
                 %%%%%%%%%%%%%%%%%%%%%%%%%%%%%%%
               %%%%%%%%%%%%%%%%%%%%%%%%%%%%%%%%%%%
              %%%%%%%%%%%%%%%%%%%%%%%%%%%%%%%%%%%%%%
             %%%%%%%%%%%%%%%%%%%%%%%%%%%%%%%%%%%%%%%%
                            %%%%%%%%%%%%%%%%%%%%%%%%
                             %%%%%%%%%%%%%%%%%%%%%%%%
         ###############     %%%%%%%%%%%%%%%%%%%%%%%%
         ##################  %%%%%%%%%%%%%%%%%%%%%%%
         ###################  %%%%%%%%%%%%%%%%%%%%%%%
         ####################  %%%%%%%%%%%%%%%%%%%%%%
         #####################  %%%%%%%%%%%%%%%%%%%%%
         ######################  %%%%%%%%%%%%%%%%%%%%
         #######################  %%%%%%%%%%%%%%%%%%
          #######################  %%%%%%%%%%%%%%%%%
          ######################  %%%%%%%%%%%%%%%%%%
           ####################  %%%%%%%%%%%%%%%%%%
            #################  %%%%%%%%%%%%%%%%%%
             ##############  %%%%%%%%%%%%%%%%%%
              ###########  %%%%%%%%%%%%%%%%%
                ########  %%%%%%%%%%%%%%%%
                         %%%%%%%%%%%%
```

```
               | The OpenMC Monte Carlo Code
     Copyright | 2011-2023 MIT, UChicago Argonne LLC, and contributors
       License | https://docs.openmc.org/en/latest/license.html
       Version | 0.14.0
      Git SHA1 | e1a8ee7794b441c992426f17fafe216391cbba83
     Date/Time | 2024-07-30 11:44:35
 MPI Processes | 1
OpenMP Threads | 20

Reading settings XML file...
Reading cross sections XML file...
Reading materials XML file...
Reading geometry XML file...
WARNING: Negative value(s) found on probability table for nuclide Ar36 at 250K
WARNING: Negative value(s) found on probability table for nuclide Ar36 at 294K
WARNING: Negative value(s) found on probability table for nuclide Ar36 at 600K
Minimum neutron data temperature: 250 K
Maximum neutron data temperature: 600 K
Reading tallies XML file...
Preparing distributed cell instances...
Reading plot XML file...
Writing summary.h5 file...

===============>     FIXED SOURCE TRANSPORT SIMULATION     <===============

Creating state point statepoint.200.h5...

============================>     RESULTS     <============================

Leakage Fraction              = 0.98279 +/- 0.00003
```

In [11]:
```python
if not(only_air_in_chamber):
    print("For the 3D model with dewar and fiber sample :\n")
else:
    print("For an empty chamber (only air):\n")


print(f"z_spool = {z_spool:.2f} cm\n")


for cell in [centDReval_cell,center_cell, sample_cell, outer316_cell,ln2_cell, sus304in_cell, vacuum_cell, s
    name=get_var_name(cell)
    mat=cell.fill.name
    tally=sp.get_tally(name=f"Photon dose tally - cell {name}").get_pandas_dataframe()
```

```
        tallyvalue = ufloat(tally.get("mean").loc[0],tally.get("std. dev.").loc[0]) *C0/DicVolCell[cell.id] *1.6
        print(f"Cell {name} ({mat}) : {tallyvalue:.2f} kGy/h")
```

For the 3D model with dewar and fiber sample :

z_spool = -2.93 cm

Cell centDReval_cell (SS316L) : 6.08+/-0.08 kGy/h
Cell center_cell (SS316L) : 7.87+/-0.02 kGy/h
Cell sample_cell (SiO2) : 11.02+/-0.03 kGy/h
Cell outer316_cell (SS316L) : 9.32+/-0.01 kGy/h
Cell ln2_cell (LN2) : 13.14+/-0.01 kGy/h
Cell sus304in_cell (SUS304_in) : 15.48+/-0.01 kGy/h
Cell vacuum_cell (Vacuum) : 16.59+/-0.01 kGy/h
Cell sus304out_cell (SUS304_out) : 16.34+/-0.01 kGy/h
Cell air_cell (Air) : 18.51+/-0.01 kGy/h
Cell extvacuum_cell (Vacuum) : 29.85+/-0.01 kGy/h
Cell airaboveln2_cell (Air) : 14.63+/-0.01 kGy/h
```

In [12]:
```python
tally=sp.get_tally(name="Photon flux tally").get_pandas_dataframe()
print(list(tally.columns))
energy_low,energy_high,flux = np.array(tally["energy low [eV]"]),np.array(tally["energy high [eV]"]),np.arra
plt.plot((energy_low+energy_high)/2e6,flux)
plt.xlabel("Photon energy (MeV)")
plt.ylabel("Flux tally")
plt.show()
```

['particle', 'energy low [eV]', 'energy high [eV]', 'nuclide', 'score', 'mean', 'std. dev.']
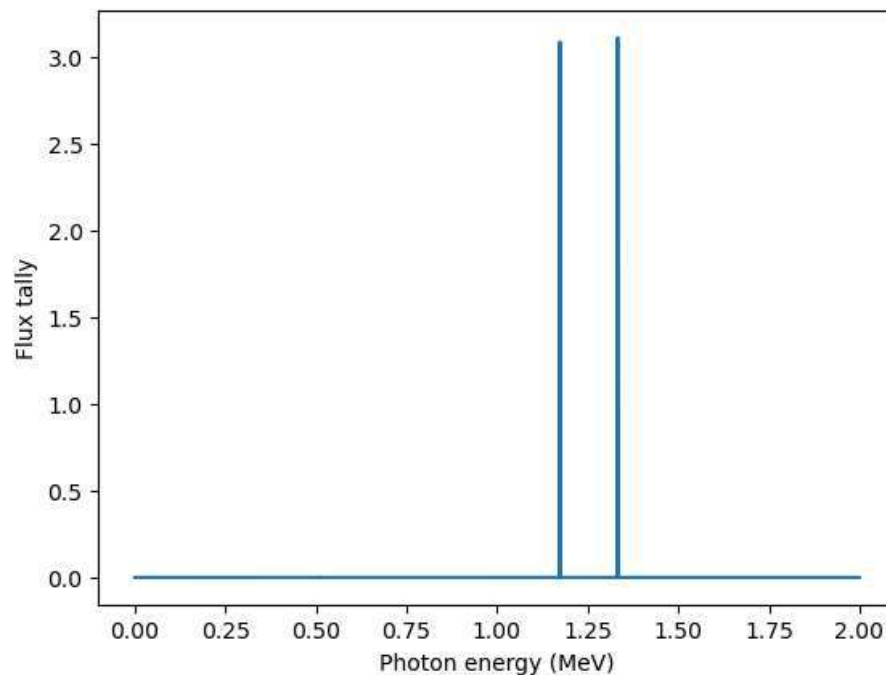
In [13]:
```python
tally=sp.get_tally(name="Photon total flux - cylindrical mesh").get_pandas_dataframe()
# print(r_grid)
flux=np.array([ufloat(m,s) for m,s in zip(tally.get('mean').tolist(),tally.get('std. dev.').tolist())])
flux /= Sample_height*np.pi*(r_grid[1:]**2-r_grid[:-1]**2)
# print(flux)
plt.errorbar(r_grid[:-1],[f.n for f in flux], yerr=[f.s for f in flux])
plt.axvline(x=6.1/2*2.54,color='k')
plt.xlabel('r')
plt.ylabel('flux')
plt.show()
atwall=next(flux[x] for x,val in enumerate(r_grid) if val>6.1/2*2.54)
print(f"Ratio between flux at chamber wall and flux at center : {atwall/flux[0]*100} %")
```
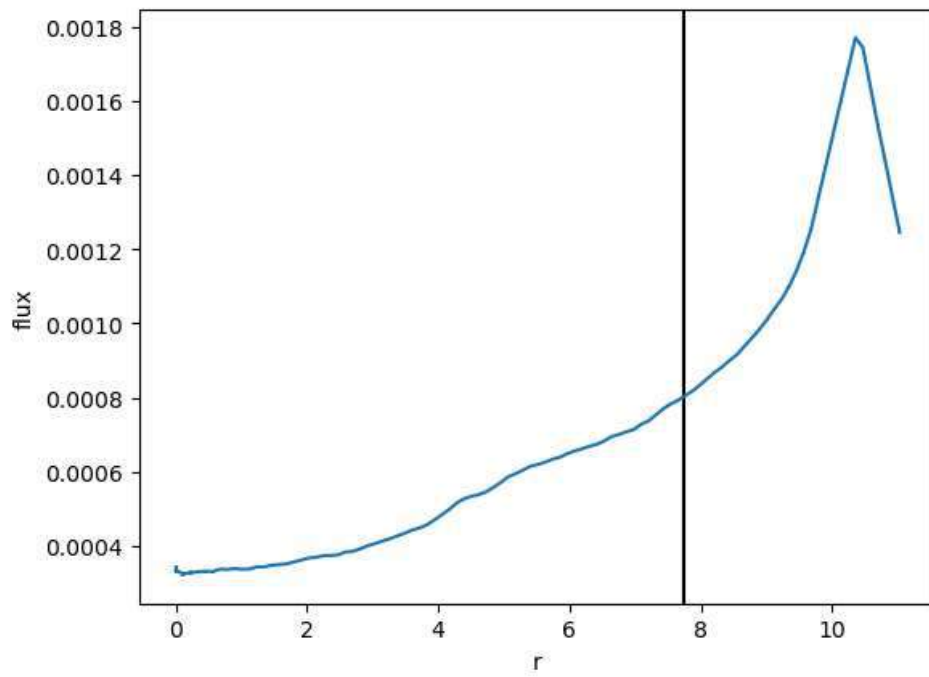
Ratio between flux at chamber wall and flux at center : 240+/-7 %

Appendix E

Data analysis Python code

This appendix contains the following Python packages (in order):

- `rmnoise.py` contains the function to remove the left part of absorption spectra that falls below the spectrometer noise floor.

- `MSsmoothing.py` implements in Python the modified sinc kernel filter proposed by Schmid et al. in [65].

- `gaussdec.py` implements the non-linear least squares decomposition of RIA spectra over the absorption bands known from the literature.

All code used in this thesis work is made available at https://github.com/shortlab/2024-Legoupil-SM-Thesis.

```python
# -*- coding: utf-8 -*-
"""
rmnoise.py

Function to filter out the noise region of my spectra in the different analysis notebook

@author: Aurelien Legoupil
"""

import numpy as np

def firstid(data, half_width_test = 40, noise_threshold = -75):
    extdata = np.zeros(len(data)+2*half_width_test)
    extdata[half_width_test:half_width_test+len(data)]=data
    TESTF_bool = [not(np.any(extdata[i:i+2*half_width_test] < noise_threshold)) for i in
    ↪  range(len(data))]
    try:
        I=next(id for id,bool in enumerate(TESTF_bool) if bool)
    except StopIteration:
        I=len(data)
    return I
```

```python
# -*- coding: utf-8 -*-
"""
MSsmoothing.py

Package for smoothing according to Schmid et al. 2022 "Why and How SavitzkyGolay Filters Should Be
    Replaced"
https://doi.org/10.1021/acsmeasuresciau.1c00054

@author: Aurelien Legoupil
"""

import numpy as np

CorrCoeffsMS_dic={
    2:[],
    4:[],
    6:[[0.001717576, 0.02437382, 1.64375]],
    8:[[0.0043993373, 0.088211164, 2.359375], #j=0
        [0.006146815, 0.024715371, 3.6359375]],#j=1
    10:[[0.0011840032, 0.04219344, 2.746875], #j=0
        [0.0036718843, 0.12780383, 2.7703125]]#j=1
}

def windowsMS(x,alpha):
    '''
    w_a(x) from (4)
    '''
    return np.exp(-alpha*x**2) + np.exp(-alpha*(x+2)**2) + np.exp(-alpha*(x-2)**2) -
        2*np.exp(-alpha) - np.exp(-9*alpha)

def kernelMS(n,m,alpha=4):
    '''
    Function that returns the convolution kernel array a (eq (3) schmid et al)
    Inputs:
        - m : half size of kernel (kernel size: 2m+1
        - n : degree
        - alpha : steepness parameter. value 4 from 2.2 in schmid et al
    '''
    KAPPA = [ a + b/(c-m)**3 for [a,b,c] in CorrCoeffsMS_dic[n] ]
    X = [i/(m+1) for i in range(-m,m+1)]
    nu = 2 - ((n/2)%2)
    A = np.array([windowsMS(x,alpha) * (
                    np.sinc((n+4)/2*np.pi*x)
                + np.sum([ kappa*x*np.sin((2*j+nu)*np.pi*x) for j,kappa in enumerate(KAPPA) ])
    ) for x in X])
    A /= np.sum(A)
    return A
```

```python
47    def edgeWeights(n,m):
48        '''
49        Hann-square weights for linear fit at the edges from (17) and (18)
50        Inputs:
51            - m : half size of kernel (kernel size: 2m+1
52            - n : degree
53        '''
54        beta = 0.7 + 0.14*np.exp(-0.6*(n-4))
55        fitlengthD = (m+1)*beta/(1.5+0.5*n)
56        fitlength = int(np.floor(fitlengthD))
57        return np.array([ (np.cos(np.pi/2*i/fitlengthD))**2  for i in range(fitlength+1) ])

58
59    def fitWeighted(xData,yData,weights):
60        sumWeights = np.sum(weights)
61        sumX = np.sum(xData*weights)
62        sumY = np.sum(yData*weights)
63        sumX2 = np.sum(xData**2*weights)
64        sumXY = np.sum(xData*yData*weights)
65        varX2 = sumX2*sumWeights - sumX**2
66        if varX2==0:
67            slope=0
68        else:
69            slope = (sumXY*sumWeights - sumX*sumY)/varX2
70        offset = (sumY-slope*sumX)/sumWeights
71        return offset,slope

72
73    def extendData(data,m,fitWeights):
74        '''
75        Extends the data by weighted linear extrapolation, for smoothing to the ends
76        '''
77        extData=np.zeros(len(data)+2*m)
78        extData[m:len(data)+m]=data
79        fitX = np.arange(len(fitWeights))
80        fitY = data[:len(fitWeights)]
81        offset,slope = fitWeighted(fitX,fitY,fitWeights)
82        extData[:m] = [offset + slope*x for x in range(-m+1,1)]
83        fitY = data[-len(fitWeights):][::-1]
84        offset,slope = fitWeighted(fitX,fitY,fitWeights)
85        extData[-m:]= [offset + slope*x for x in range(-m+1,1)][::-1]
86        return extData

87
88    def smoothMS(data,n,m):
89        '''
90        MS data smoothing (see Schmid et al) with correction and linear extrapolation for edge
          ↪  smoothing
91        Inputs:
92            - data : row vector on which to apply smoothing
93            - m : half size of kernel (kernel size: 2m+1
94            - n : degree
```

```python
        '''
        kernel = kernelMS(n,m)
        fitWeights = edgeWeights(n,m)
        extData = extendData(data,m,fitWeights)
        smoothedExtData = np.convolve(extData, kernel, mode="same")
        smoothedData = smoothedExtData[m:len(data)+m]
        return smoothedData
```

```python
# -*- coding: utf-8 -*-
"""
gaussdec.py

@author: Aurelien Legoupil
"""

#%% Imports
import numpy as np
from scipy.optimize import curve_fit

#%% Catalog of defect peaks
# Nameofdefect, peak number, OA peak eV , FWHM eV, sources (list)

#GR91 = Griscom, 1991
#GI19 = Girard, 2019
#KA22 = Kashaykin, 2022
#MO20 = Morana, 2020

#{"peak":,"FWHM":,"sources":["GI19"]}
#FWHM=1e-6 when unknown

DICOPEAKS = {
    "ODC-II":[
        {"peak":5.05,"FWHM":0.32,"sources":["GI19"]},
        {"peak":3.15,"FWHM":0.30,"sources":["GI19"]},
        {"peak":6.9,"FWHM":0.4,"sources":["GI19"]}
        ],
    "ODC-I":[
        {"peak":7.6,"FWHM":{"min":0.5,"max":0.6},"sources":["GI19"]}
        ],
    "NBOHC":[
        {"peak":1.97,"FWHM":0.17,"sources":["GI19"]},
        {"peak":4.8,"FWHM":1.0,"sources":["GI19"]},
        {"peak":6.4,"FWHM":1.7,"sources":["GI19"]}
        ],
    "E-prime":[
        {"peak":5.8,"FWHM":0.7,"sources":["GI19"]}
        ],
    "STH1":[
        {"peak":2.61,"FWHM":1.2,"sources":["GI19"]},
        {"peak":1.88,"FWHM":{"min":0.2,"max":0.5},"sources":["GI19"]}
        ],
    "STH2":[
        {"peak":2.16,"FWHM":{"min":0.3,"max":0.6},"sources":["GI19"]},
        {"peak":1.63,"FWHM":{"min":0.3,"max":0.7},"sources":["GI19"]}
        ],
    "POL":[
```

```
49          {"peak":3.8,"FWHM":0.2,"sources":["GI19"]},
50          {"peak":4.2,"FWHM":0.6,"sources":["GI19"]},
51          {"peak":7.3,"FWHM":0.2,"sources":["GI19"]},
52          {"peak":7.5,"FWHM":0.1,"sources":["GI19"]}
53          ],
54      "POR":[
55          {"peak":2.02,"FWHM":None,"sources":["GI19"]},
56          {"peak":4.08,"FWHM":None,"sources":["GI19"]},
57          {"peak":5.02,"FWHM":None,"sources":["GI19"]},
58          {"peak":2.0,"FWHM":None,"sources":["GI19"]},
59          {"peak":4.8,"FWHM":None,"sources":["GI19"]}
60          ],
61      "STE":[
62          {"peak":3.7,"FWHM":None,"sources":["GI19"]},
63          {"peak":4.6,"FWHM":None,"sources":["GI19"]},
64          {"peak":6.4,"FWHM":None,"sources":["GI19"]}
65          ],
66      "STEX":[
67          {"peak":4.2,"FWHM":1.16,"sources":["GI19"]},
68          {"peak":5.3,"FWHM":0.78,"sources":["GI19"]}
69          ],
70      "Composite 1-eV band":[
71          {"peak":1.2,"FWHM":0.56,"sources":["KA22","MO20"]},
72          {"peak":0.93,"FWHM":0.42,"sources":["KA22","MO20"]}
73          ]
74      }
75
76  DICOIMPUR = {
77      "O3":[
78          {"peak":4.8,"FWHM":{"min":0.8,"max":0.86},"sources":["GI19"]}
79          ],
80      "O2":[
81          {"peak":0.97,"FWHM":0.013,"sources":["GI19"]},
82          {"peak":1.62,"FWHM":0.013,"sources":["GI19"]}
83          ],
84      "Cl0":[
85          {"peak":3.26,"FWHM":None,"sources":["GI19"]},
86          {"peak":3.65,"FWHM":None,"sources":["GI19"]}
87          ],
88      "Cl2":[
89          {"peak":3.78,"FWHM":0.6,"sources":["GI19"]},
90          {"peak":2.3,"FWHM":None,"sources":["GI19"]}
91          ],
92      "H(I)":[], #not observed
93      "LTIRA":[] #non gaussian, see Girard 2019, Dianov Chernov 1989
94      }
95
96  DICOLTIRA = {"D":0.39, #eV (even if they say eV^-1?) #From Ka22 and Dianov-Chernov 89
97              "S":0.11, #eV (even if they say eV^-1?)
```

```
 98                    "R":0.43, #eV (even if they say eV^-1?)
 99                    "Ep":0.65 #eV
100                    }
101
102   #%% Helper functions
103
104   def Sigma(FWHM):
105       return FWHM/(2*np.sqrt(2*np.log(2)))
106
107   eV = 1.60218e-19 #J
108   h_Planck = 6.62607015e-34 #m^2.kg/s
109   c_light = 299792458 #m/s
110   def eV2WLnm(E):
111       return h_Planck*c_light/(E*eV*1e-9) #in nm
112   def WLnm2eV(lmbda):
113       return h_Planck*c_light/(lmbda*1e-9*eV)
114
115
116   #%% Functions for bands
117
118   def LTIRAfunc(lmbda,magnitude,D,S,R,Ep,model="Kubo-Greenwood"):
119       E = WLnm2eV(lmbda)
120       if magnitude==0:
121           return 0
122       if model=="Kubo-Greenwood":
123           Q=D+S/(D-S)
124           B0=magnitude
125           return B0*E*np.exp(-E/S)*(np.exp(E/Q)-np.exp(Ep/Q))
126       elif model=="exp":
127           C=magnitude
128           return (C*np.exp(-E/R))
129       else:
130           raise NameError("You fucked up")
131
132   def gaussband(lmbda,magnitude,peak_eV,FWHM_eV):
133       E = WLnm2eV(lmbda)
134       sigma = Sigma(FWHM_eV)
135       return magnitude/(sigma*np.sqrt(2*np.pi)) * np.exp(-(E-peak_eV)**2/(2*sigma**2))
136
137   #%% Function for total absorption fitting
138
139   def totabs(lmbda,
140              ltira_magnitude,ltira_D,ltira_S,ltira_R,ltira_Ep,
141              *paramsgauss):
142
143       assert len(paramsgauss)%3==0
144       n_gaussians=int(len(paramsgauss)/3)
145
146       total = LTIRAfunc(lmbda, ltira_magnitude, ltira_D, ltira_S, ltira_R, ltira_Ep)
```

```python
147         #Add gaussian bands:
148         for i in range(n_gaussians):
149             magnitude = paramsgauss[i*3]
150             peak_eV = paramsgauss[i*3+1]
151             FWHM_eV = paramsgauss[i*3+2]
152             total += gaussband(lmbda, magnitude, peak_eV, FWHM_eV)
153
154         return total
155
156     #%%
157
158     def decompose(lmbdadata,ydata,LTIRA=False,GaussList=[],fixedreldelta=1e-6,⌋
    ↪   defautfwhm_minmaxinit=(1e-6,2,0.1),relmaxfev=100,defaultmag=1e2):
159         #GaussList must be a list of keys in DICOPEAKS or DICOIMPUR, setting these gaussians as
        ↪   available for decomposition
160         #Possible improvements if necessary after decomposition attempt:
161             #give margin for ltira parameters and other fixed parameters (in percent?)
162             #modify the optimization ranges for peaks with unknown FWHM
163
164         #Construct the intial guess and parameter ranges for curve fitting
165
166         d_minus = 1-fixedreldelta/2
167         d_plus  = 1+fixedreldelta/2
168
169         low_bounds=[]
170         high_bounds=[]
171         if LTIRA:
172             initial_guesses =[defaultmag,DICOLTIRA["D"],DICOLTIRA["S"],DICOLTIRA["R"],DICOLTIRA["Ep"]]
173             low_bounds=[0,DICOLTIRA["D"]*d_minus,DICOLTIRA["S"]*d_minus,DICOLTIRA["R"]*d_minus,⌋
            ↪   DICOLTIRA["Ep"]*d_minus]
174             high_bounds=[np.inf,DICOLTIRA["D"]*d_plus,DICOLTIRA["S"]*d_plus,DICOLTIRA["R"]*d_plus,⌋
            ↪   DICOLTIRA["Ep"]*d_plus]
175         else:
176             initial_guesses =[0,DICOLTIRA["D"],DICOLTIRA["S"],DICOLTIRA["R"],DICOLTIRA["Ep"]]
177             low_bounds=[0-fixedreldelta/2,DICOLTIRA["D"]*d_minus,DICOLTIRA["S"]*d_minus,⌋
            ↪   DICOLTIRA["R"]*d_minus,DICOLTIRA["Ep"]*d_minus]
178             high_bounds=[0+fixedreldelta/2,DICOLTIRA["D"]*d_plus,DICOLTIRA["S"]*d_plus,⌋
            ↪   DICOLTIRA["R"]*d_plus,DICOLTIRA["Ep"]*d_plus]
179
180         for KeyGauss in GaussList:
181             if KeyGauss in DICOPEAKS.keys():
182                 PEAKS=DICOPEAKS[KeyGauss]
183             elif KeyGauss in DICOIMPUR.keys():
184                 PEAKS=DICOIMPUR[KeyGauss]
185             else:
186                 PEAKS=[]
187             for dicpeak in PEAKS:
188                 if dicpeak["FWHM"]==None:
189                     initial_guesses+=[defaultmag,dicpeak["peak"],defautfwhm_minmaxinit[2]]
```

```
190                    low_bounds+=[0,dicpeak["peak"]*d_minus,defautfwhm_minmaxinit[0]]
191                    high_bounds+=[np.inf,dicpeak["peak"]*d_plus,defautfwhm_minmaxinit[1]]
192              elif type(dicpeak["FWHM"])==float:
193                    initial_guesses+=[defaultmag,dicpeak["peak"],dicpeak["FWHM"]]
194                    low_bounds+=[0,dicpeak["peak"]*d_minus,dicpeak["FWHM"]*d_minus]
195                    high_bounds+=[np.inf,dicpeak["peak"]*d_plus,dicpeak["FWHM"]*d_plus]
196              elif type(dicpeak["FWHM"])==dict:
197                    initial_guesses+=[defaultmag,dicpeak["peak"],⌋
     ↪   (dicpeak["FWHM"]["min"]+dicpeak["FWHM"]["max"])/2]
198                    low_bounds+=[0,dicpeak["peak"]*d_minus,dicpeak["FWHM"]["min"]]
199                    high_bounds+=[np.inf,dicpeak["peak"]*d_plus,dicpeak["FWHM"]["max"]]
200
201      #Apply curve fitting
202      popt, pcov = curve_fit(totabs, lmbdadata, ydata, p0=initial_guesses,
     ↪   bounds=(low_bounds,high_bounds),max_nfev=relmaxfev*len(initial_guesses))
203
204      return popt,pcov
205
206
207
208
209
210
211
```

References

[1] O. Duke, A. Greenberg, J. Desroches, J. Schuyt, D. Moseley, and E. Salazar, "Reducing radiation effects on fiber optic quench detection sensors with optical annealing," *IEEE Transactions on Applied Superconductivity*, pp. 1–5, 2024. DOI: 10.1109/TASC.2023.3347369.

[2] E. E. Salazar, R. A. Badcock, M. Bajko, *et al.*, "Fiber optic quench detection for large-scale HTS magnets demonstrated on VIPER cable during high-fidelity testing at the SULTAN facility," *IOP Publishing*, 2021, Accepted: 2021-10-27T19:57:24Z Publisher: IOP Publishing. DOI: 10.1088/1361-6668/abdba8.

[3] M. Coatanea-Gouachet, D. Carrillo, S. Lee, and F. Rodriguez-Mateos, "Electromagnetic quench detection in ITER superconducting magnet systems," *IEEE Transactions on Applied Superconductivity*, vol. 25, no. 3, pp. 1–7, Jun. 2015. DOI: 10.1109/TASC.2015.2390296.

[4] A. Othonos, "Bragg gratings in optical fibers: Fundamentals and applications," in *Optical Fiber Sensor Technology: Advanced Applications — Bragg Gratings and Distributed Sensors*, K. T. V. Grattan and B. T. Meggitt, Eds., Boston, MA: Springer US, 2000, pp. 79–187, ISBN: 978-1-4757-6079-8. DOI: 10.1007/978-1-4757-6079-8_2.

[5] K. T. V. Grattan and T. Sun, "Fiber optic sensor technology: Introduction and overview," in *Optical Fiber Sensor Technology: Fundamentals*, K. T. V. Grattan and B. T. Meggitt, Eds., Boston, MA: Springer US, 2000, pp. 1–44, ISBN: 978-1-4757-6081-1. DOI: 10.1007/978-1-4757-6081-1_1.

[6] Y.-J. Rao, "Fiber bragg grating sensors: Principles and applications," in *Optical Fiber Sensor Technology: Devices and Technology*, ser. Optoelectronics, Imaging and Sensing, K. T. V. Grattan and B. T. Meggitt, Eds., Boston, MA: Springer US, 1998, pp. 355–379, ISBN: 978-1-4615-5787-6. DOI: 10.1007/978-1-4615-5787-6_11.

[7] Y. N. Ning and B. T. Meggitt, "Fiber bragg grating sensors: Signal processing aspects," in *Optical Fiber Sensor Technology: Devices and Technology*, ser. Optoelectronics, Imaging and Sensing, K. T. V. Grattan and B. T. Meggitt, Eds., Boston, MA: Springer US, 1998, pp. 381–417, ISBN: 978-1-4615-5787-6. DOI: 10.1007/978-1-4615-5787-6_12.

[8] A. Vaughan, "EDF faces £1m a day bill to keep french nuclear reactor offline," *The Guardian*, Feb. 21, 2017. [Online]. Available: https://www.theguardian.com/business/2017/feb/21/edf-faces-1m-a-day-bill-to-keep-french-nuclear-reactor-offline.

[9] "Mass energy rates - compare electricity rates, switch suppliers and save." (), [Online]. Available: https://www.massenergyrates.com/compare-mass-electricity-rates.

[10] I. The Fiber Optic Association. "The FOA reference for fiber optics - optical fiber for outside plant networks (webpage)." (2018), [Online]. Available: https://www.thefoa.org/tech/ref/OSP/fiber.html.

[11] A. P. Thompson, H. M. Aktulga, R. Berger, *et al.*, "LAMMPS - a flexible simulation tool for particle-based materials modeling at the atomic, meso, and continuum scales," *Computer Physics Communications*, vol. 271, p. 108 171, Feb. 1, 2022. DOI: 10.1016/j.cpc.2021.108171.

[12] A. Stukowski, "Visualization and analysis of atomistic simulation data with OVITO–the open visualization tool," *Modelling and Simulation in Materials Science and Engineering*, vol. 18, no. 1, p. 015 012, Dec. 2009. DOI: 10.1088/0965-0393/18/1/015012.

[13] S. Girard, J. Kuhnhenn, A. Gusarov, B. Brichard, M. Van Uffelen, Y. Ouerdane, A. Boukenter, and C. Marcandella, "Radiation effects on silica-based optical fibers: Recent advances and future challenges," *IEEE Transactions on Nuclear Science*, vol. 60, no. 3, pp. 2015–2036, Jun. 2013, Conference Name: IEEE Transactions on Nuclear Science. DOI: 10.1109/TNS.2012.2235464.

[14] H. Govindarajan, "Atomic-scale modeling of the effects of irradiation on silica optical fibers," Master's thesis (unpublished), Ohio State University, 2011, 127 pp. [Online]. Available: http://rave.ohiolink.edu/etdc/view?acc_num=osu1322670048.

[15] S. Girard, A. Alessi, N. Richard, *et al.*, "Overview of radiation induced point defects in silica-based optical fibers," *Reviews in Physics*, vol. 4, p. 100 032, Nov. 1, 2019. DOI: 10.1016/j.revip.2019.100032.

[16] S. Girard, J. Baggio, and J.-L. Leray, "Radiation-induced effects in a new class of optical waveguides: The air-guiding photonic crystal fibers," *IEEE Transactions on Nuclear Science*, vol. 52, no. 6, pp. 2683–2688, Dec. 2005. DOI: 10.1109/TNS.2005.860735.

[17] V. A. Handerek, "Fiber gratings: Principles, fabrication and properties," in *Optical Fiber Sensor Technology: Devices and Technology*, ser. Optoelectronics, Imaging and Sensing, K. T. V. Grattan and B. T. Meggitt, Eds., Boston, MA: Springer US, 1998, pp. 329–353, ISBN: 978-1-4615-5787-6. DOI: 10.1007/978-1-4615-5787-6_10.

[18] M. Becker, L. Fernandes, M. Rothhardt, S. Bruckner, K. Schuster, J. Kobelke, O. Frazao, H. Bartelt, and P. V. S. Marques, "Inscription of fiber bragg grating arrays in pure silica suspended core fibers," *IEEE Photonics Technology Letters*, vol. 21, no. 19, pp. 1453–1455, Oct. 2009, Conference Name: IEEE Photonics Technology Letters. DOI: 10.1109/LPT.2009.2028309.

[19] Y. Wang, H. Bartelt, M. Becker, S. Brueckner, J. Bergmann, J. Kobelke, and M. Rothhardt, "Fiber bragg grating inscription in pure-silica and ge-doped photonic crystal fibers," *Applied Optics*, vol. 48, no. 11, pp. 1963–1968, Apr. 10, 2009, Publisher: Optica Publishing Group. DOI: 10.1364/AO.48.001963.

[20] F. Falcetelli, A. Martini, R. Di Sante, and M. Troncossi, "Strain modal testing with fiber bragg gratings for automotive applications," *Sensors*, vol. 22, no. 3, p. 946, Jan. 2022, Number: 3 Publisher: Multidisciplinary Digital Publishing Institute. DOI: 10.3390/s22030946.

[21] J. A. Buck, *Fundamentals of Optical Fibers*. John Wiley & Sons, Apr. 27, 2004, 360 pp., ISBN: 978-0-471-22191-3.

[22] D. L. Griscom, "Optical properties and structure of defects in silica glass," *Journal of the Ceramic Society of Japan*, vol. 99, no. 1154, pp. 923–942, 1991. DOI: 10.2109/jcersj.99.923.

[23] N. Kerboub, D. Di Francesca, A. Morana, *et al.*, "Radiation induced attenuation and luminescence study in radioluminescent optical fibers," *IEEE Transactions on Nuclear Science*, vol. 70, no. 8, pp. 1917–1924, Aug. 2023, Conference Name: IEEE Transactions on Nuclear Science. DOI: 10.1109/TNS.2023.3246239.

[24] A. K. Mukhsin, B. I. Maksudbek, G. M. Eldar, I. D. Jalil, N. Izzatillo, R. R. Igor, A. Mukhtor, and S. Kakhramon, "Measurement method of radiation induced emission spectra of optical fibers," *Japanese Journal of Applied Physics*, vol. 47, no. 1, p. 301, Jan. 18, 2008, Publisher: IOP Publishing. DOI: 10.1143/JJAP.47.301.

[25] F. Esposito, R. Ranjan, A. Stăncălie, D. Sporea, D. Neguţ, N. Becherescu, S. Campopiano, and A. Iadicicco, "Real-time analysis of arc-induced long period gratings under gamma irradiation," *Scientific Reports*, vol. 7, no. 1, p. 43 389, Mar. 6, 2017, Publisher: Nature Publishing Group. DOI: 10.1038/srep43389.

[26] B. Brichard, O. V. Butov, K. M. Golant, and A. Fernandez Fernandez, "Gamma radiation-induced refractive index change in ge- and n-doped silica," *Journal of Applied Physics*, vol. 103, no. 5, p. 054 905, Mar. 7, 2008. DOI: 10.1063/1.2885116.

[27] A. Morana, "Gamma-rays and neutrons effects on optical fibers and bragg gratings for temperature sensors," Ph.D. dissertation, Universite Jean Monnet de Saint-Etienne; Universita Degli Studi di Palermo, 2013. [Online]. Available: https://tel.archives-ouvertes.fr/tel-01064993.

[28] J. Zhang, Y. Xiang, C. Wang, Y. Chen, S. C. Tjin, and L. Wei, "Recent advances in optical fiber enabled radiation sensors," *Sensors (Basel, Switzerland)*, vol. 22, no. 3, p. 1126, Feb. 1, 2022. DOI: 10.3390/s22031126.

[29] G. M. Lo Piccolo, M. Cannas, and S. Agnello, "Intrinsic point defects in silica for fiber optics applications," *Materials*, vol. 14, no. 24, p. 7682, Dec. 13, 2021. DOI: 10.3390/ma14247682.

[30] A. Morana, C. Campanella, J. Vidalot, V. De Michele, E. Marin, I. Reghioua, A. Boukenter, Y. Ouerdane, P. Paillet, and S. Girard, "Extreme radiation sensitivity of ultra-low loss pure-silica-core optical fibers at low dose levels and infrared wavelengths," *Sensors*, vol. 20, no. 24, p. 7254, Jan. 2020, Number: 24 Publisher: Multidisciplinary Digital Publishing Institute. DOI: 10.3390/s20247254.

[31] P. F. Kashaykin, E. A. Pospelova, Y. O. Sharonova, O. L. Vokhmyanina, I. S. Azanova, and A. L. Tomashuk, "Temperature and polarization dependence of radiation-induced attenuation in pure-silica-core PANDA optical fiber," *Optical Materials*, vol. 131, p. 112 510, Sep. 1, 2022. DOI: 10.1016/j.optmat.2022.112510.

[32] T.-E. Tsai and D. L. Griscom, "On the structures of hydrogen-associated defect centers in irradiated high-purity a-SiO2:OH," *Journal of Non-Crystalline Solids*, vol. 91, no. 2, pp. 170–179, May 1, 1987. DOI: 10.1016/S0022-3093(87)80300-9.

[33] L. N. Skuja, A. N. Streletsky, and A. B. Pakovich, "A new intrinsic defect in amorphous SiO2: Twofold coordinated silicon," *Solid State Communications*, vol. 50, no. 12, pp. 1069–1072, Jun. 1, 1984. DOI: 10.1016/0038-1098(84)90290-4.

[34] D. Griscom, "Self-trapped holes in pure-silica glass: A history of their discovery and characterization and an example of their critical significance to industry," *Journal of Non-Crystalline Solids*, vol. 352, pp. 2601–2617, Jul. 1, 2006. DOI: 10.1016/j.jnoncrysol.2006.03.033.

[35] E. M. Dianov, V. N. Karpechev, V. O. Sokolov, V. B. Sulimov, P. V. Chernov, L. S. Kornienko, I. O. Morozova, and A. O. Rybaltovskii, "Spectroscopic manifestations of self-trapped holes in silica theory and experiment," *physica status solidi (b)*, vol. 156, no. 2, pp. 663–675, 1989. DOI: 10.1002/pssb.2221560230.

[36] C. Sousa, C. de Graaf, and G. Pacchioni, "Optical properties of peroxy radicals in silica: Multiconfigurational perturbation theory calculations," *The Journal of Chemical Physics*, vol. 114, no. 14, pp. 6259–6264, Apr. 8, 2001. DOI: 10.1063/1.1355986.

[37] B. Winkler, L. Martin-Samos, N. Richard, L. Giacomazzi, A. Alessi, S. Girard, A. Boukenter, Y. Ouerdane, and M. Valant, "Correlations between structural and optical properties of peroxy bridges from first principles," *The Journal of Physical Chemistry C*, vol. 121, no. 7, pp. 4002–4010, Feb. 23, 2017, Publisher: American Chemical Society. DOI: 10.1021/acs.jpcc.6b11291.

[38] H. Nishikawa, R. Tohmon, Y. Ohki, K. Nagasawa, and Y. Hama, "Defects and optical absorption bands induced by surplus oxygen in high-purity synthetic silica," *Journal of Applied Physics*, vol. 65, no. 12, pp. 4672–4678, Jun. 15, 1989. DOI: 10.1063/1.343242.

[39] A.-M. El-Sayed, M. B. Watkins, V. V. Afanas'ev, and A. L. Shluger, "Nature of intrinsic and extrinsic electron trapping in SiO${}_{2}$," *Physical Review B*, vol. 89, no. 12, p. 125 201, Mar. 10, 2014, Publisher: American Physical Society. DOI: 10.1103/PhysRevB.89.125201.

[40] S. Girard, Y. Ouerdane, G. Origlio, *et al.*, "Radiation effects on silica-based preforms and optical fibers—i: Experimental study with canonical samples," *IEEE Transactions on Nuclear Science*, vol. 55, no. 6, pp. 3473–3482, Dec. 2008, Conference Name: IEEE Transactions on Nuclear Science. DOI: 10.1109/TNS.2008.2007297.

[41] S. Girard, N. Richard, Y. Ouerdane, G. Origlio, A. Boukenter, L. Martin-Samos, P. Paillet, and R. Boscaino, "Radiation effects on silica-based preforms and optical fibers-II: Coupling ab initio simulations and experiments," *IEEE Transactions on Nuclear Science*, vol. 55, no. 6, pp. 3508–3514, 2008. DOI: 10.1109/TNS.2008.2007232.

[42] H. Nishikawa, R. Nakamura, Y. Ohki, and Y. Hama, "Correlation of preexisting diamagnetic defect centers with induced paramagnetic defect centers by ultraviolet or vacuum-ultraviolet photons in high-purity silica glasses," *Physical Review B*, vol. 48, no. 21, pp. 15 584–15 594, Dec. 1, 1993. DOI: 10.1103/PhysRevB.48.15584.

[43] G. Pacchioni, L. Skuja, D. L. Griscom, and NATO Advanced Study Institute on Defects in SiO2 and Related Dielectrics Science and Technology, *Defects in SiO2 and Related Dielectrics: Science and Technology* (NATO Science Series II: Mathematics, Physics and Chemistry, Mathematics, Physics and Chemistry, 2), 1st ed. 2000. Dordrecht: Springer Netherlands, 2000, viii+624, ISBN: 978-94-010-0944-7. DOI: 10.1007/978-94-010-0944-7.

[44] S. Agnello and L. Nuccio, "Thermal stability of gamma-irradiation-induced oxygen-deficient centers in silica," *Physical Review B*, vol. 73, no. 11, p. 115 203, Mar. 14, 2006, Publisher: American Physical Society. DOI: 10.1103/PhysRevB.73.115203.

[45] P. Martín, M. León, A. Ibarra, and E. R. Hodgson, "Thermal stability of gamma irradiation induced defects for different fused silica," *Journal of Nuclear Materials*, Proceedings of ICFRM-14, vol. 417, no. 1, pp. 818–821, Oct. 1, 2011. DOI: 10.1016/j.jnucmat.2010.12.171.

[46] C. F. Systems, *SPARC RPT r&d MPS 0001 (unpublished)*.

[47] S. Girard, C. Marcandella, A. Morana, *et al.*, "Combined high dose and temperature radiation effects on multimode silica-based optical fibers," *IEEE Transactions on Nuclear Science*, vol. 60, no. 6, pp. 4305–4313, Dec. 2013. DOI: 10.1109/TNS.2013.2281832.

[48] C. E. Barnes, "Irradiation and photobleaching of all-silica, pure silica core fibers at low temperatures," in *Optical Fibers in Adverse Environments*, vol. 0404, SPIE, Mar. 29, 1984, pp. 47–54. DOI: 10.1117/12.935627.

[49] H. Henschel, O. Kohn, and H. Schmidt, "Radiation hardening of optical fibre links by photobleaching with light of shorter wavelength," *IEEE Transactions on Nuclear Science*, vol. 43, no. 3, pp. 1050–1056, Jun. 1996, Conference Name: IEEE Transactions on Nuclear Science. DOI: 10.1109/23.510754.

[50] C. Campanella, A. Guttilla, A. Morana, *et al.*, "Photobleaching effect on infrared radiation-induced attenuation of germanosilicate optical fibers at MGy dose levels," *IEEE Transactions on Nuclear Science*, vol. 68, no. 8, pp. 1688–1693, Aug. 2021, Conference Name: IEEE Transactions on Nuclear Science. DOI: 10.1109/TNS.2021.3068829.

[51] F. S. Fernandez, B. M. Ludbrook, J. Schuyt, B. Trompetter, D. A. Moseley, S. M. Haneef, and R. A. Badcock, "Mitigation of radiation-induced attenuation of optical fibers through photobleaching: Study of power dependence at cryogenic temperatures," in *Sensors and Smart Structures Technologies for Civil, Mechanical, and Aerospace Systems 2024*, vol. 12949, SPIE, May 9, 2024, pp. 56–65. DOI: 10.1117/12.3010652.

[52] D. Di Francesca, A. Boukenter, S. Agnello, A. Alessi, S. Girard, M. Cannas, and Y. Ouerdane, "Resonance raman of oxygen dangling bonds in amorphous silicon dioxide," *Journal of Raman Spectroscopy*, vol. 48, no. 2, pp. 230–234, 2017. DOI: 10.1002/jrs.5006.

[53] N. Shimodaira, K. Saito, and A. J. Ikushima, "Raman spectra of fluorine-doped silica glasses with various fictive temperatures," *Journal of Applied Physics*, vol. 91, no. 6, pp. 3522–3525, Mar. 15, 2002, Publisher: American Institute of Physics. DOI: 10.1063/1.1452779.

[54] G. E. Walrafen and J. Stone, "Raman spectral characterization of pure and doped fused silica optical fibers," *Applied Spectroscopy*, vol. 29, no. 4, pp. 337–344, Jul. 1, 1975, Publisher: Society for Applied Spectroscopy. DOI: 10.1366/000370275774455969.

[55] G. Schreckenbach and T. Ziegler, "Calculation of the g-tensor of electron paramagnetic resonance spectroscopy using gauge-including atomic orbitals and density functional theory," *The Journal of Physical Chemistry A*, vol. 101, no. 18, pp. 3388–3399, May 1, 1997. DOI: 10.1021/jp963060t.

[56] S. Le Roux and P. Jund, "Ring statistics analysis of topological networks: New approach and application to amorphous GeS2 and SiO2 systems," *Computational Materials Science*, vol. 49, no. 1, pp. 70–83, Jun. 1, 2010. DOI: 10.1016/j.commatsci.2010.04.023.

[57] H. Wehr and D. Wiechert, "Refractive index and density of fluorine doped silica prepared by the PCVD process," *Materials Research Bulletin*, vol. 21, no. 5, pp. 559–566, May 1, 1986. DOI: 10.1016/0025-5408(86)90110-8.

[58] M. Ogai, A. Uno, and K. Matsubara, "Characteristics of fluorine-doped silica fiber," in *Optical Fiber Communication (1988), paper TuB4*, Optica Publishing Group, Jan. 25, 1988, TuB4. DOI: 10.1364/OFC.1988.TuB4.

[59] S. S. Courts, "High level gamma radiation effects on cernox™ cryogenic temperature sensors," *IOP Conference Series: Materials Science and Engineering*, vol. 278, p. 012 076, Dec. 2017. DOI: 10.1088/1757-899X/278/1/012076.

[60] A. E. of Canada Limited, *Instruction manual gammacell 220 cobalt 60 irradiation unit*. Jul. 1968. [Online]. Available: https://www.nrc.gov/docs/ML0216/ML021630449.pdf.

[61] M. Berger, J. Hubbell, S. Seltzer, J. Coursey, and D. Zucker, *XCOM: Photon cross section database (version 1.2)*, Jan. 1, 1999.

[62] M. P. Short and J. H. Chang. "Co-60 decay information (KAERI)." (), [Online]. Available: https://pripyat.mit.edu/KAERI/cgi-bin/decay?Co-60%20B-.

[63] N. Bende, *Nakulbende/TTL_ trigger*, original-date: 2015-09-21T21:09:19Z, Oct. 9, 2023. [Online]. Available: https://github.com/nakulbende/TTL_Trigger.

[64] J. J. Schuyt, O. Duke, D. A. Moseley, B. M. Ludbrook, E. E. Salazar, and R. A. Badcock, "Gamma irradiation of ge-doped and radiation-hard silica fibers at cryogenic temperatures: Mitigating the radiation-induced attenuation with 1550 and 970 nm photobleaching," *Journal of Applied Physics*, vol. 134, no. 4, p. 043 103, Jul. 24, 2023. DOI: 10.1063/5.0155057.

[65] M. Schmid, D. Rath, and U. Diebold, "Why and how savitzky–golay filters should be replaced," *ACS Measurement Science Au*, vol. 2, no. 2, pp. 185–196, Apr. 20, 2022, Publisher: American Chemical Society. DOI: 10.1021/acsmeasuresciau.1c00054.

[66] "SuperK COMPACT," NKT Photonics. (), [Online]. Available: https://www.nktphotonics.com/products/supercontinuum-white-light-lasers/superk-compact/.

[67] F. Hofmann, M. P. Short, and C. A. Dennett, "Transient grating spectroscopy: An ultrarapid, nondestructive materials evaluation technique," *MRS Bulletin*, vol. 44, no. 5, pp. 392–402, May 2019, Publisher: Cambridge University Press. DOI: 10.1557/mrs.2019.104.

[68] A. Schweiger and G. Jeschke, *Principles of Pulse Electron Paramagnetic Resonance*. Oxford, New York: Oxford University Press, Aug. 9, 2001, 604 pp., ISBN: 978-0-19-850634-8.

[69] E. (C. Duin. "Duin laboratory webpage - auburn university." (), [Online]. Available: https://webhome.auburn.edu/~duinedu/.

[70] L. Giacomazzi, L. Martin-Samos, A. Boukenter, Y. Ouerdane, S. Girard, and N. Richard, "EPR parameters of ${e}^{\ensuremath{'}}$ centers in $v\ensuremath{-}{\mathrm{SiO}}_{2}$ from first-principles calculations," *Physical Review B*, vol. 90, no. 1, p. 014 108, Jul. 28, 2014, Publisher: American Physical Society. DOI: 10.1103/PhysRevB.90.014108.

[71] M. Lancry, N. Ollier, B. H. Babu, C. Herrero, and B. Poumellec, "EPR reversible signature of self-trapped holes in fictive temperature-treated silica glass," *Journal of Applied Physics*, vol. 123, no. 11, p. 113 101, Mar. 15, 2018. DOI: 10.1063/1.5023310.

[72] M. Matthewson, C. Kurkjian, and J. Hamblin, "Acid stripping of fused silica optical fibers without strength degradation," *Journal of Lightwave Technology*, vol. 15, no. 3, pp. 490–497, Mar. 1997. DOI: 10.1109/50.557565.

[73] A. P. C. Wylie, K. B. Woller, S. A. A. Al Dajani, B. R. Dacus, E. J. Pickering, M. Preuss, and M. P. Short, "Thermal diffusivity in ion-irradiated single-crystal iron, chromium, vanadium, and tungsten measured using transient grating spectroscopy," *Journal of Applied Physics*, vol. 132, no. 4, p. 045 102, Jul. 22, 2022. DOI: 10.1063/5.0089048.

[74] E. Trachanas, A. Bignami, N. Gazis, A. P. C. Wylie, K. B. Woller, B. R. Dacus, M. P. Short, E. Gazis, and G. Fikioris, "Thermal diffusivity variation assessment on radio-frequency quadrupole cu-OF copper due to proton irradiation," *Nuclear Instruments and Methods in Physics Research Section B: Beam Interactions with Materials and Atoms*, vol. 539, pp. 179–189, Jun. 1, 2023. DOI: 10.1016/j.nimb.2023.04.002.

[75] C. A. Dennett and M. P. Short, "Thermal diffusivity determination using heterodyne phase insensitive transient grating spectroscopy," *Journal of Applied Physics*, vol. 123, no. 21, p. 215 109, Jun. 6, 2018. DOI: 10.1063/1.5026429.

[76] L. S. Cryotronics. "Cryostat windows," Default. (2024).

[77] D. V. Orlinski, I. V. Al'tovsky, T. A. Bazilevskaya, *et al.*, "Preliminary results of window radiation resistance investigations," *Journal of Nuclear Materials*, Fusion Reactor Materials, vol. 212-215, pp. 1059–1064, Sep. 1, 1994. DOI: 10.1016/0022-3115(94)90995-4.

[78] Buehler. "Methods by material - buehler - metallography equipment & supplies for sample preparation." (Oct. 21, 2021), [Online]. Available: https://www.buehler.com/solutions/buehler-solutions/methods-by-material/.

[79] J. Zhou, H. D. Shin, K. Chen, B. Song, R. A. Duncan, Q. Xu, A. A. Maznev, K. A. Nelson, and G. Chen, "Direct observation of large electron–phonon interaction effect on phonon heat transport," *Nature Communications*, vol. 11, no. 1, p. 6040, Nov. 27, 2020, Publisher: Nature Publishing Group. DOI: 10.1038/s41467-020-19938-9.

[80] *COMSOL multiphysics*, version 6.2. Stockholm, Sweden. [Online]. Available: www.comsol.com.

[81] P. K. Romano, N. E. Horelik, B. R. Herman, A. G. Nelson, B. Forget, and K. Smith, "OpenMC: A state-of-the-art monte carlo code for research and development," *Annals of Nuclear Energy*, Joint International Conference on Supercomputing in Nuclear Applications and Monte Carlo 2013, SNA + MC 2013. Pluri- and Trans-disciplinarity, Towards New Modeling and Numerical Simulation Paradigms, vol. 82, pp. 90–97, Aug. 1, 2015. DOI: 10.1016/j.anucene.2014.07.048.